

Restriction/Classification Cancelled

Copy /
RM SL54A12

JAN 21 1954 RPT

Restriction/Classification Cancelled

PERMANENT FILE COPY

NACA

Source of Acquisition
CASI Acquired

RESEARCH MEMORANDUM

for the

Bureau of Aeronautics, Department of the Navy

PRELIMINARY INVESTIGATION OF THE STATIC LONGITUDINAL AND
 LATERAL STABILITY CHARACTERISTICS OF A 0.05-SCALE
 MODEL OF THE CONVAIR F2Y-1 AIRPLANE
 AT HIGH SUBSONIC SPEEDS

TED NO. NACA DE 383

By Kenneth P. Spreemann and Albert G. Few, Jr.

Langley Aeronautical Laboratory
 Langley Field, Va.

CLASSIFIED DOCUMENT

Restriction/Classification Cancelled

of the United States within the meaning
 of the espionage laws, Title 18, U.S.C., Secs. 793 and 794, the transmission or revelation of which in any
 manner to an unauthorized person is prohibited by law.

NATIONAL ADVISORY COMMITTEE
 FOR AERONAUTICS

WASHINGTON

JAN 18 1954

FILE COPY

To be returned to
 the files of the National
 Advisory Committee

for Aeronautics
 Washington, D.C.

16

CONFIDENTIAL
 Restriction/Classification Cancelled

NATIONAL ADVISORY COMMITTEE FOR AERONAUTICS

RESEARCH MEMORANDUM

for the

Bureau of Aeronautics, Department of the Navy

PRELIMINARY INVESTIGATION OF THE STATIC LONGITUDINAL AND

LATERAL STABILITY CHARACTERISTICS OF A 0.05-SCALE

MODEL OF THE CONVAIR F2Y-1 AIRPLANE

AT HIGH SUBSONIC SPEEDS

TED NO. NACA DE 383

By Kenneth P. Spreemann and Albert G. Few, Jr.

SUMMARY

A preliminary investigation of the static longitudinal and lateral stability characteristics of a 0.05-scale model of the Convair F2Y-1 water-based fighter airplane was made in the Langley high-speed 7- by 10-foot tunnel. The investigation was made with and without wing fences over a Mach number range of 0.50 to 0.94. The maximum angle-of-attack range (obtained at the lower Mach numbers) was from about -2° to 25° . Sideslip angles ranging from -4° to 12° also were investigated.

For the basic model without fences, regions of longitudinal instability were found to exist at a lift coefficient of about 0.40 throughout the Mach number range investigated. In general, most of the fences employed delayed the instability of the model to considerably higher lift coefficients and angles of attack. The fences had little or no significant effects on the lift and drag characteristics except for a small increase in drag at zero angle of attack. The elevator effectiveness at zero lift for small settings and for the lower Mach numbers held up well through the lift-coefficient range; however, at Mach numbers of 0.92 and 0.94, rather large losses in effectiveness were indicated at the higher angles of attack.

The model was directionally stable up to 21° or 23° angle of attack but became highly unstable at higher angles. Up to a Mach number of 0.85, aileron effectiveness was rather constant up to 20° or 22° angle of attack; but above this Mach number, some reduction in effectiveness was evident

above about 12° or 14° angle of attack. The rudder effectiveness was almost constant throughout the Mach number and angle-of-attack range investigated.

INTRODUCTION

At the request of the Bureau of Aeronautics, Department of the Navy, National Advisory Committee for Aeronautics has conducted a preliminary investigation at high subsonic speeds of the static longitudinal and lateral stability characteristics of a 0.05-scale model of the Convair F2Y-1 water-based fighter airplane. The tests covered a Mach number range from 0.5 to 0.94 and corresponding Reynolds numbers, based on the wing mean aerodynamic chord, from 3.3×10^6 to 4.3×10^6 . The maximum angle-of-attack range (obtained at the lower Mach numbers) was from -2° to 25° . Sideslip angles from -4° to 12° also were investigated. The investigation included effects of various arrangements of wing fences and of rocket packages.

COEFFICIENTS AND SYMBOLS

The stability system of axes used for the presentation of the data, together with an indication of the positive directions of forces, moments, and angles, are presented in figure 1. All moments are referred to the 30-percent-chord point of the mean aerodynamic chord.

C_L	lift coefficient, $\frac{\text{Lift}}{qS_w}$
C_D	drag coefficient, $\frac{\text{Drag}}{qS_w}$
C_m	pitching-moment coefficient, $\frac{\text{Pitching moment}}{qS_w \bar{c}}$
C_l	rolling-moment coefficient, $\frac{\text{Rolling moment}}{qS_w b}$
C_n	yawing-moment coefficient, $\frac{\text{Yawing moment}}{qS_w b}$
C_Y	lateral-force coefficient, $\frac{\text{Lateral force}}{qS_w}$

q dynamic pressure, $\frac{\rho V^2}{2}$, lb/sq ft
 S area, sq ft
 \bar{c} mean aerodynamic chord of wing, $\frac{2}{S_w} \int_0^{b/2} c^2 dy$, 1.069 ft on model
 c local wing chord, parallel to plane of symmetry, ft
 b wing span, 1.76 ft on model
 ρ air density, slugs per cubic ft
 V free-stream velocity, ft/sec
 P static pressure, lb/sq ft
 M Mach number
 R Reynolds number of wing based on \bar{c}
 α angle of attack of fuselage reference line, deg
 β angle of sideslip, deg
 Λ leading-edge sweep angle, deg
 δ control surface deflection, deg

$$C_{l\beta} = \frac{\partial C_l}{\partial \beta} \text{ per deg}$$

$$C_{n\beta} = \frac{\partial C_n}{\partial \beta} \text{ per deg}$$

$$C_{Y\beta} = \frac{\partial C_Y}{\partial \beta} \text{ per deg}$$

L/D lift-drag ratio

Subscripts:

o free stream

w wing

b base of model fuselage
E duct exit
e elevon
r rudder
max maximum

MODEL DESIGNATIONS

B fuselage
C canopy
V vertical fin
W wing; W also used with following subscripts:
 F₁ fence 1
 F₂ fence 2
 F₃ fence 3
 RP rocket package

Combinations of the above designations that indicate the various configurations investigated are listed in table I.

MODEL AND APPARATUS

A drawing of the 0.05-scale model of the Convair F2Y-1 airplane employed in this investigation is presented in figure 2. Note that a small modification was made to the afterbody to accommodate the sting (shown in fig. 2). Details of the fences and fence positions tested are shown in figure 3. Included in figure 3 is a sketch of the rocket package tested on this model. Photographs of the various model configurations tested are presented in figure 4. A photograph of the basic model mounted on the sting in the Langley high-speed 7- by 10-foot tunnel is shown in figure 4(d). Presented in table II is a sketch of the probe positions employed in the duct exit.

The model was tested on the sting-type support system shown in figure 4(d). With this system, the model was remotely operated through

an angle-of-attack range of about -2° to 25° . A strain-gage balance mounted inside the fuselage was used to measure the forces and moments of the model.

TESTS AND CORRECTIONS

The investigation was made in the Langley high-speed 7- by 10-foot tunnel over a Mach number range of 0.50 to 0.94 at angles of attack ranging from about -2° to 25° and through a sideslip range from -4° to 12° . The model caused the tunnel to choke above a corrected Mach number of about 0.97 at zero angle of attack, although partial choking conditions may have occurred in the high angle-of-attack range at a Mach number of 0.94.

Blockage corrections were determined by the method of reference 1 and were applied to the Mach numbers and dynamic pressures. Jet-boundary corrections, applied to the angle of attack and drag, were calculated by the method of reference 2. The angles of attack and sideslip have been corrected for deflection of the sting support system under load. The jet-boundary corrections to pitching moment were considered negligible and were not applied to the data. Corrections to the drag coefficients for buoyancy due to longitudinal pressure gradients were about 0.0007 to 0.0008 throughout the Mach number range investigated. These corrections were not applied to the data. No tare corrections were obtained.

The drag data have been corrected by adjusting the base pressure drag to a pressure at the base of the fuselage equal to free-stream static pressure. For this correction, the base pressure was determined by measuring the pressure inside the fuselage at a point about 9 inches forward of the base. The drag correction (base pressure drag coefficient C_{D_b}) was calculated from the measured pressure data by the relation

$$C_{D_b} = \frac{P_b - P_\infty}{q} \frac{S_b}{S_w}$$

Values of C_{D_b} for average test conditions are presented in figure 5. The corrected model drag data were obtained by adding the base pressure drag coefficient to the drag coefficient determined from the strain-gage measurements.

The mean Reynolds number variation with Mach number for the model of this investigation is presented in figure 6.

RESULTS AND DISCUSSION

The data are presented in figures 7 to 26; a detailed listing of the data is given in table I. Presented in table II are the duct exit survey stations and velocity ratios for the BCWF₁V configuration with $\delta_e = 0^\circ$, $\delta_r = 0^\circ$, and the duct full open. All configurations presented in the present paper were tested with ducts full open. Data for an elevon deflection of -20° (presented in fig. 10) were obtained for a Mach number of 0.50 only because of limited tunnel time and the feeling that higher Mach numbers for this elevon deflection would be of little interest. The data indicated by dashed lines in figures 9 to 14 have been reproduced from figure 8 to facilitate analysis of these data. The slopes presented in figure 26 have been averaged over a lift-coefficient range of about 0 to 0.4. In order to expedite the publication of these data, only a brief analysis of the data is included herein.

Longitudinal Stability Characteristics

Lift.- All configurations exhibited much the same maximum lift characteristics. (See parts (a) of figs. 8, 9, and 11 to 16 and fig. 10.)

The lift-curve slopes $\frac{\partial C_L}{\partial \alpha}$ were practically unaffected by the addition of any of the fences (fig. 26). The trimmed lift-curve slope was about 10 to 15 percent lower than the untrimmed slope throughout the Mach number range investigated.

Drag.- The addition of any of the fences to the basic model (BCWV, $\delta_e = 0^\circ$, $\delta_r = 0^\circ$) increased the drag coefficient at zero angle of attack $C_{D\alpha=0}$ about 0.001 to 0.002 throughout the Mach number range investigated. (See fig. 7.) An elevon deflection of -10° resulted in an increase of 0.006 to 0.01 in $C_{D\alpha=0}$; whereas, -5° deflection caused an increase of only about 0.001 throughout the Mach number range investigated.

The drag due to lift $\frac{\partial C_D}{\partial C_L^2}$ was not greatly affected by the addition of fence 1 (see fig. 26). In the trimmed condition, $\frac{\partial C_D}{\partial C_L^2}$ was increased about 20 to 30 percent up to $M = 0.90$. Above this Mach number, the trimmed model gave a sharp rise in drag due to lift.

Lift-drag ratios. - The addition of fence 1 to the basic model reduced the maximum lift-drag ratios by about 2 to 5 percent throughout the Mach number range investigated; however, at lift coefficients above that for $(L/D)_{max}$, the effect of the fence was insignificant. Trimming the model at the assumed center-of-gravity location ($0.30\bar{c}$) generally reduced the lift-drag ratios by from 15 to 20 percent over the Mach number range investigated. (See figs. 25 and 26.)

Pitching moment. - For the basic model without fences, regions of longitudinal instability were found to exist at a lift coefficient of about 0.40 throughout the Mach number range investigated. All of the fences employed, with the possible exception of fence 3, delayed the instability of the model to considerably higher lift coefficients and angles of attack (usually $C_L \approx 0.2$ to 0.4 or 6° to 8° angle of attack). (See parts (d) and (e) of figs. 8 and 11 to 14.) However, the departures from linearity in the medium lift and angle-of-attack range still may be undesirable on the basis of dynamic-stability considerations. Fence 3 was the least effective in reducing the instability of the model, since pitch-up was indicated between lift coefficients of 0.3 to 0.4.

The fences employed on this model had little effect on the aerodynamic-center location as is illustrated in figure 26, wherein the addition of fence 1 (which is a typical example) gave practically no

change in $\frac{\partial C_m}{\partial C_L}$ throughout the Mach number range investigated.

Elevator effectiveness. - The results obtained for various elevator settings (figs. 8 and 9) indicate that the elevator effectiveness $\left(\frac{\partial C_m}{\partial \delta_e}\right)_{C_L=0}$ (fig. 24) for small settings and for the lower Mach numbers held up well through the lift-coefficient range. At Mach number of 0.92 and 0.94, however, quite a large loss in effectiveness was indicated at high angles of attack. Although no serious loss was indicated at trim conditions for the assumed center-of-gravity location, it is possible that some impairment in maneuverability may result at the highest Mach numbers. At zero

lift, the effectiveness parameter $\frac{\partial C_m}{\partial \delta_e}$ for small deflections increased

in magnitude from -0.0051 to -0.0064 as the Mach number increased from 0.50 to 0.90 but then decreased to -0.0057 at $M = 0.94$. (See fig. 24.) In assessing the elevator effectiveness, it should be noted that some flexibility in the elevator restraining members did exist; however, comparisons of the present data with additional data (not presented in this paper) obtained with the elevator locked indicate that the effects of flexibility were extremely small.

Lateral Stability Characteristics

Lateral stability.- Within the ranges of test variables for which comparable data were obtained, there were only small changes in the lateral stability characteristics of the model with the addition of fence 1. With fence 1 installed, the model showed no instabilities in sideslip at 0° and 12° angle of attack; but at 24° angle of attack in the low Mach number range, large directional instabilities were encountered. (See fig. 18.) It should be noted that 24° angle of attack is at or above the maximum lift and consequently flow instability would be expected. The lateral-stability-parameter data presented in figure 19 show that the model with fence 1 became unstable at 23° and 21° angle of attack or at $C_L = 0.8$ and 0.85 for Mach numbers of 0.50 and 0.85 , respectively. Note that these data were taken from the slopes between two series of tests made at $\pm 4^\circ$ sideslip and, therefore, would not indicate nonlinearities that exist in the high angle-of-attack range between these two sideslip angles.

Comparison of figures 18 and 21 indicates that the tail contribution to the directional stability C_{n_B} of the model at 0° and 12° angle of attack was increased from approximately 0.0023 at $M = 0.50$ to 0.0029 at $M = 0.92$.

Aileron and rudder effectiveness.- The results of deflecting the left aileron to -10° are presented in figure 22 for the model with fence 1 installed. Up to a Mach number of 0.85 , aileron effectiveness was rather constant up to 20° or 22° angle of attack; but above this Mach number, some reduction in effectiveness was evident above about 12° or 14° angle of attack.

The effects of a rudder deflection of 10° are presented in figure 23 and these data indicate almost constant rudder effectiveness throughout the Mach number and angle-of-attack range investigated.

CONCLUSIONS

A preliminary investigation to determine the static longitudinal and lateral stability characteristics, with and without wing fences, of a 0.05-scale model of the Convair F2Y-1 water-based fighter airplane at high subsonic speeds indicates the following conclusions:

- (1) For the basic model without fences, regions of longitudinal instability were found to exist at a lift coefficient of about 0.40 throughout the Mach number range investigated.

(2) Most of the fences employed in this investigation delayed the longitudinal instability of the model to considerably higher lift coefficients and angles of attack.

(3) The fences had little or no significant effects on the lift and drag characteristics except for a small increase in drag at zero angle of attack.

(4) Deflecting the elevators to provide longitudinal trim reduced the maximum lift-drag ratios about 15 to 20 percent and increased the drag due to lift about 20 to 40 percent throughout the Mach number range investigated.

(5) The elevator effectiveness at zero lift for small settings and for the lower Mach numbers held up well through the lift-coefficient range; however, at Mach numbers of 0.92 and 0.94, quite large losses in effectiveness were indicated at the high angles of attack.

(6) The model was directionally stable up to 21° or 23° angle of attack, but became highly unstable at higher angles.

(7) Up to a Mach number of 0.85, the aileron effectiveness was almost constant up to 20° or 22° angle of attack, but above this Mach number some reduction in effectiveness was evident above about 12° or 14° angle of attack.

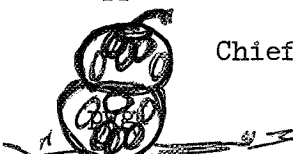
(8) The rudder effectiveness was almost constant throughout the Mach number and angle-of-attack range investigated.

Langley Aeronautical Laboratory,
National Advisory Committee for Aeronautics,
Langley Field, Va., December 30, 1953.

Kenneth P. Spremann
Kenneth P. Spremann
Aeronautical Research Scientist

Albert G. Few Jr.
Albert G. Few, Jr.
Aeronautical Research Scientist

Approved: *Thomas A. Harris*
Thomas A. Harris
Chief of Stability Research Division



REFERENCES

1. Herriot, John G.: Blockage Corrections for Three-Dimensional-Flow Closed-Throat Wind Tunnels, With Consideration of the Effect of Compressibility. NACA Rep. 995, 1950. (Supersedes NACA RM A7B28.)
2. Gillis, Clarence L., Polhamus, Edward C., and Gray, Joseph L., Jr.: Charts for Determining Jet-Boundary Corrections for Complete Models in 7- by 10-Foot Closed Rectangular Wind Tunnels. NACA WR L-123, 1945. (Formerly NACA ARR L5G31.)

TABLE I.- INDEX OF FIGURES PRESENTING DATA

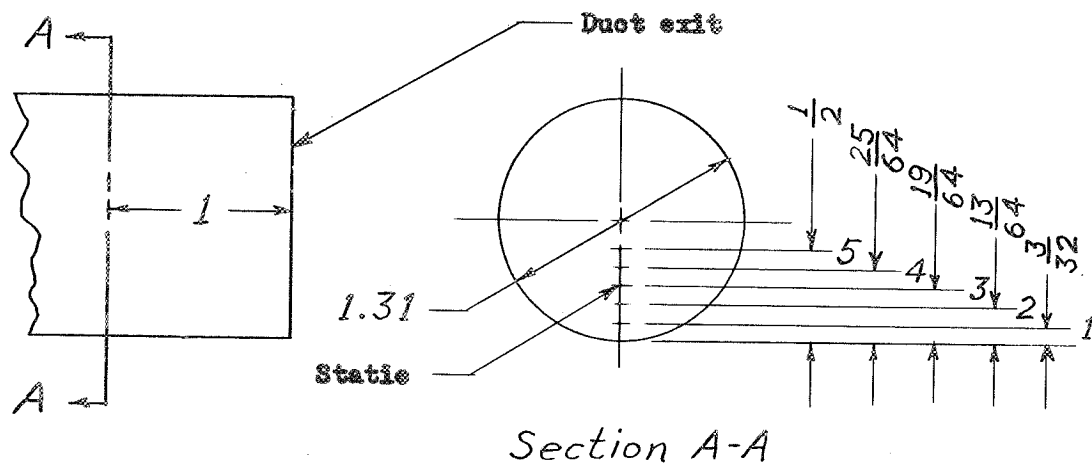
Figure	Configuration	δ_e , deg		δ_r , deg	Data presented
		Right	Left		
7	BC	0	0	--	Drag at $\alpha = 0^\circ$
	BCWF ₁	0	0	--	
	BCWV	0	0	0	
	BCWF ₁ V	0	0	0	
	BCWF ₂ V	0	0	0	
	BCWF ₃ V	0	0	0	
	BCWF ₂₊₃ V	0	0	0	
	BCWF _{1+RP} V	0	0	0	
	BCWF ₁ V	0	0	0	
	BCWF ₁ V	-5	-5	0	
8	BCWV	0	0	0	Basic longitudinal
	BCWF ₁ V	0	0	0	
9	BCWF ₁ V	0	0	0	Basic longitudinal
	BCWF ₁ V	-5	-5	0	
	BCWF ₁ V	-10	-10	0	
10	BCWF ₁ V	0	0	0	Basic longitudinal
	BCWF ₁ V	-20	-20	0	
11	BCWV	0	0	0	Basic longitudinal
	BCWF ₂ V	0	0	0	
12	BCWV	0	0	0	Basic longitudinal
	BCWF ₃ V	0	0	0	
13	BCWV	0	0	0	Basic longitudinal
	BCWF ₂₊₃ V	0	0	0	

TABLE I. - INDEX OF FIGURES PRESENTING DATA - CONCLUDED

Figure	Configuration	δ_e , deg		δ_r , deg	Data presented
		Right	Left		
14	BCWV BCWF ₁ +RPV	0 0	0 0	0 0	Basic longitudinal
15	BCWF ₁ V	0	-10	0	Basic longitudinal
16	BCWF ₁ V	0	0	10	Basic longitudinal
17	BCWV	0	0	0	Basic lateral
18	BCWF ₁ V	0	0	0	Basic lateral
19	BCWF ₁ V	0	0	0	Lateral stability
20	BCWF ₁ +RPV	0	0	0	Basic lateral
21	BCWF ₁	0	0	--	Basic lateral
22	BCWF ₁ V BCWF ₁ V	0 0	-10 0	0 0	Basic lateral
23	BCWF ₁ V BCWF ₁ V	0 0	0 0	10 0	Basic lateral
24	BCWF ₁ V	0	0	0	Elevator effectiveness
25	BCWV BCWF ₁ V	0 0	0 0	0 0	L/D
26	BCWV BCWF ₁ V	0 0	0 0	0 0	Summary

TABLE II

DUCT EXIT SURVEY STATIONS AND VELOCITY RATIOS

(Configuration BCWF₁V; $\delta_e = 0^\circ$, $\delta_r = 0^\circ$)

M	V_o	v_E/v_o			
		Tube number			
		1	2	4	5
0.50	510	0.508	0.628	---	0.668
.70	774	.396	.488	---	.523
.85	926	.354	.432	0.477	.505
.90	972	.349	.436	.496	.524
.92	990	.348	.436	.501	.528
.94	1002	.339	.427	.494	.512

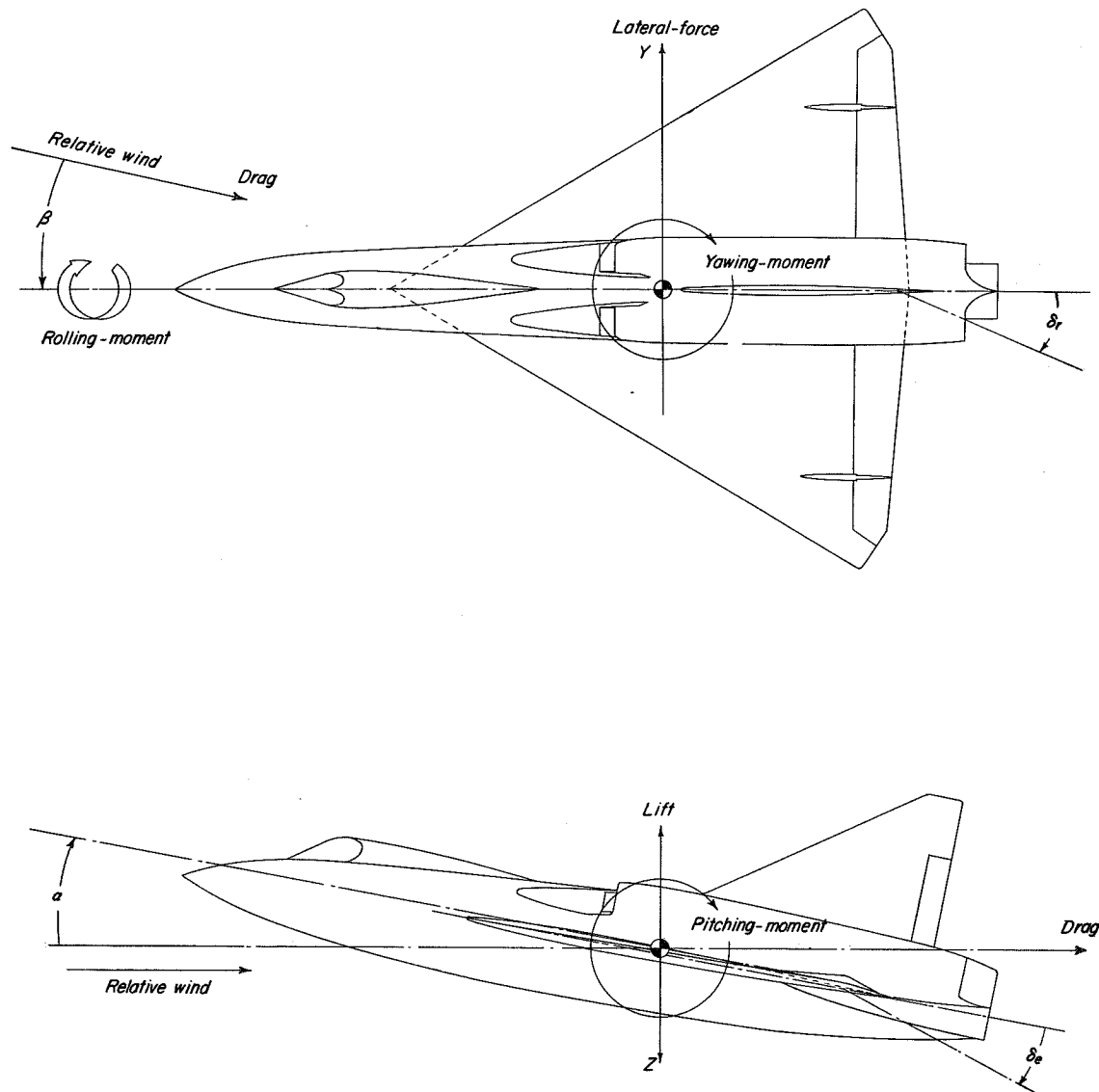


Figure 1.- System of axes used. Positive direction of forces, moments, and angles is indicated by arrows.

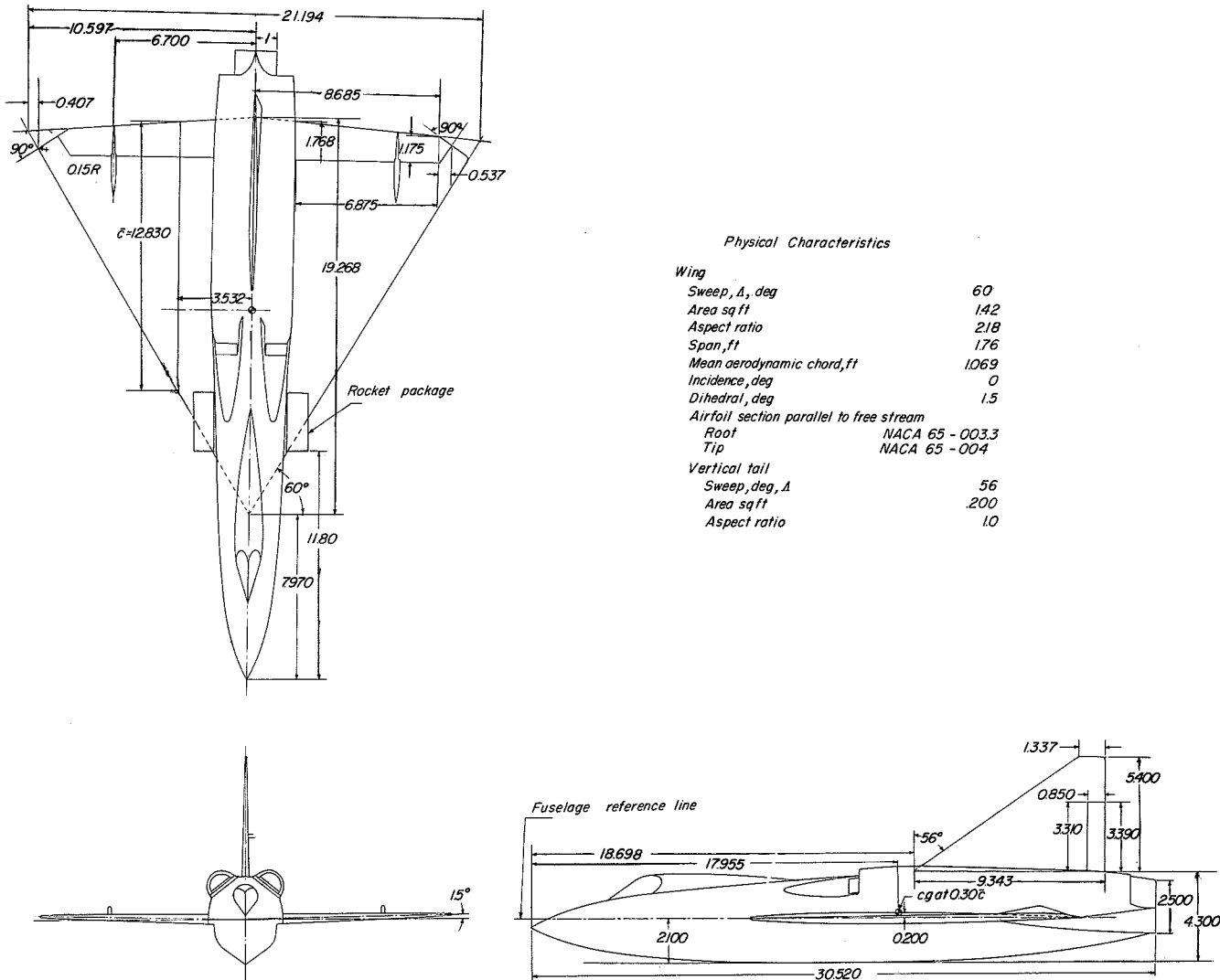


Figure 2.- General arrangement of test model. All dimensions are in inches.

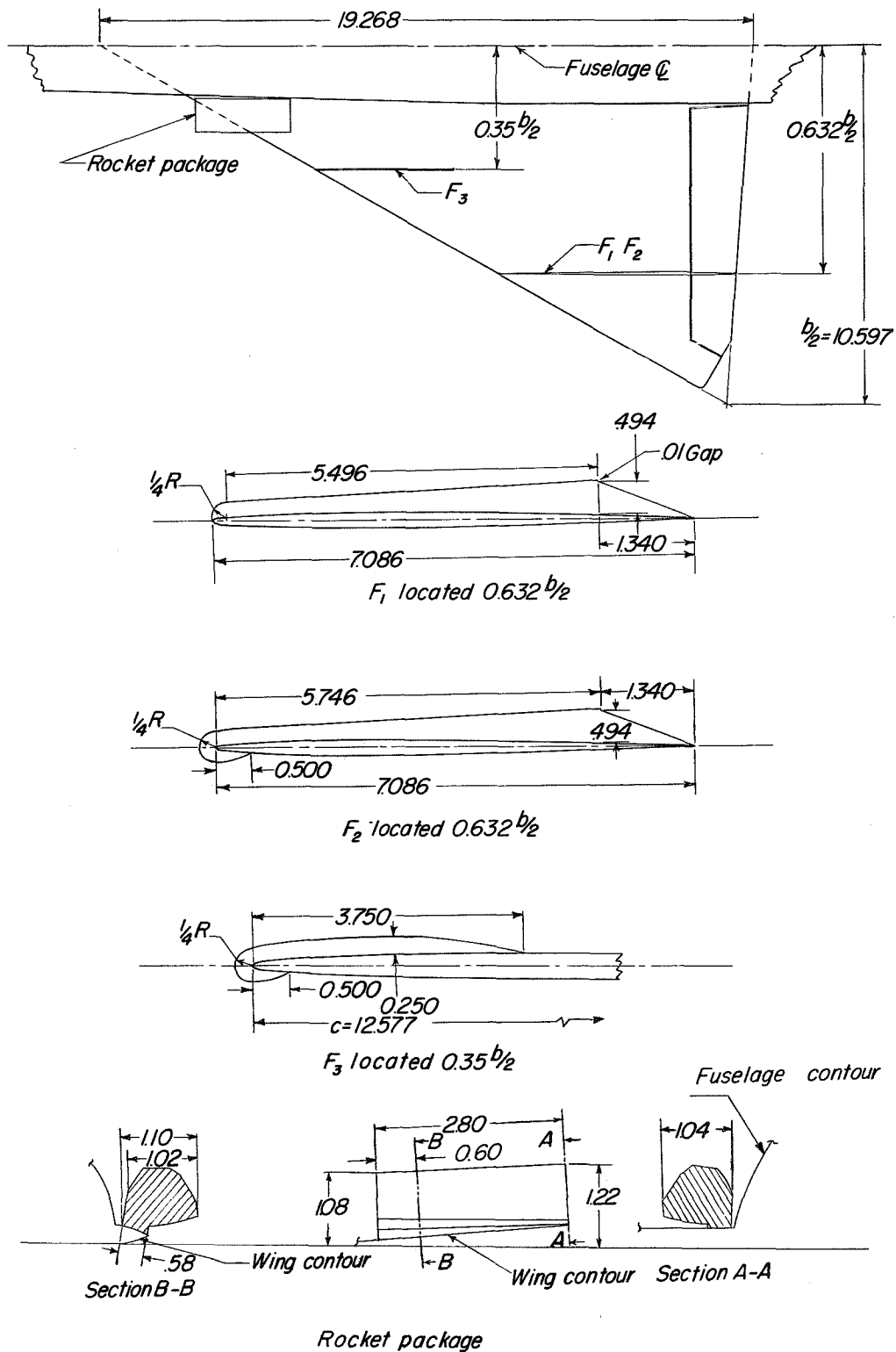
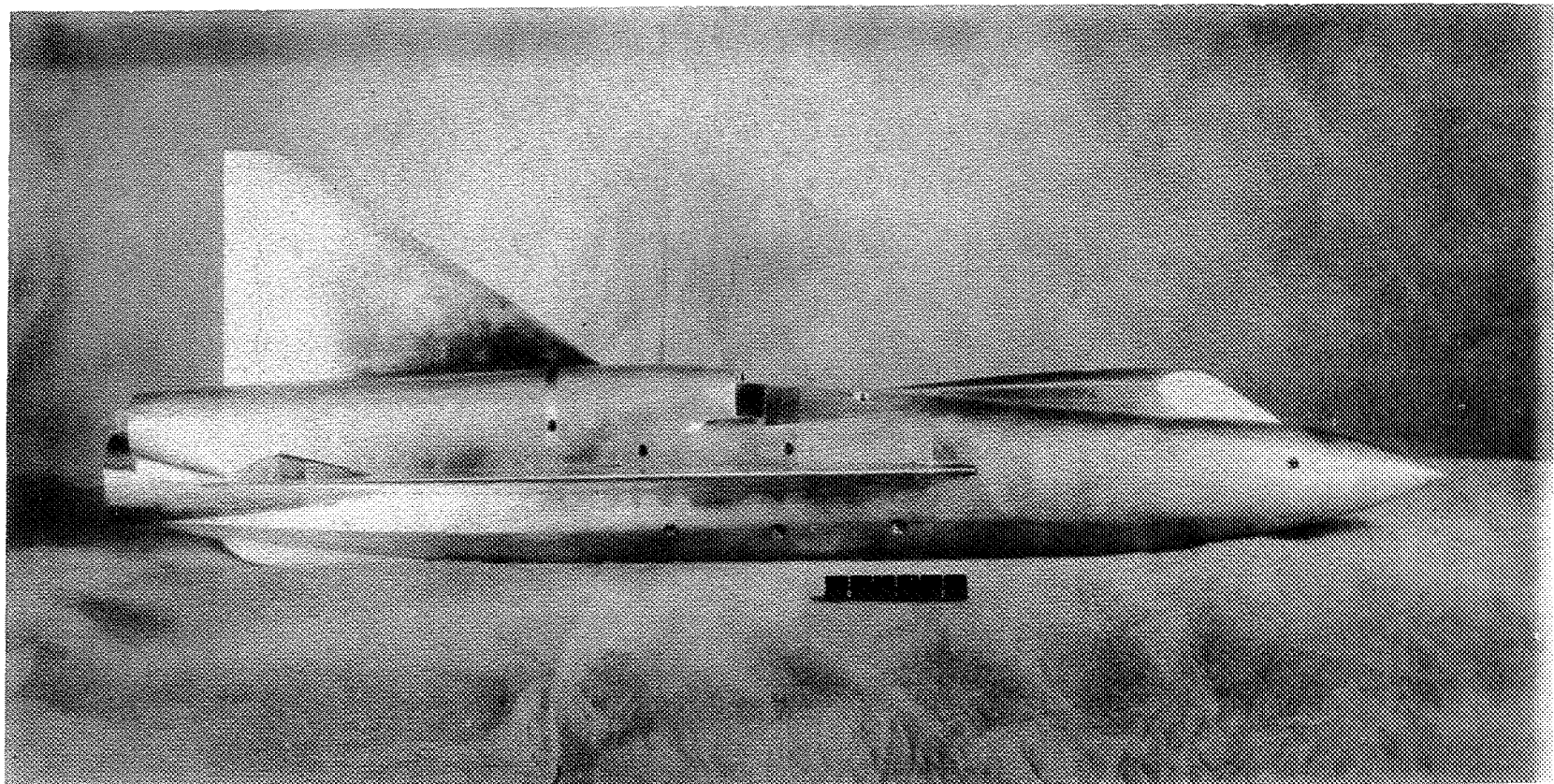


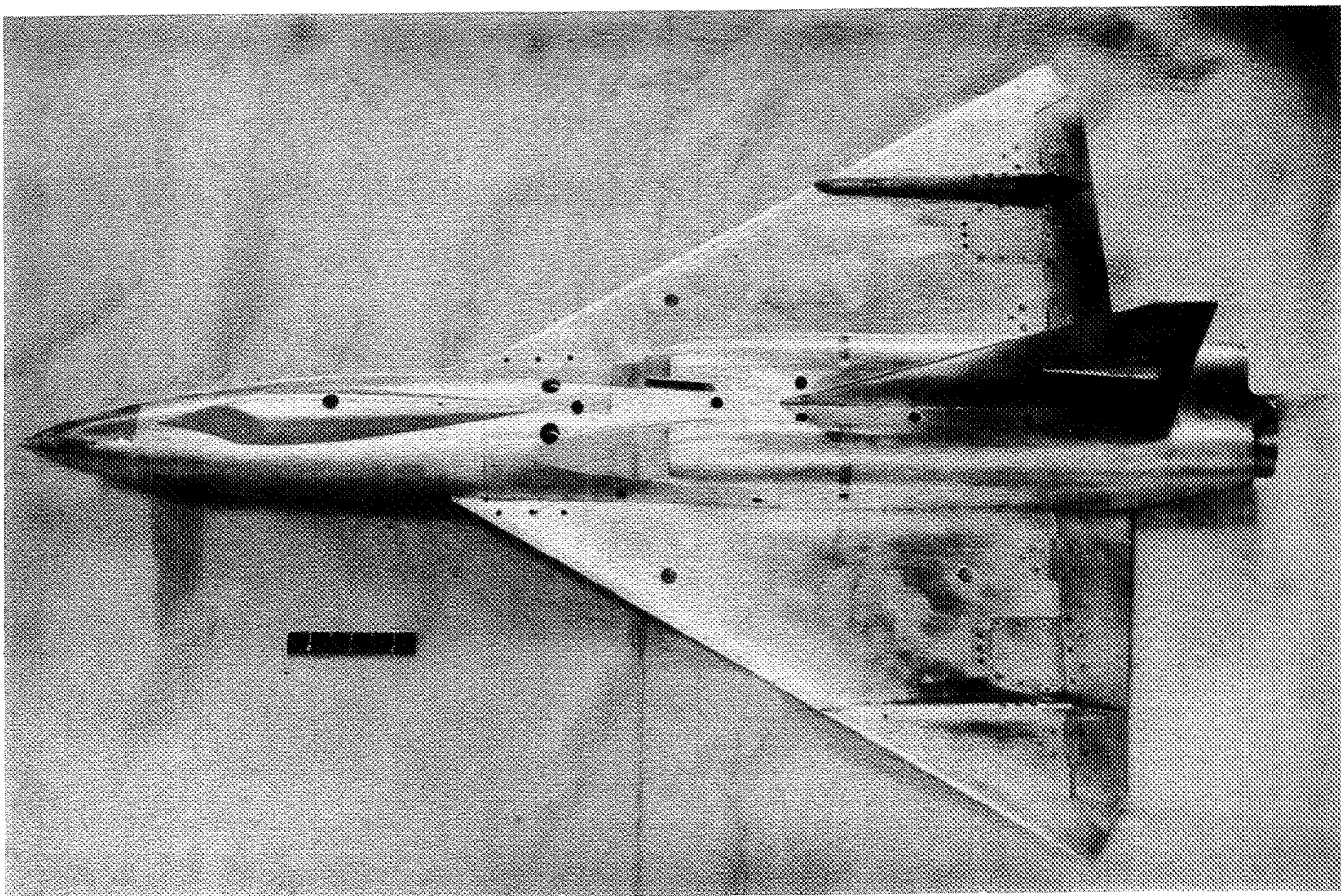
Figure 3.- Details of various fence configurations and rocket package.
All dimensions are in inches.



(a) Configuration BCWV; $\delta_e = 0^\circ$, $\delta_r = 0^\circ$. L-78678

Figure 4.- Photographs of test model.

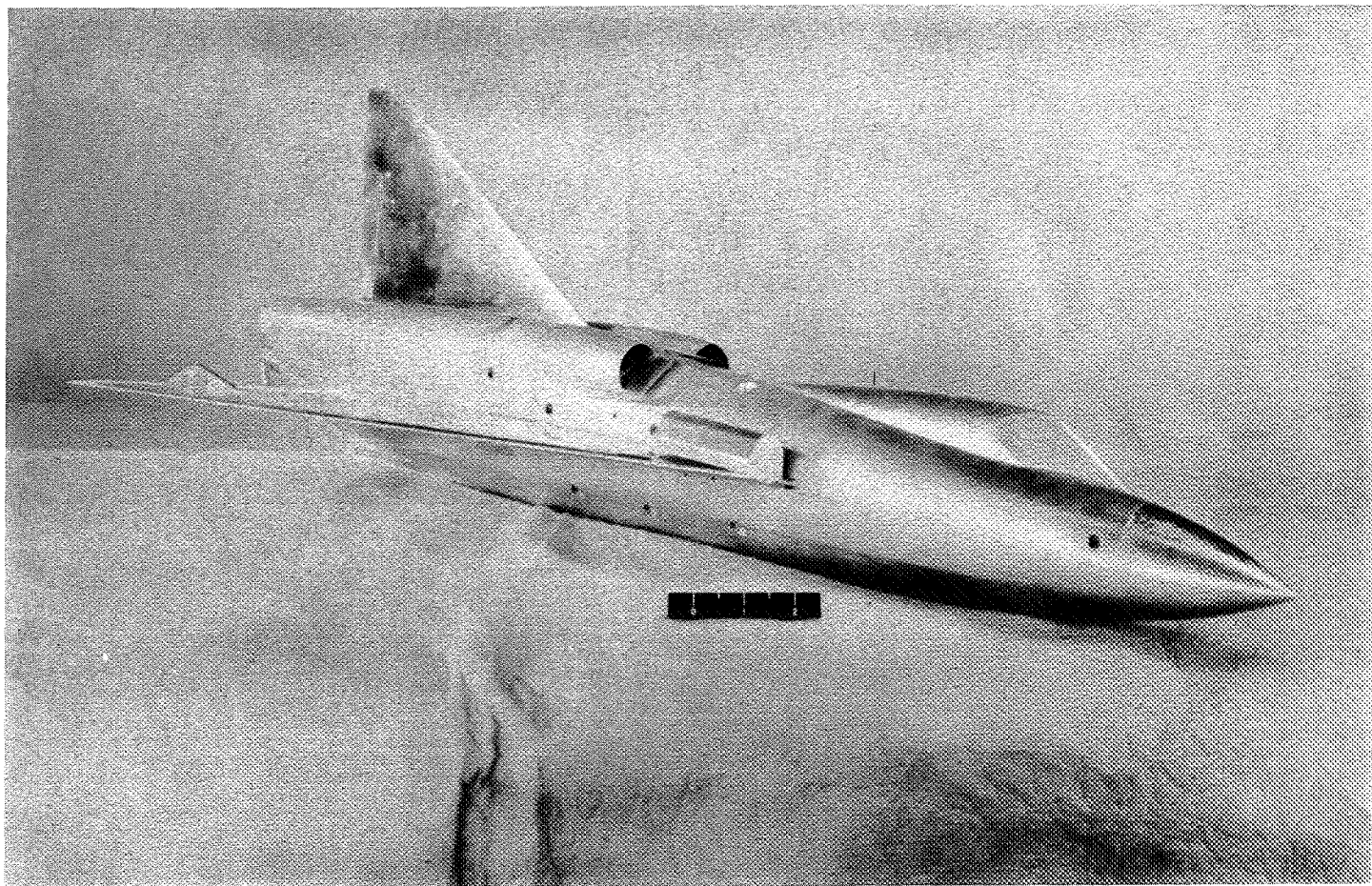
CONFIDENTIAL



L-78681

(b) Configuration $BCWF_1V$; $\delta_e = 0^\circ$, $\delta_r = 0^\circ$.

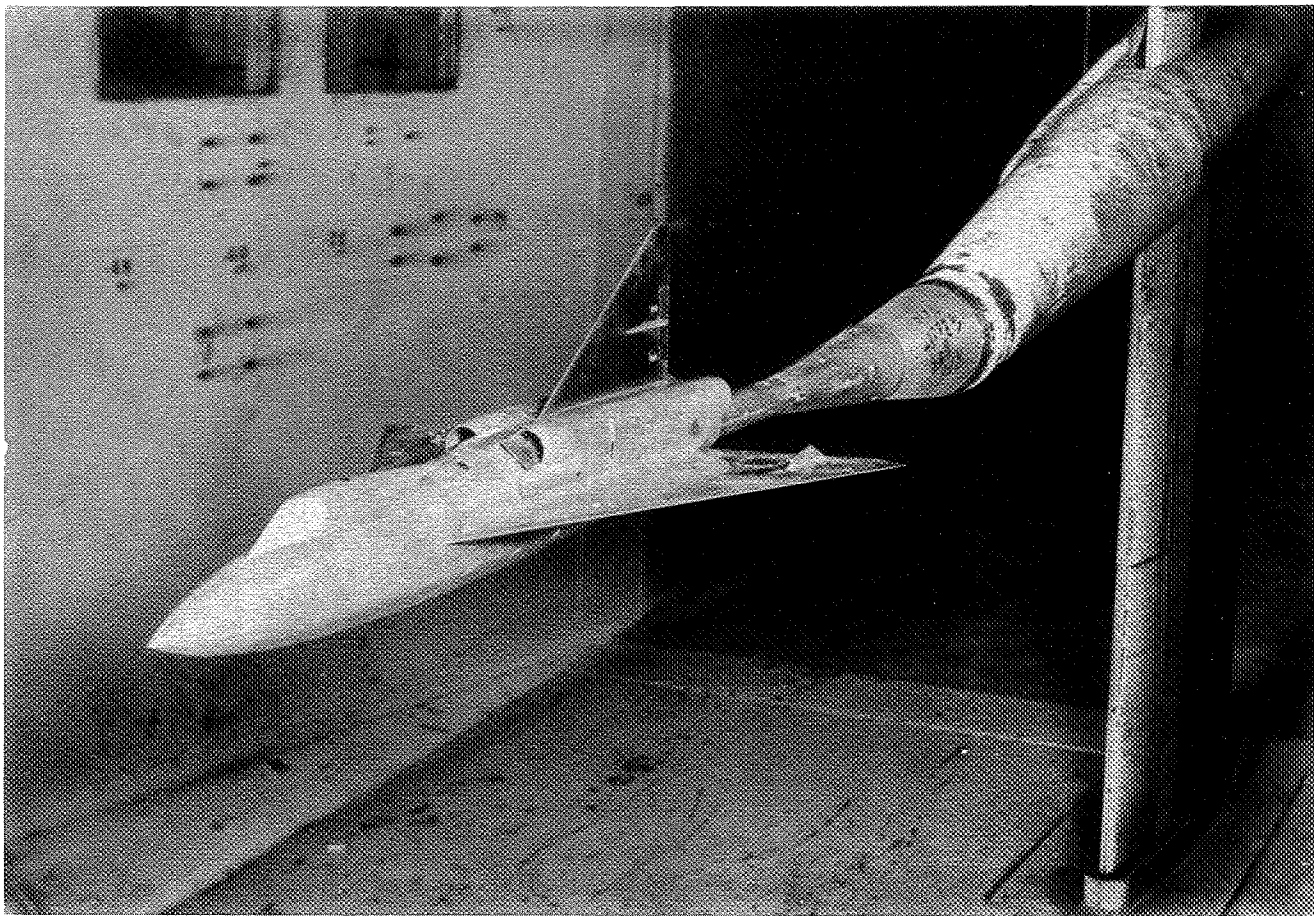
Figure 4--Continued.



L-78680

(c) Configuration BCW_{RP}V; $\delta_e = 0^\circ$, $\delta_r = 0^\circ$.

Figure 4.- Continued.



L-78683

(d) Configuration BCWV; $\delta_e = 0^\circ$, $\delta_r = 0^\circ$, mounted on
sting in Langley high-speed 7- by 10-foot tunnel.

Figure 4.- Concluded.

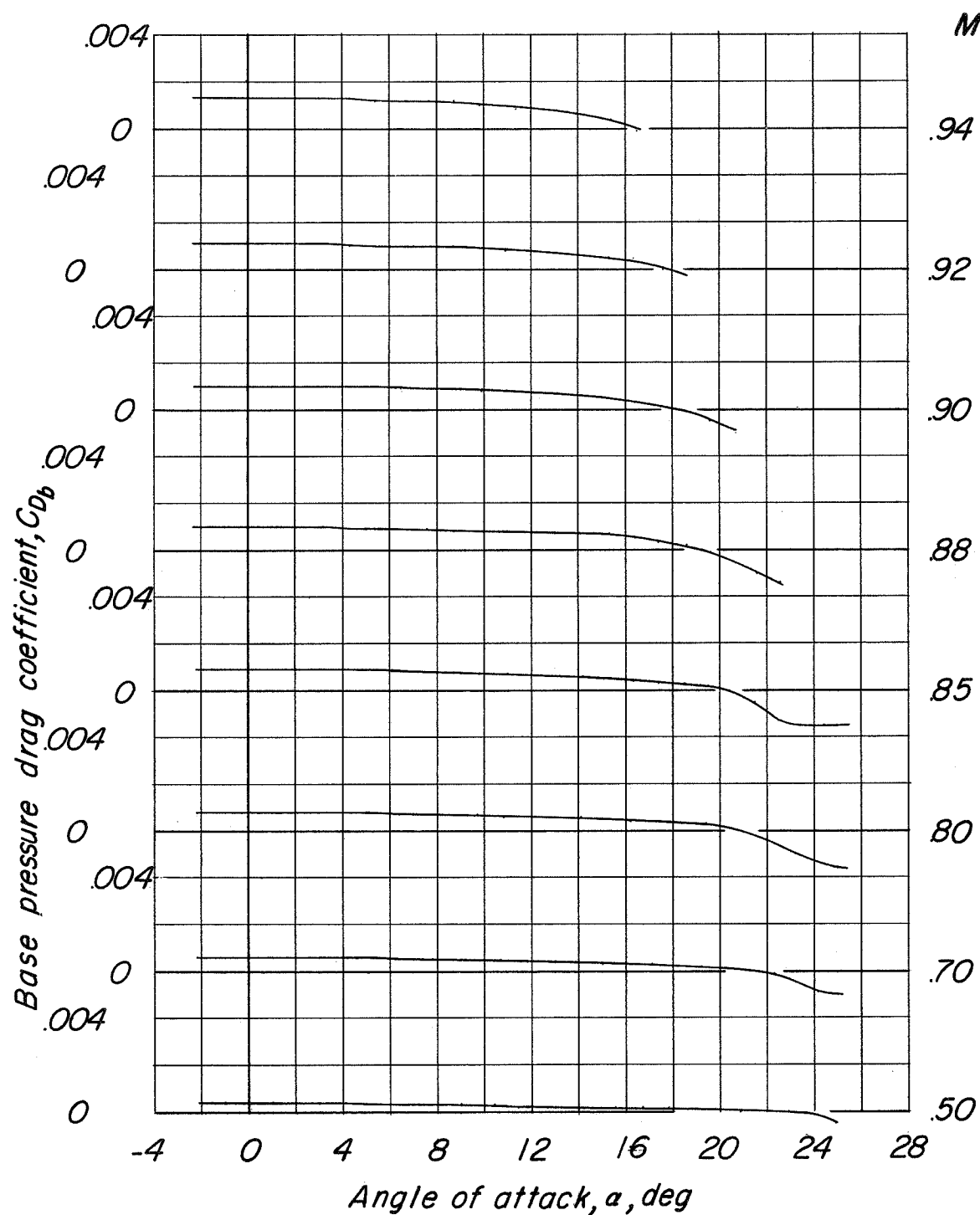


Figure 5.- Variation of base pressure drag coefficient with angle of attack and test Mach number.

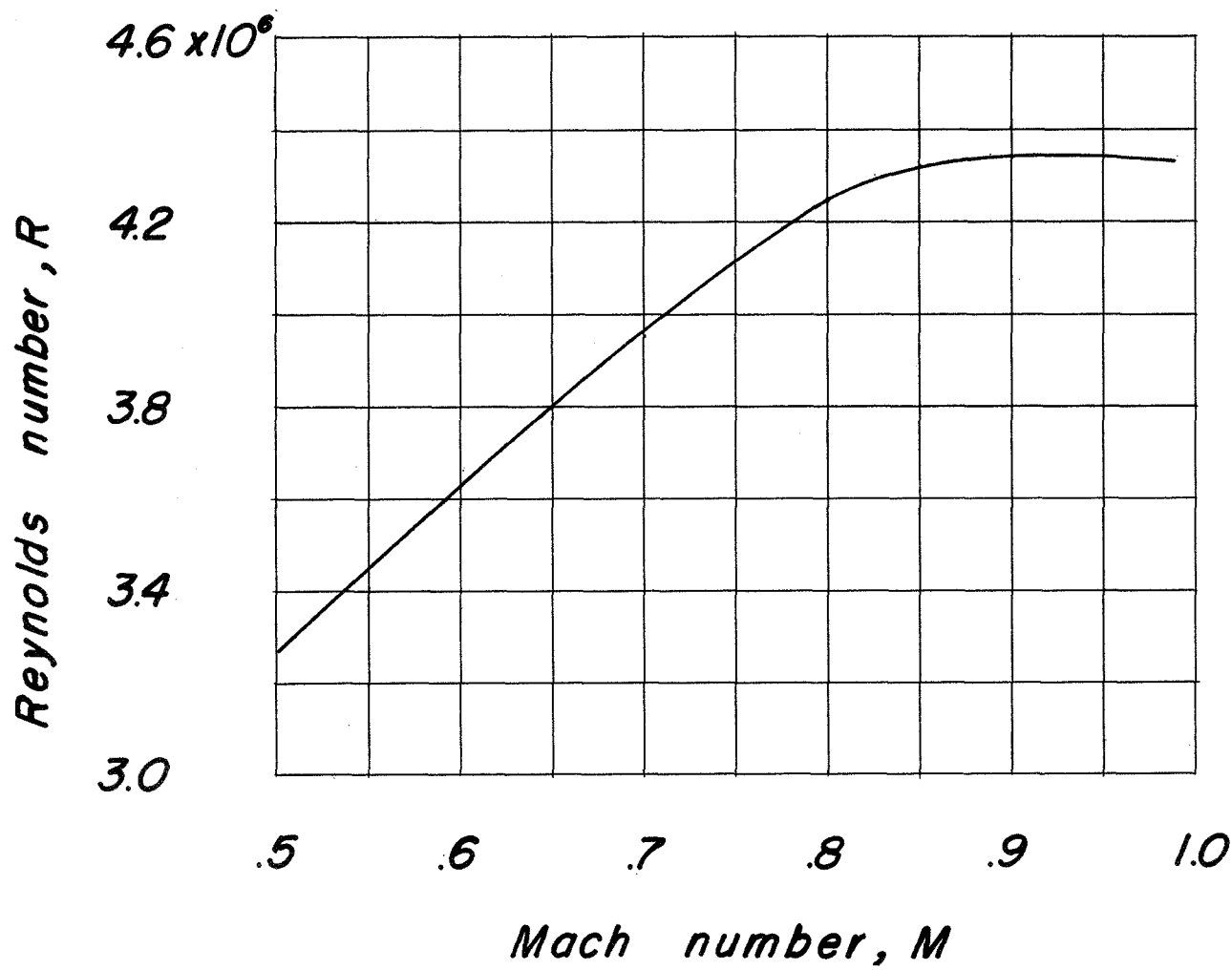


Figure 6.- Variation of test Reynolds number with Mach number based on wing mean aerodynamic chord.

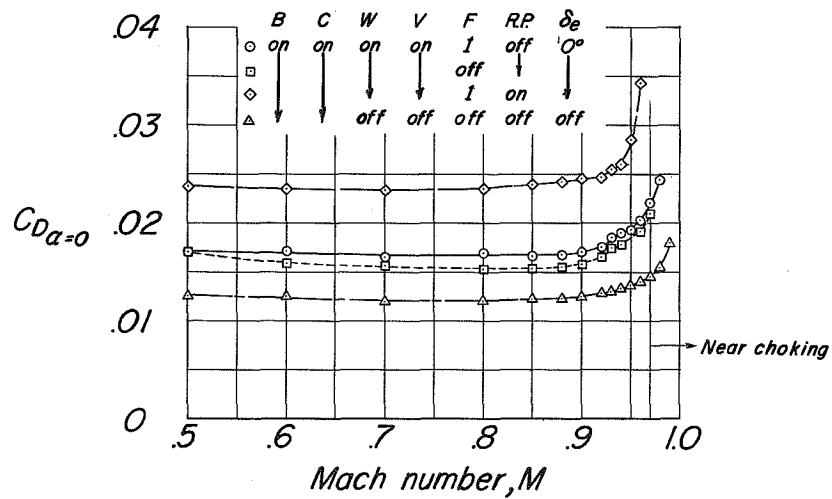
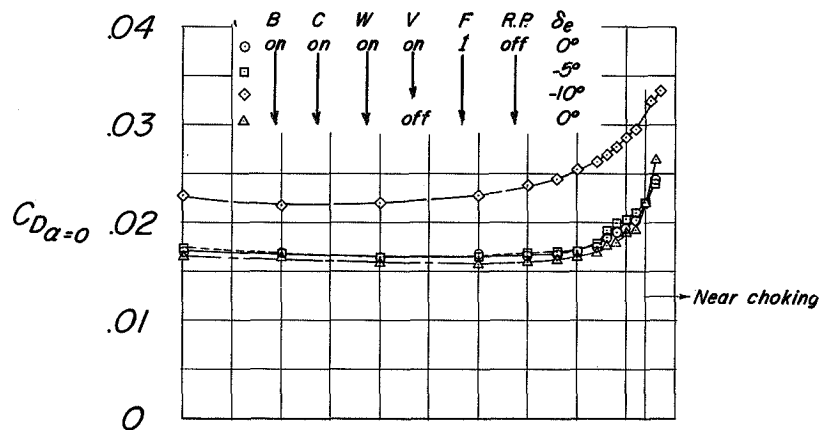
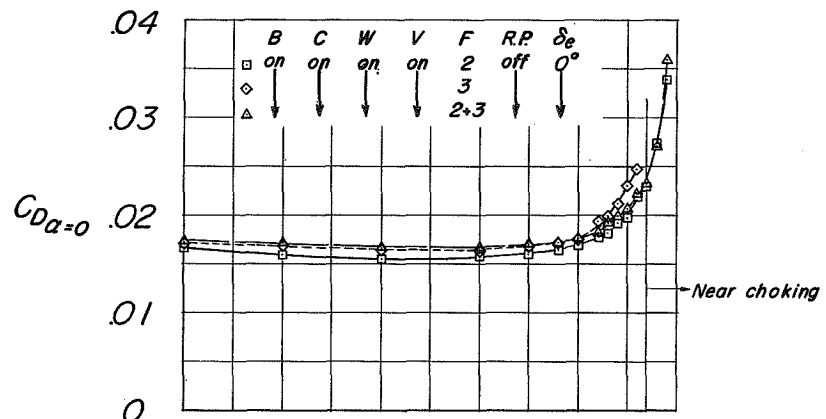


Figure 7.- Drag at zero angle of attack for 10 configurations investigated.

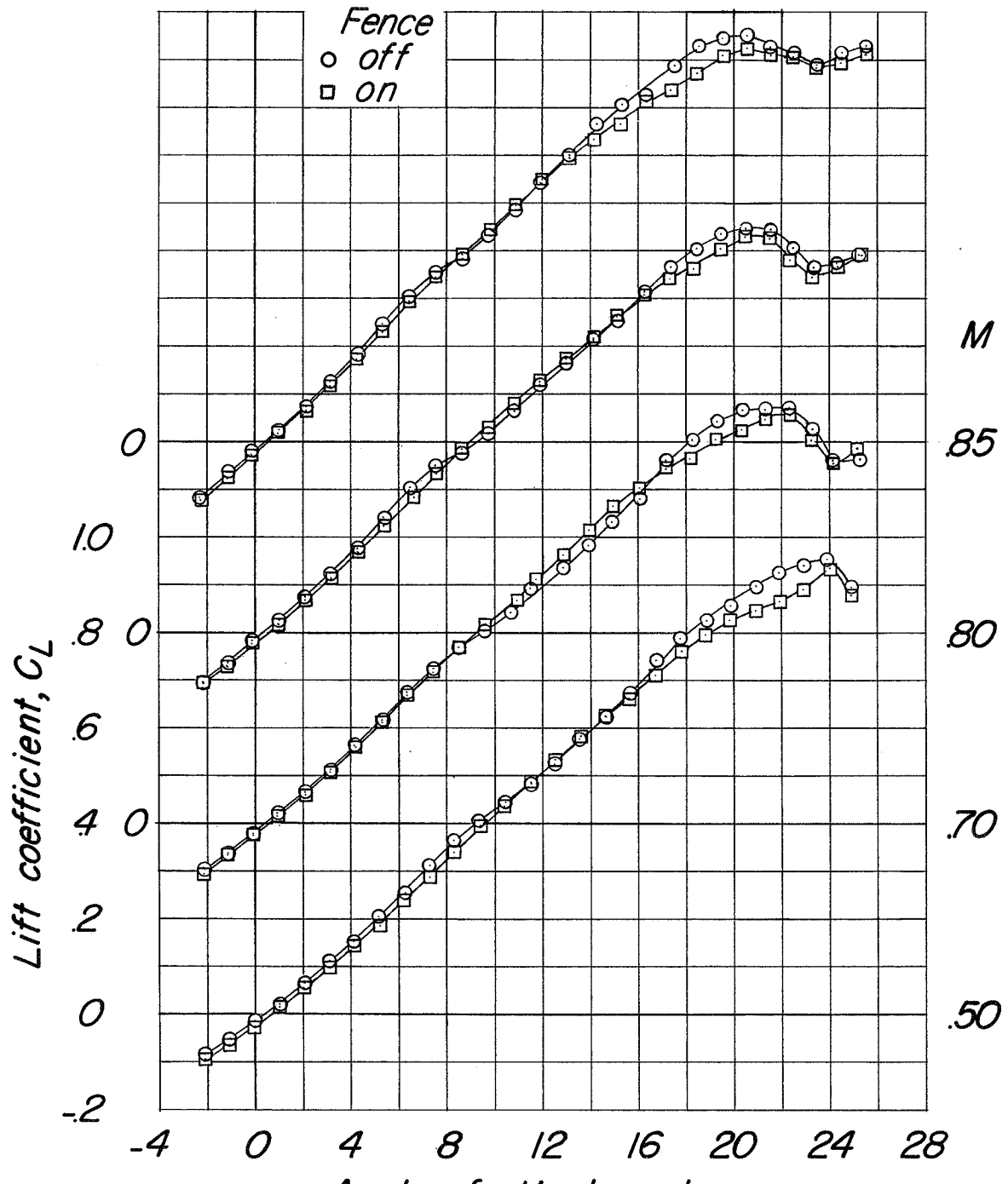
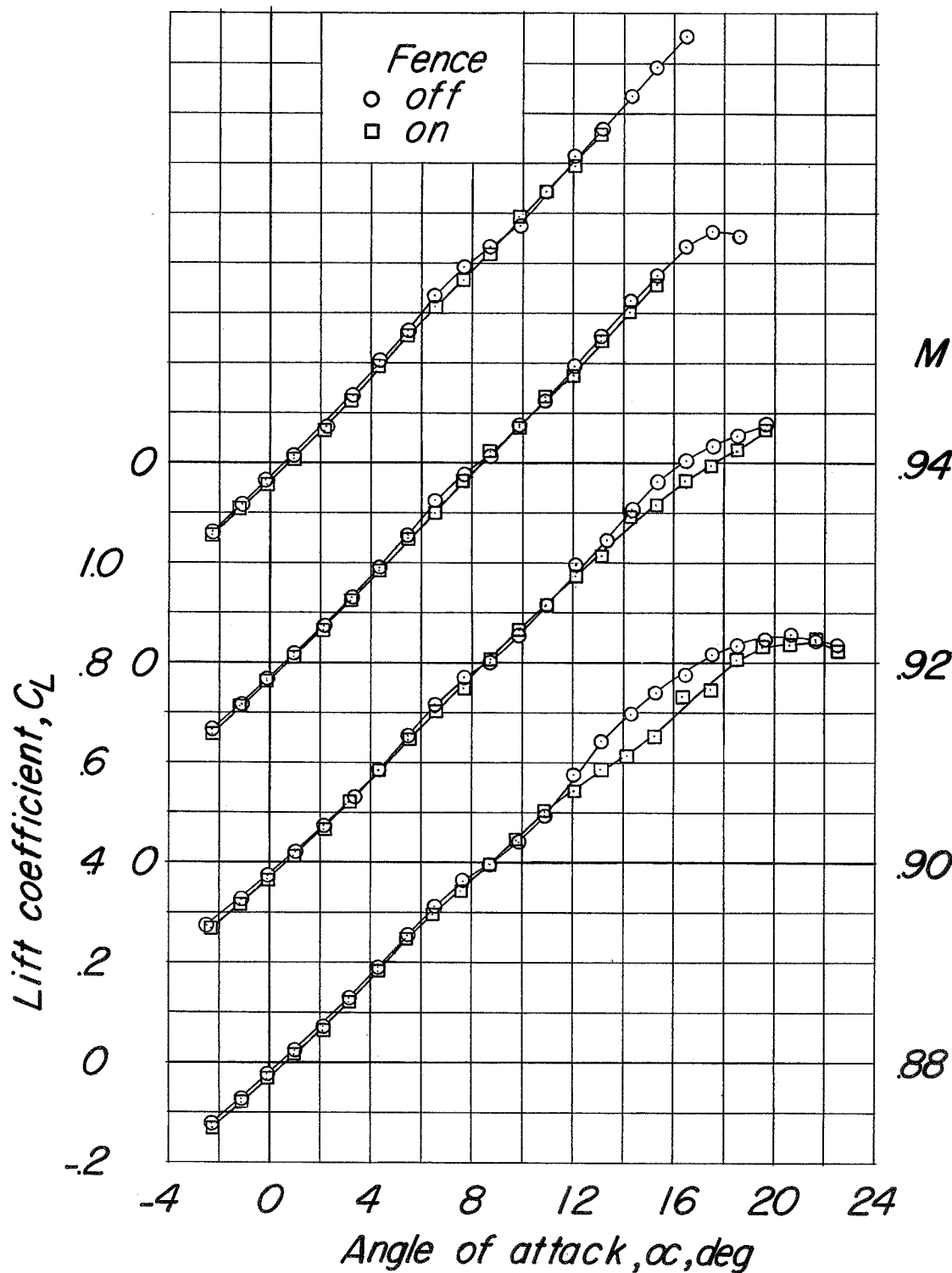
(a) C_L against α .

Figure 8.- Basic longitudinal characteristics for configuration BCWV,
 $\delta_e = 0^\circ$, $\delta_r = 0^\circ$, with and without fence 1.



(a) Concluded.

Figure 8.- Continued.

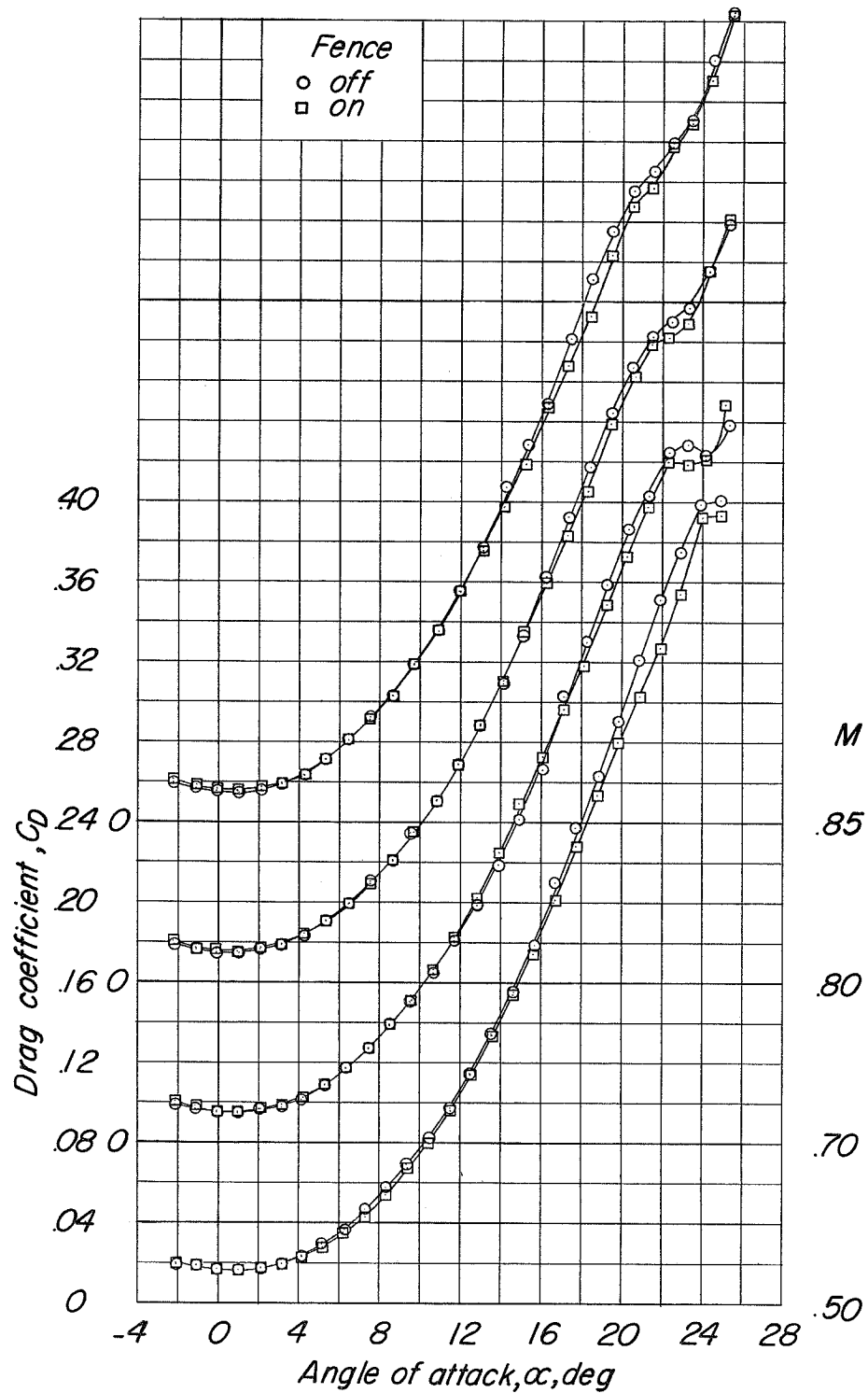
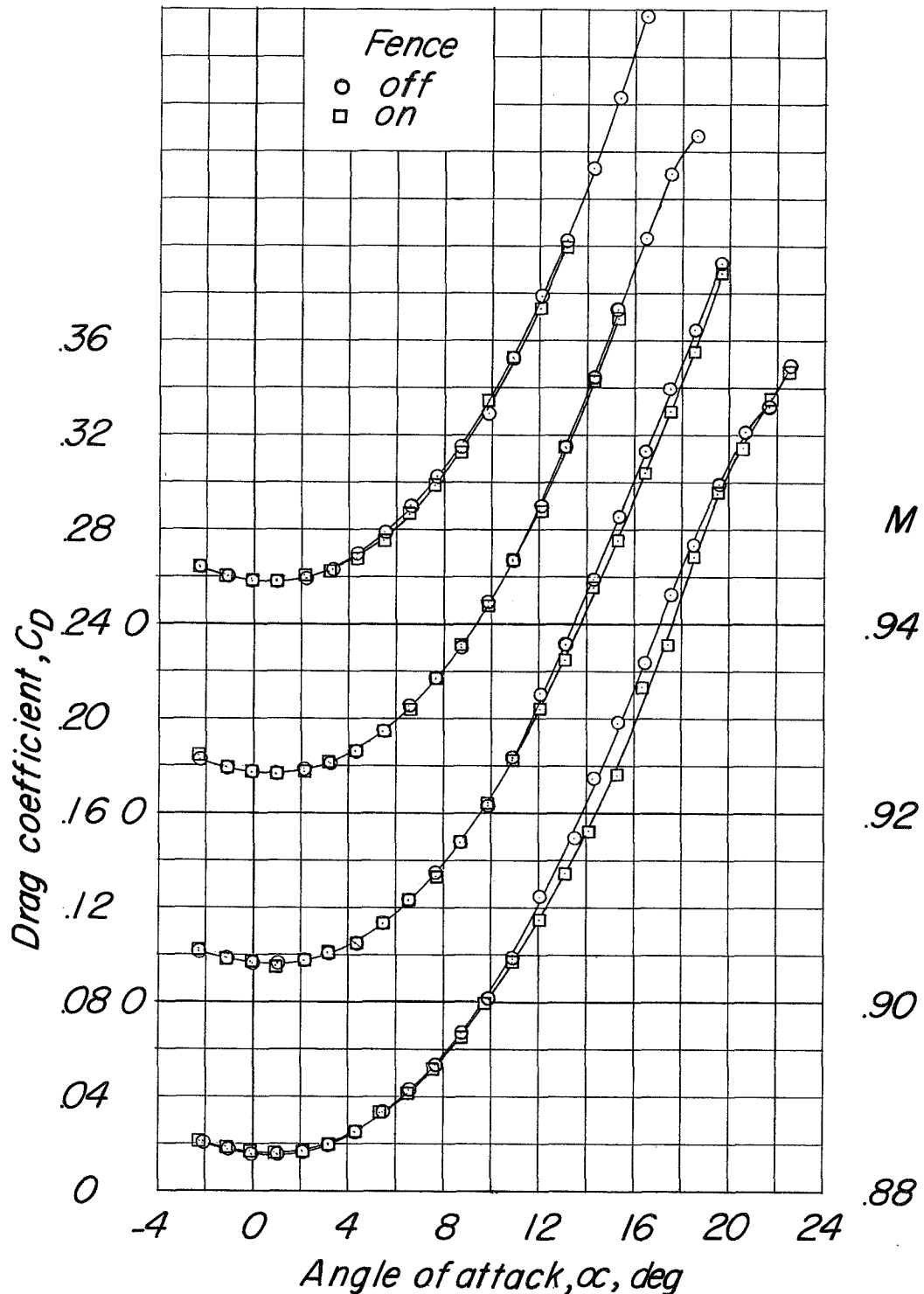
(b) C_D against α .

Figure 8.- Continued.



(b) Concluded.

Figure 8.- Continued.

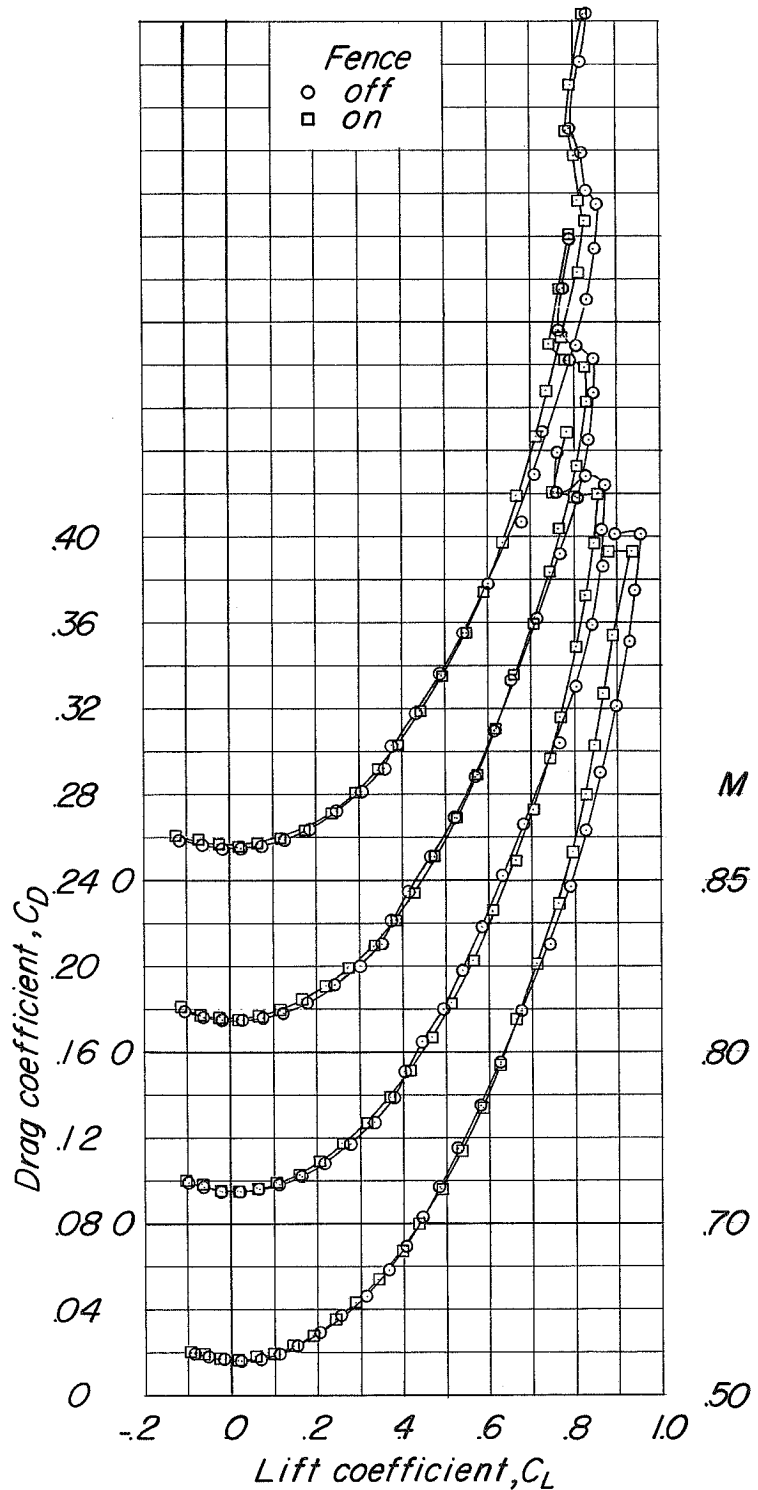
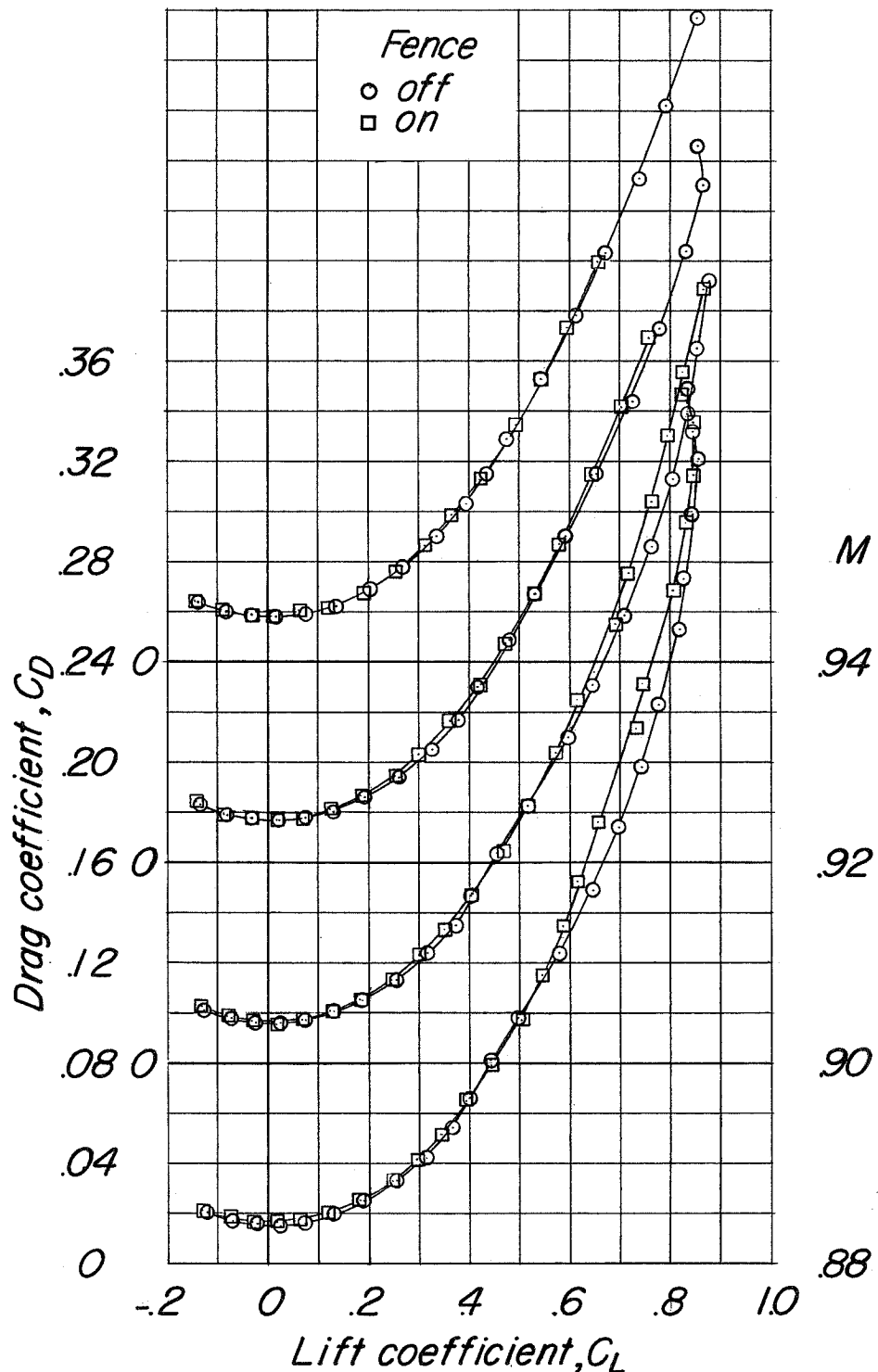
(c) C_D against C_L .

Figure 8.- Continued.



(c) Concluded.

Figure 8.- Continued.

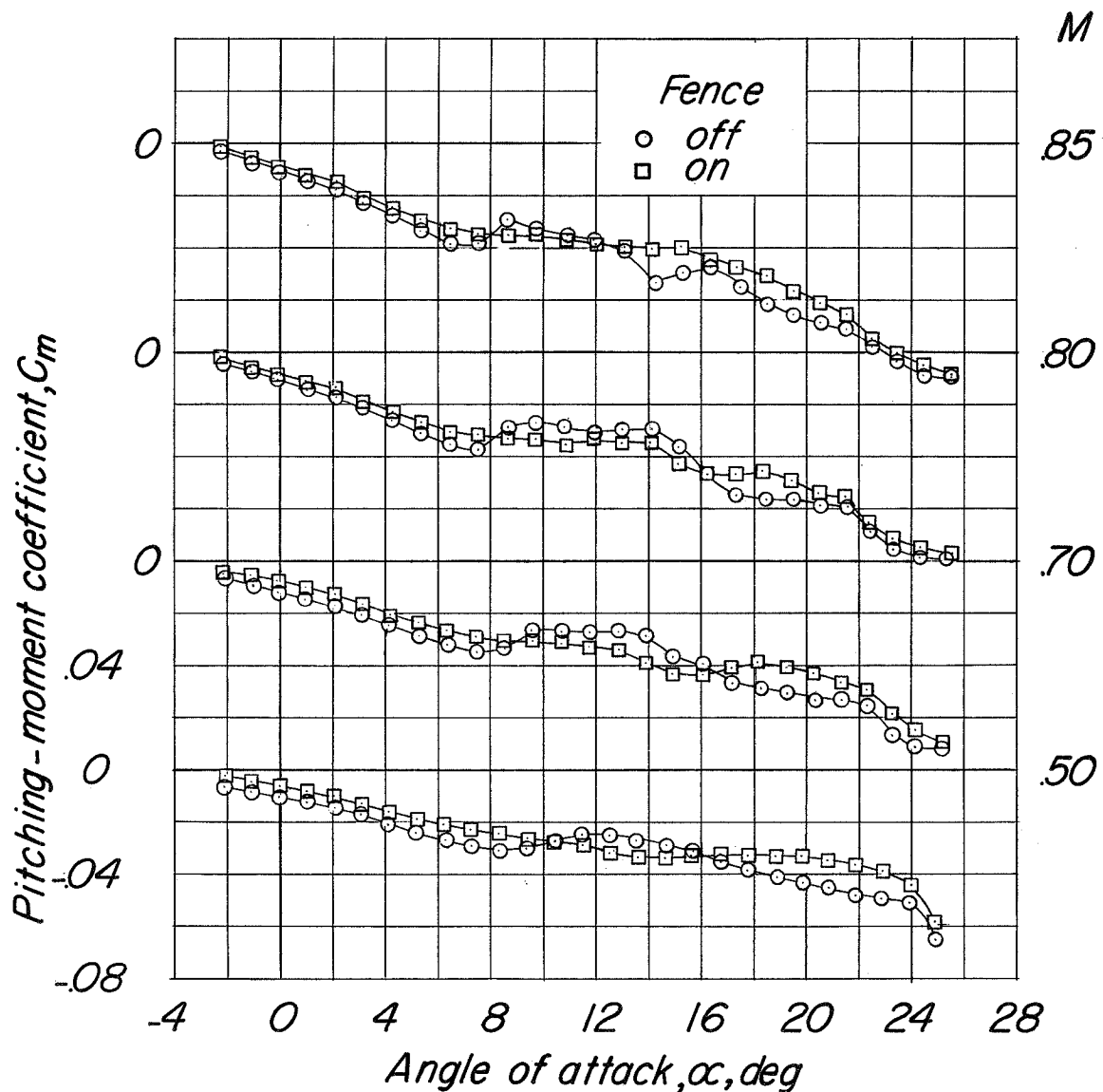
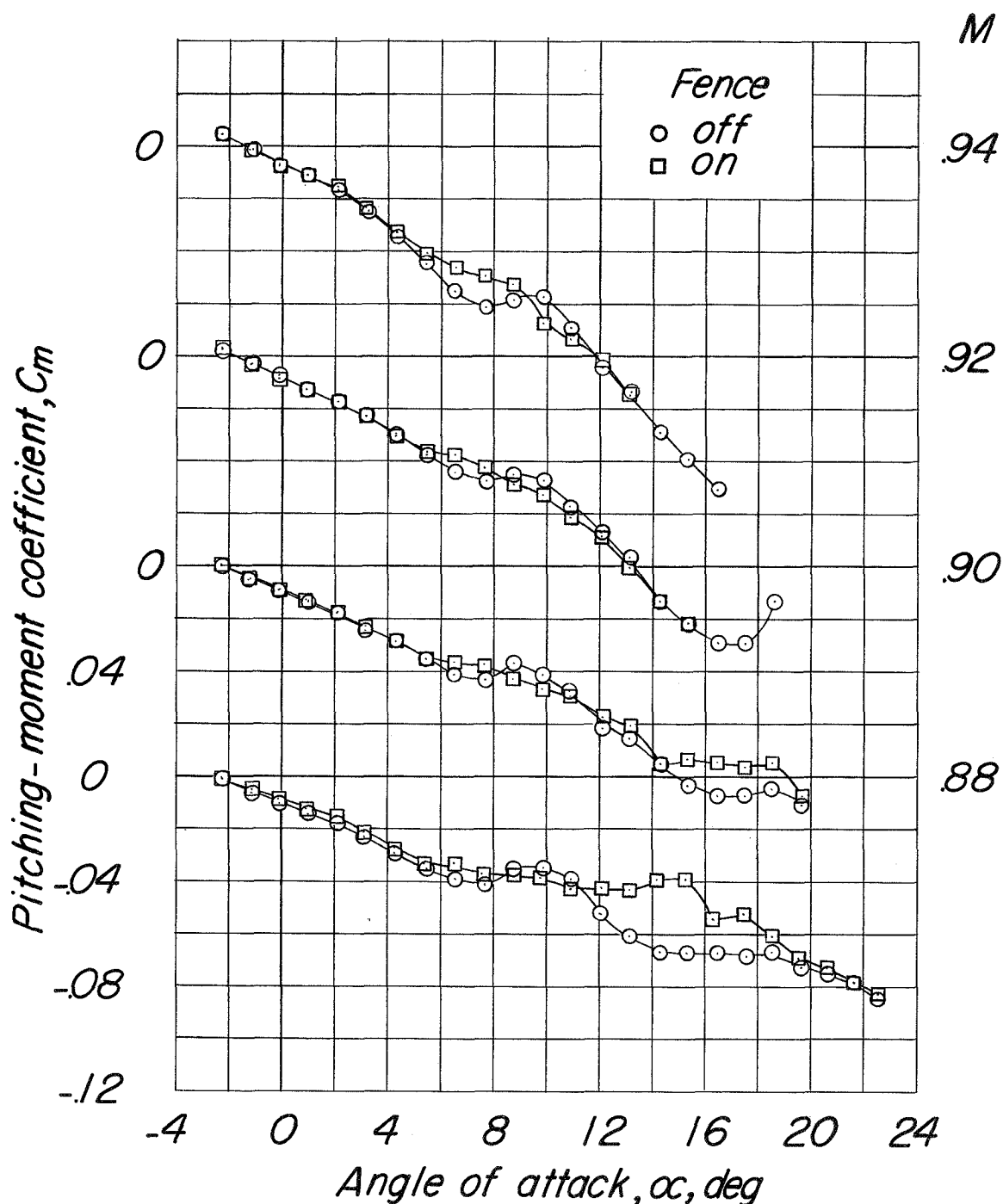
(d) C_m against α .

Figure 8-- Continued.



(d) Concluded.

Figure 8.- Continued.

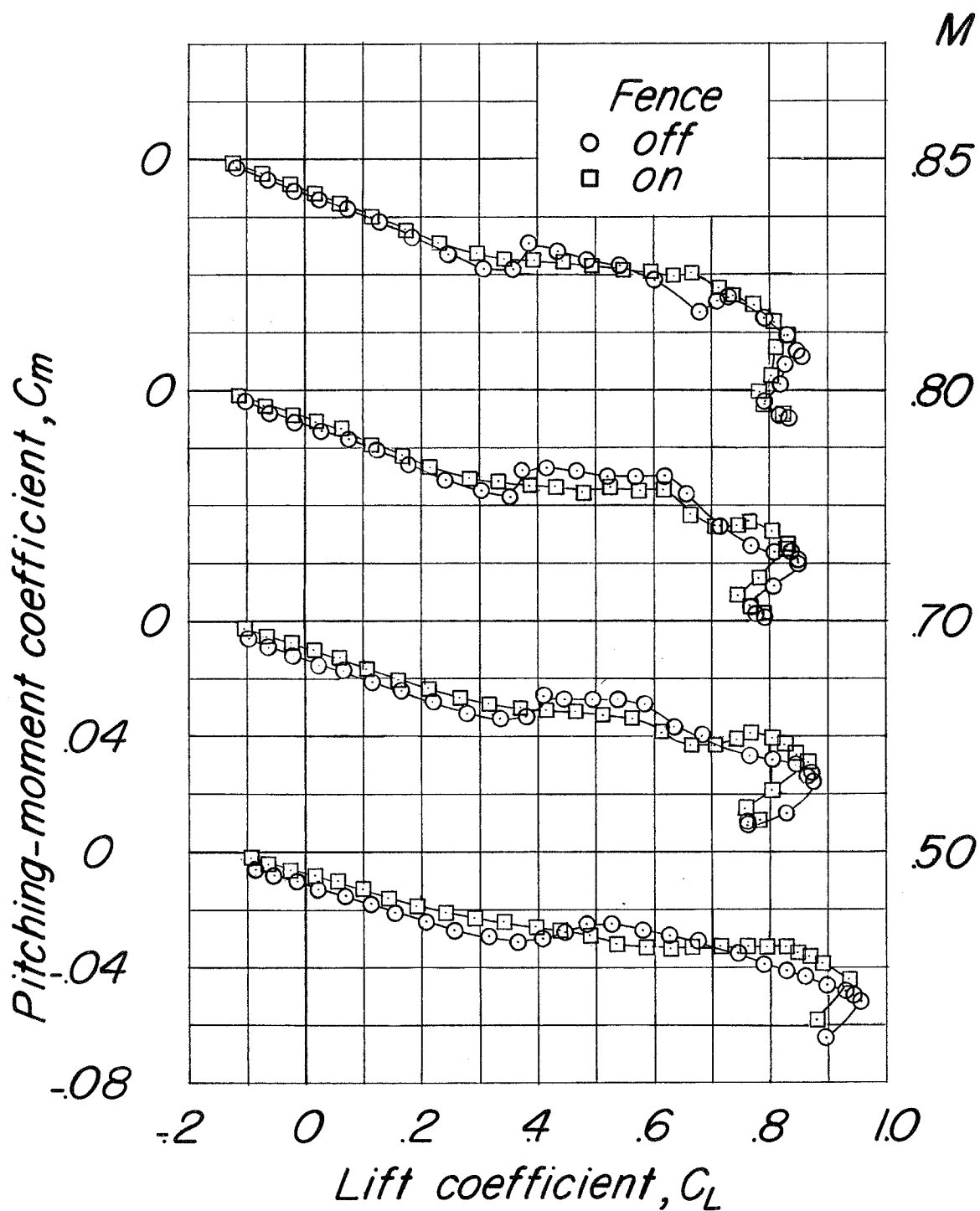
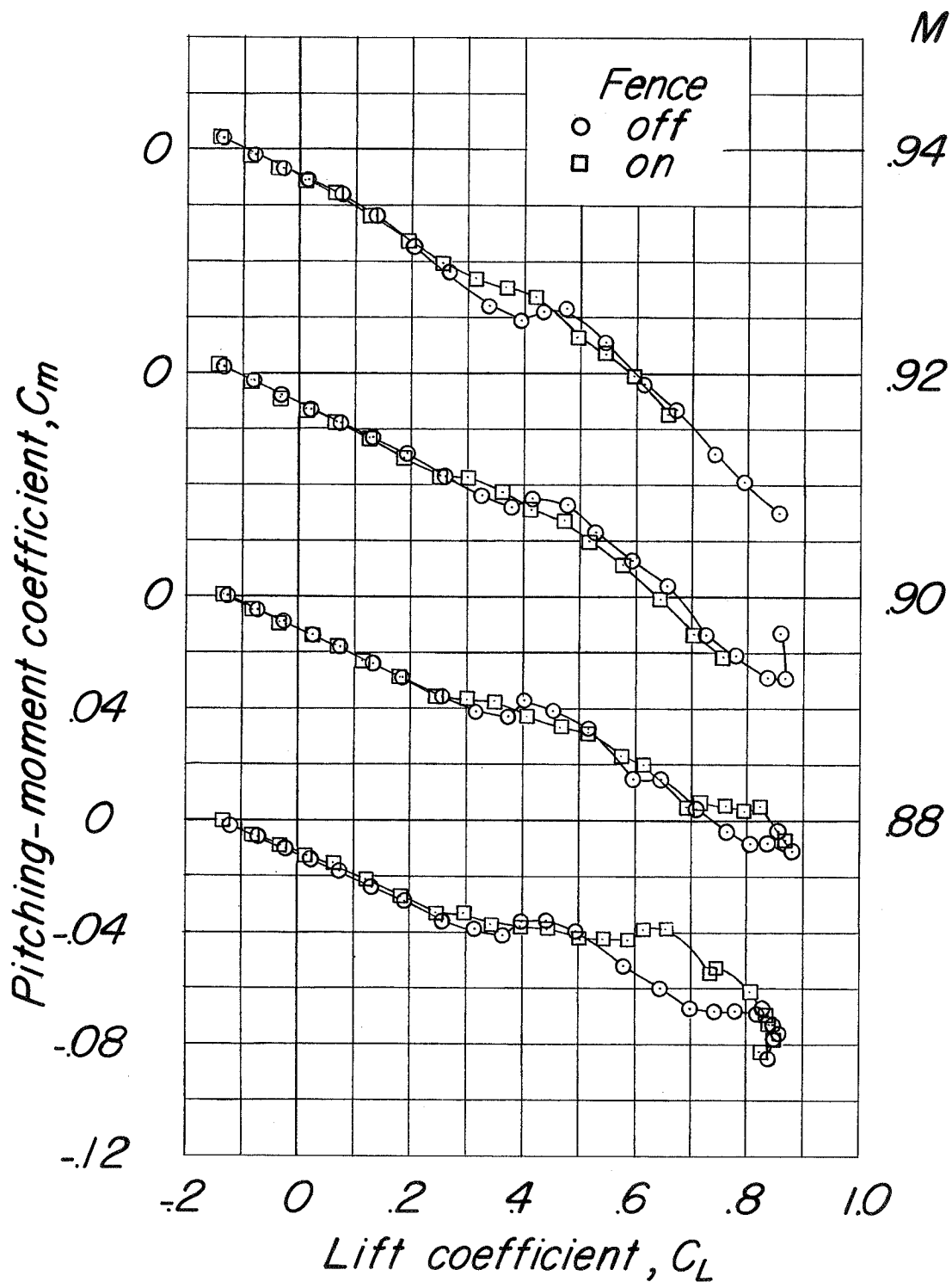
(e) C_m against C_L .

Figure 8.- Continued.



(e) Concluded.

Figure 8.- Concluded.

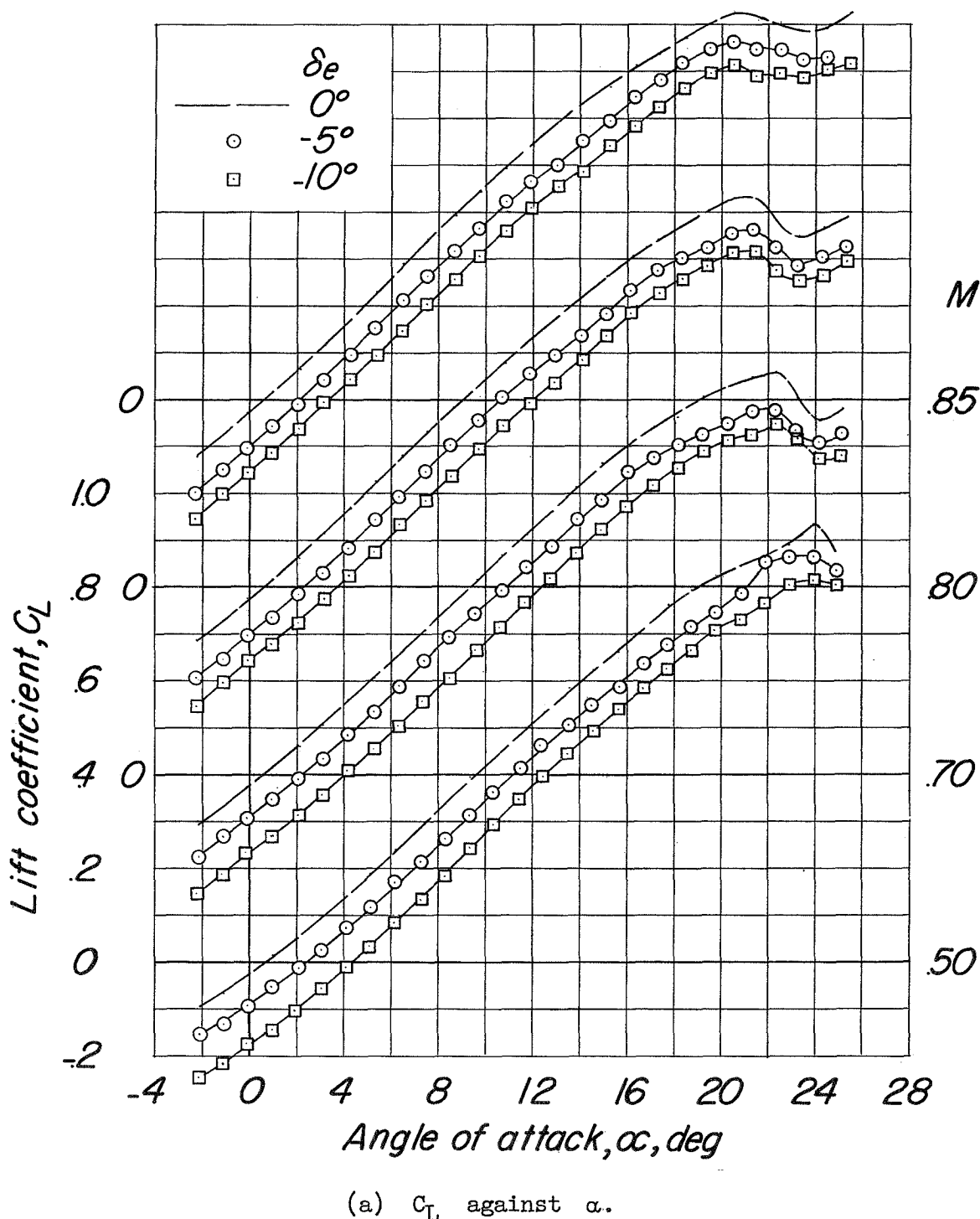
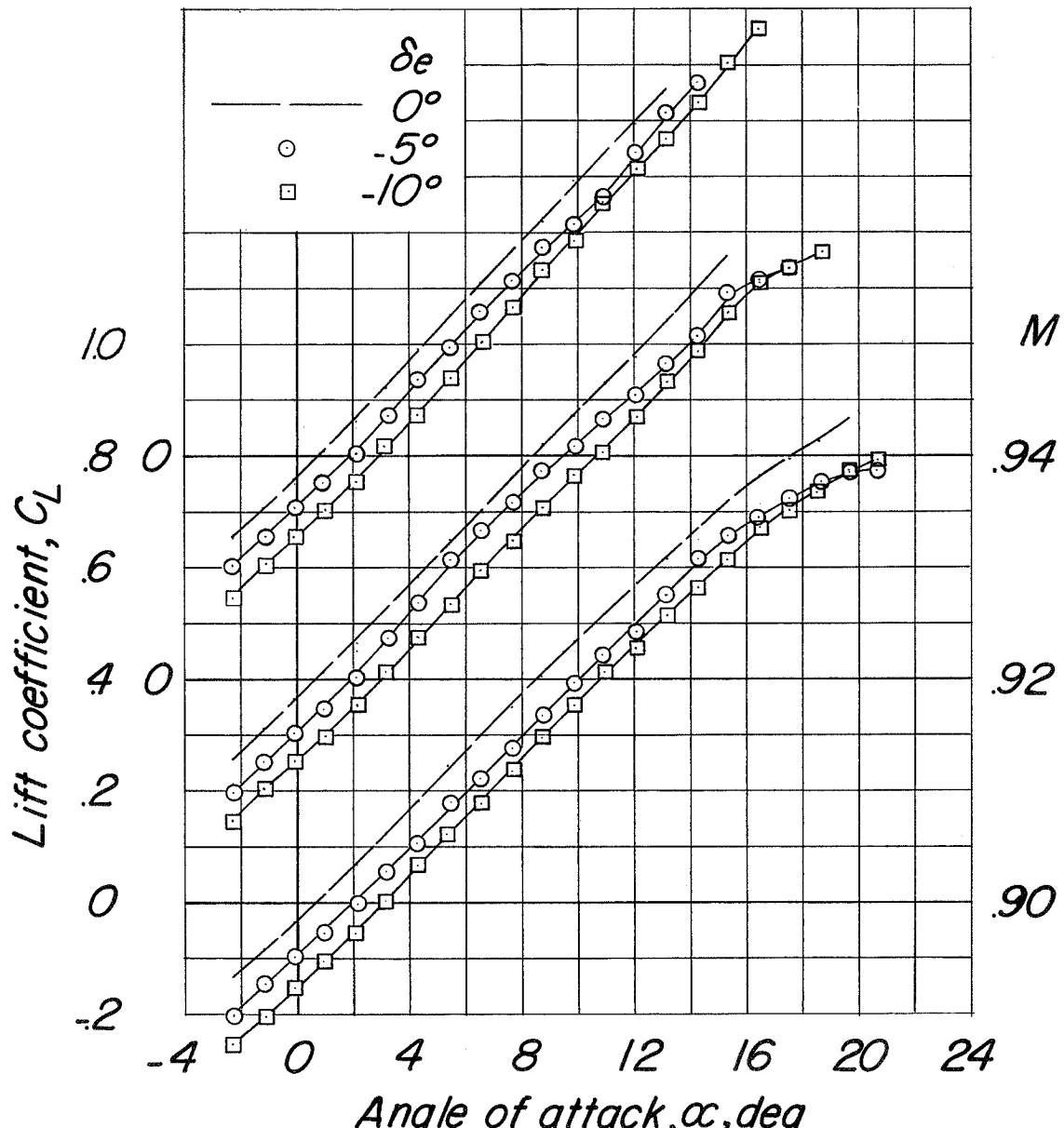


Figure 9.- Basic longitudinal characteristics for configuration BCWF₁V,
 $\delta_r = 0^\circ$.



(a) Concluded.

Figure 9.- Continued.

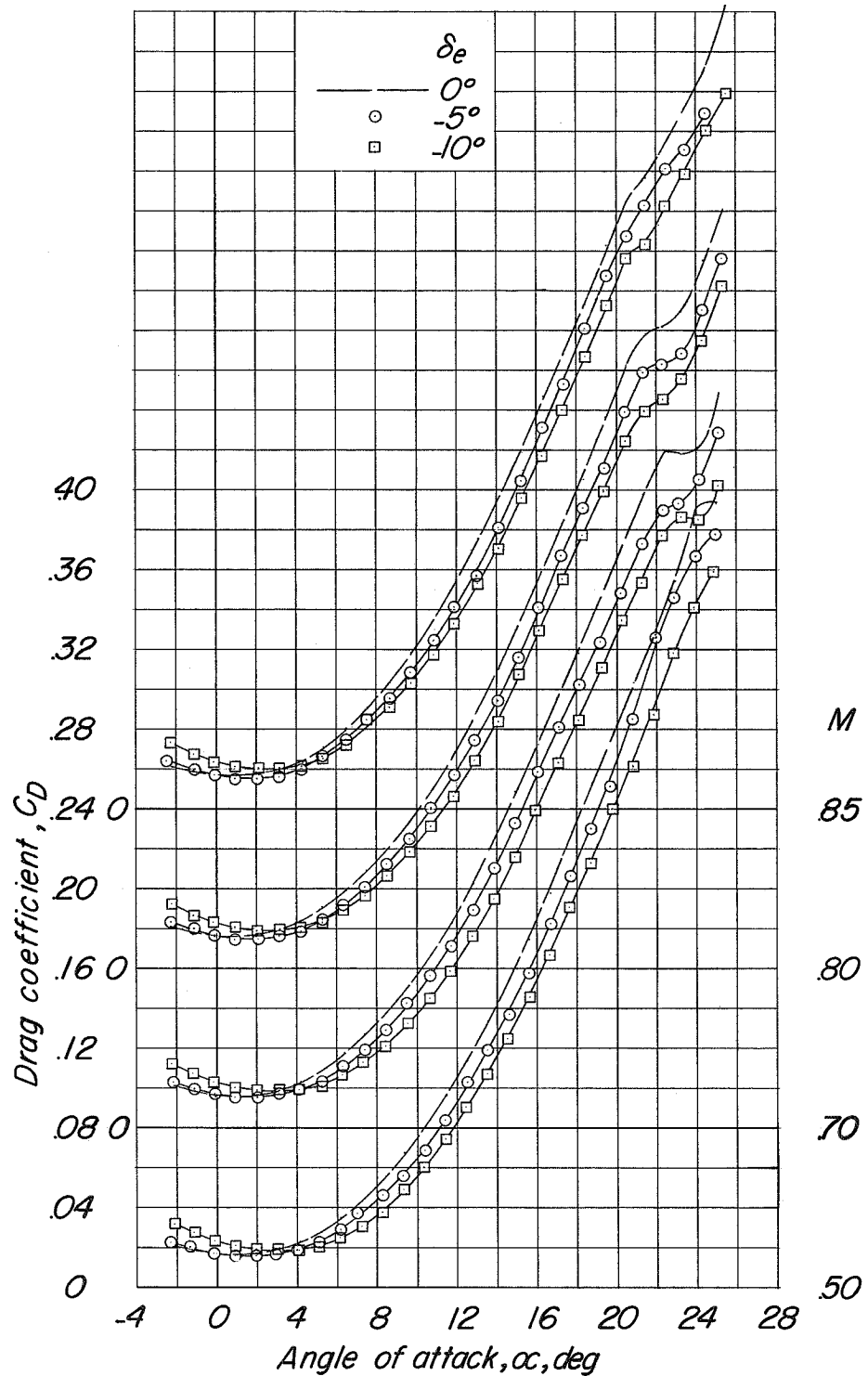
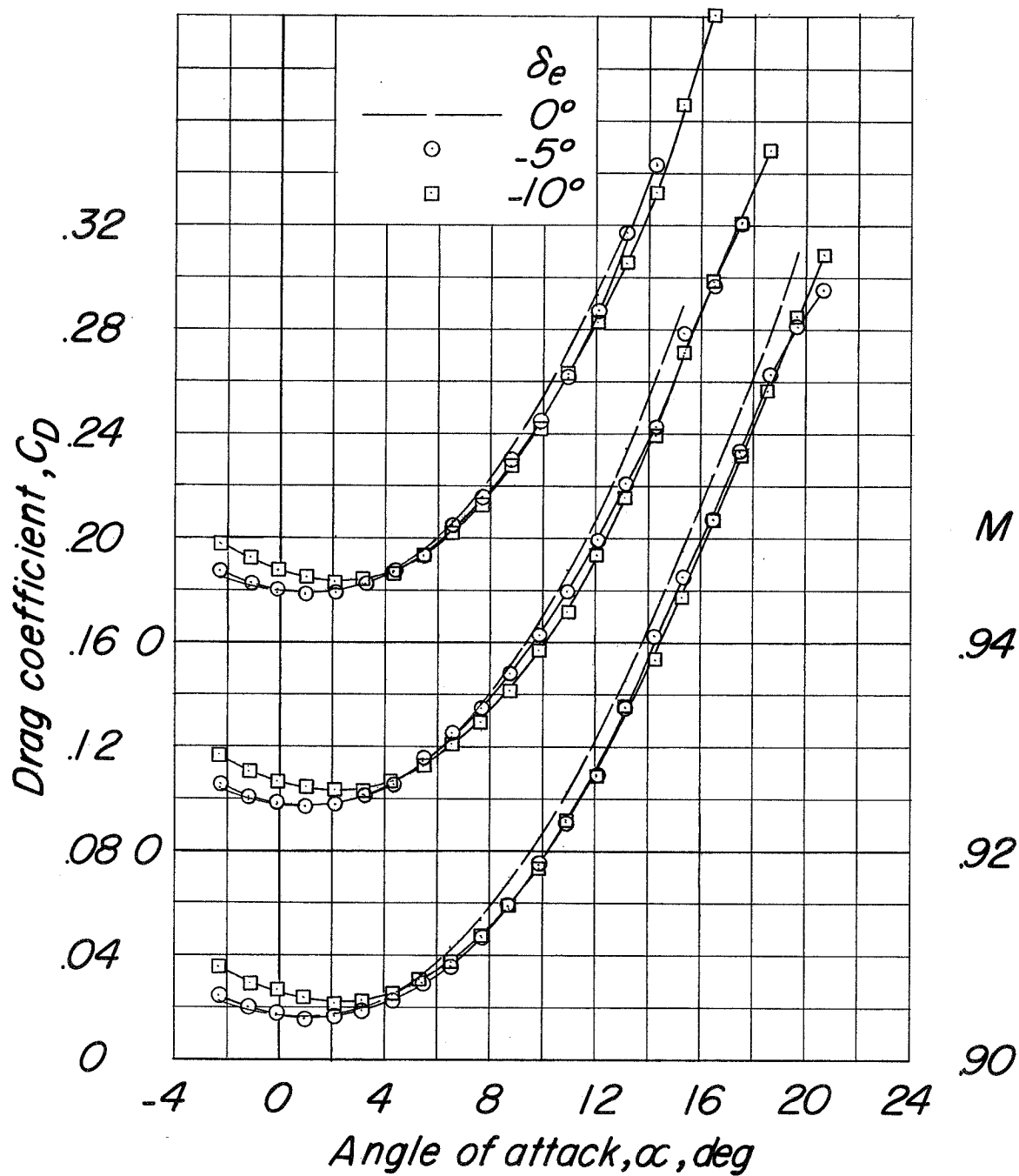
(b) C_D against α .

Figure 9.- Continued.



(b) Concluded.

Figure 9.- Continued.

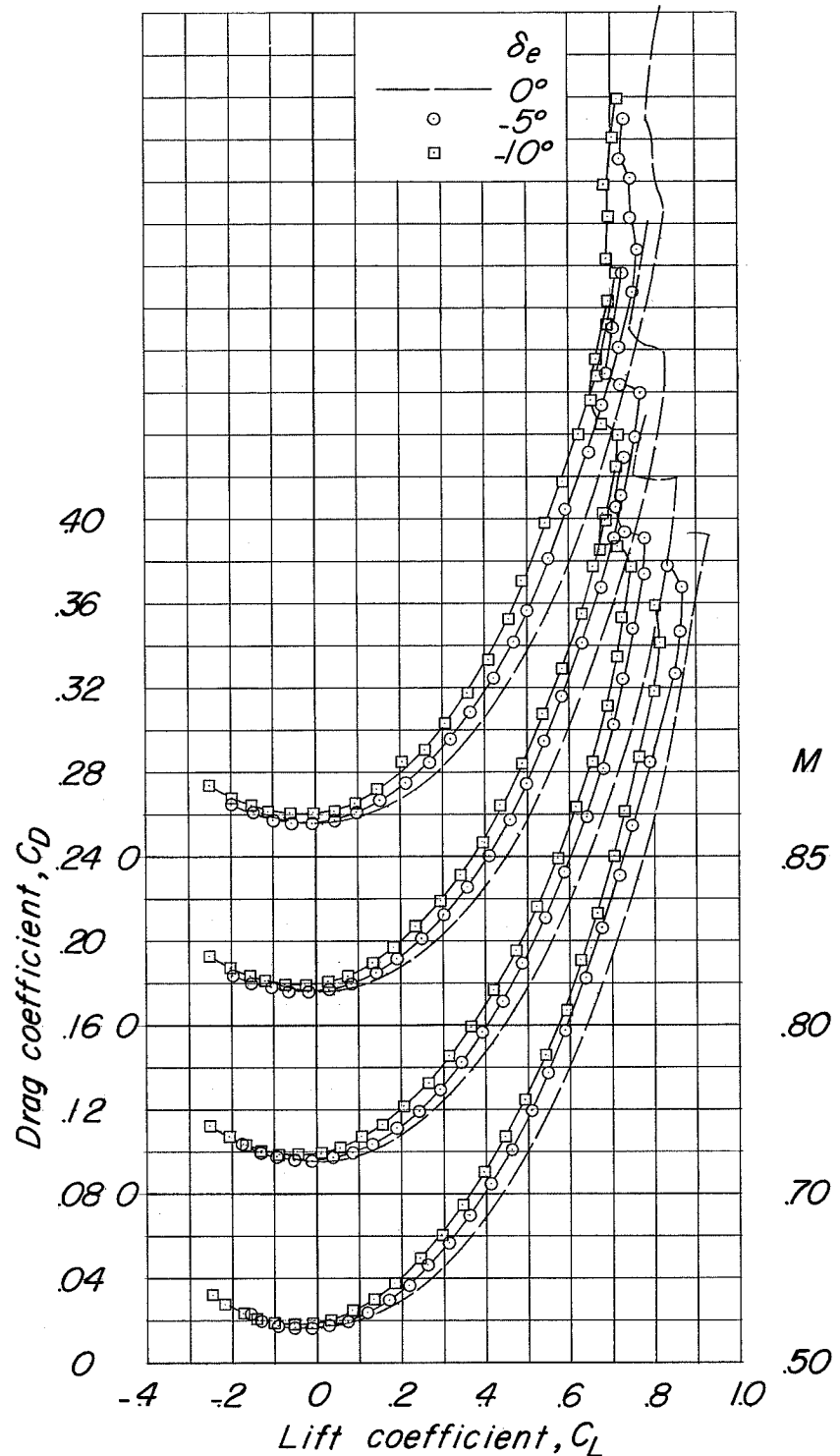
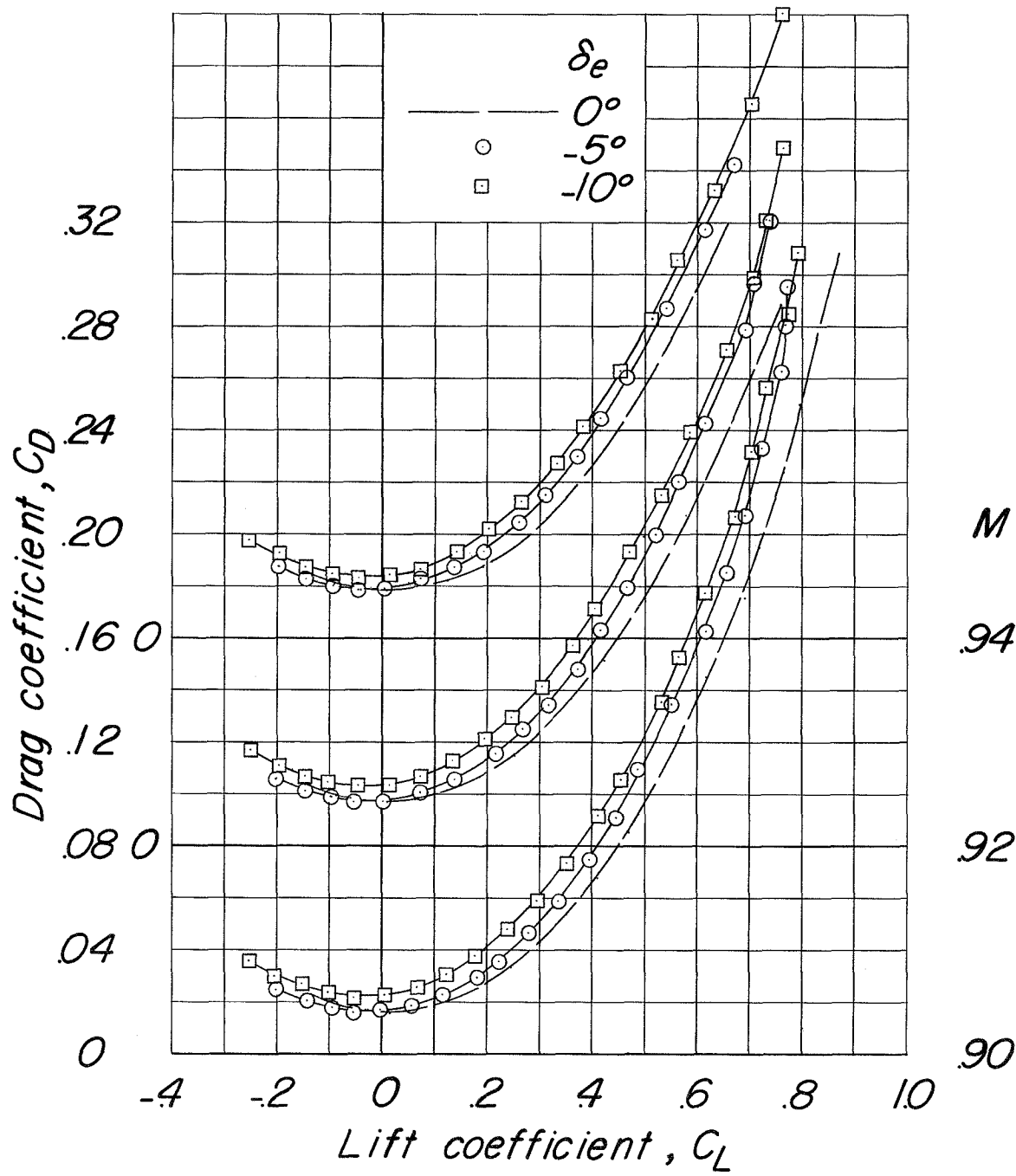
(c) C_D against C_L .

Figure 9.- Continued.



(c) Concluded.

Figure 9.- Continued.

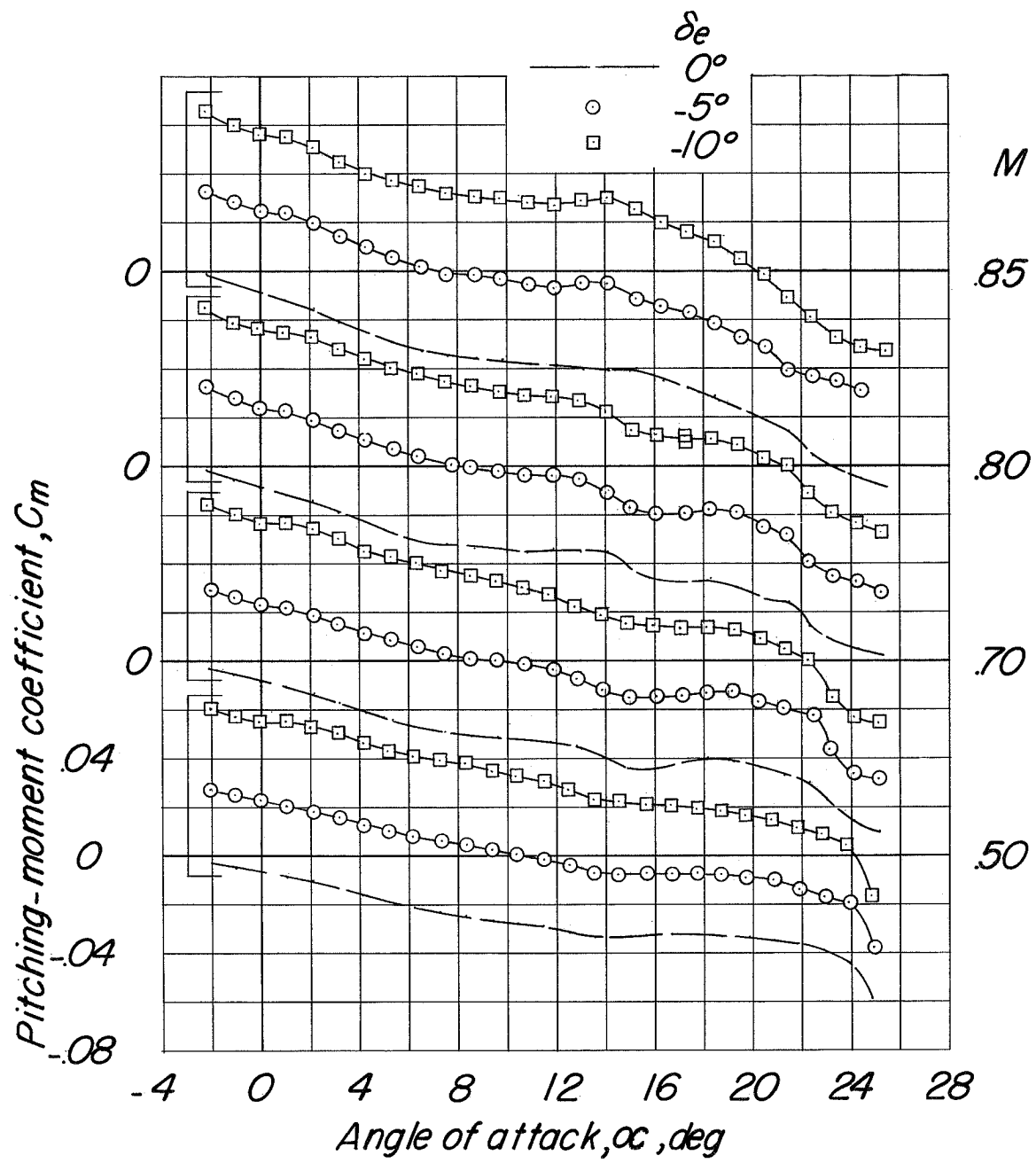
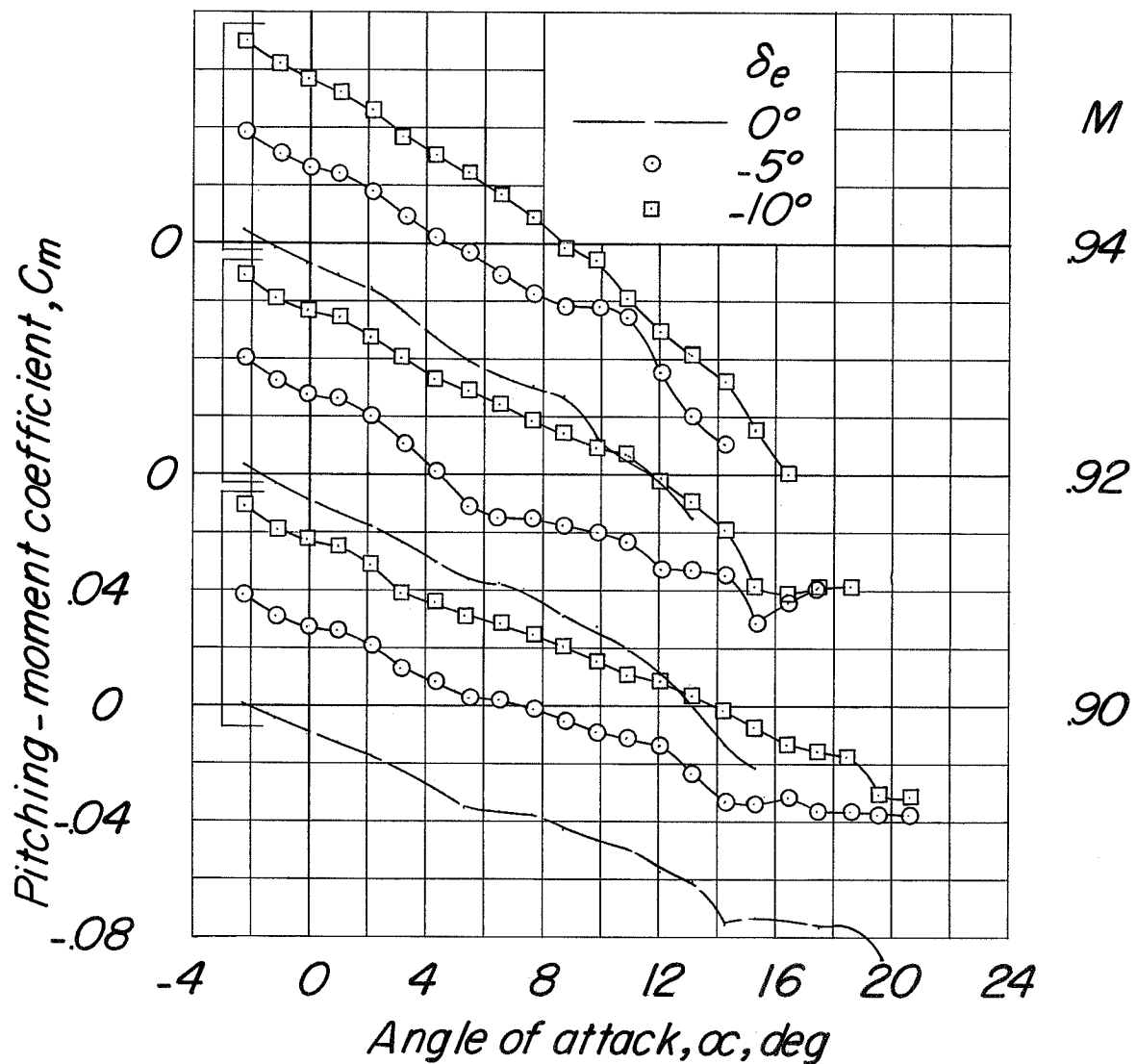
(d) C_m against α .

Figure 9.- Continued.



(d) Concluded.

Figure 9.- Continued.

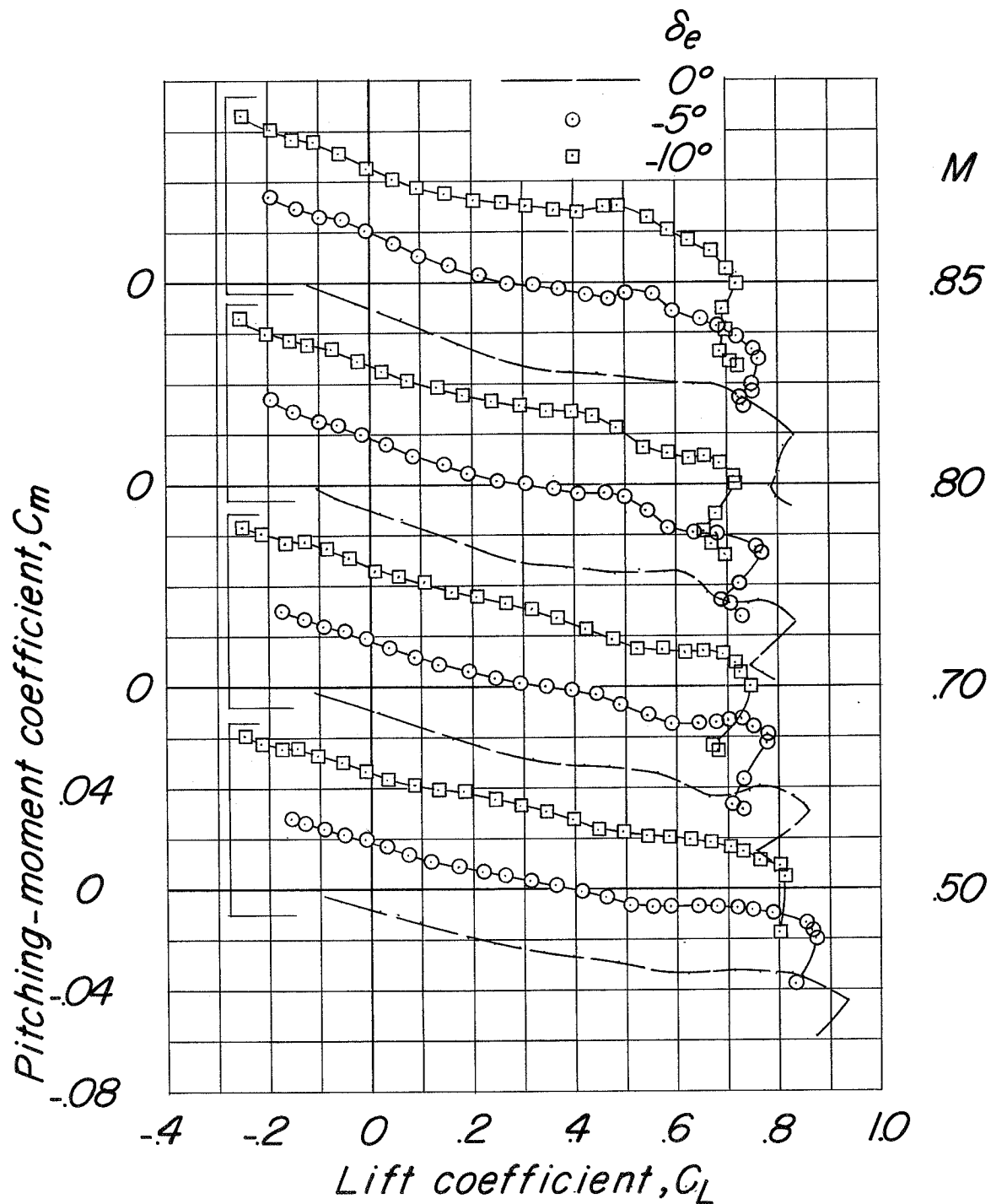
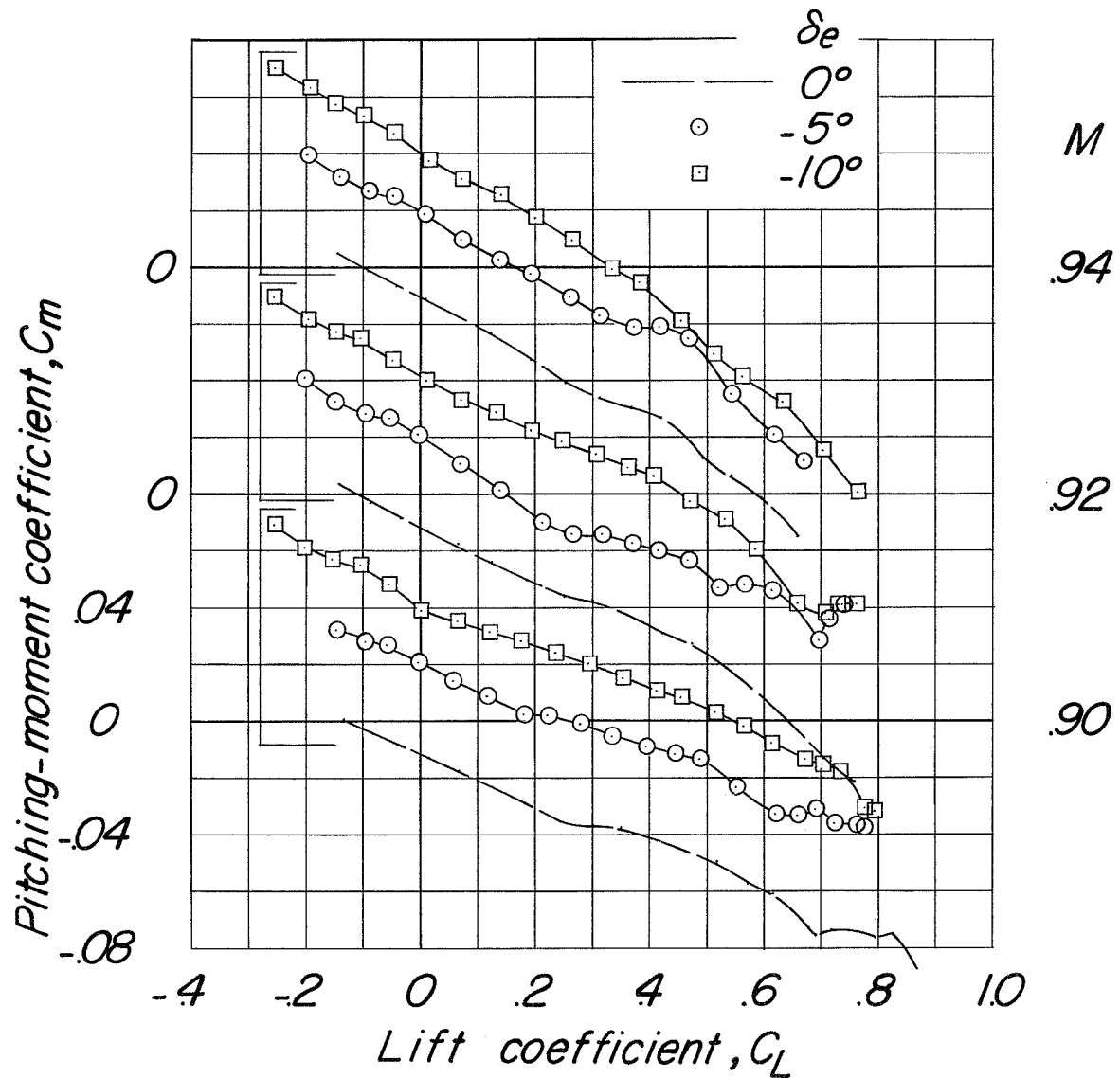
(e) C_m against C_L .

Figure 9.- Continued.



(e) Concluded.

Figure 9.- Concluded.

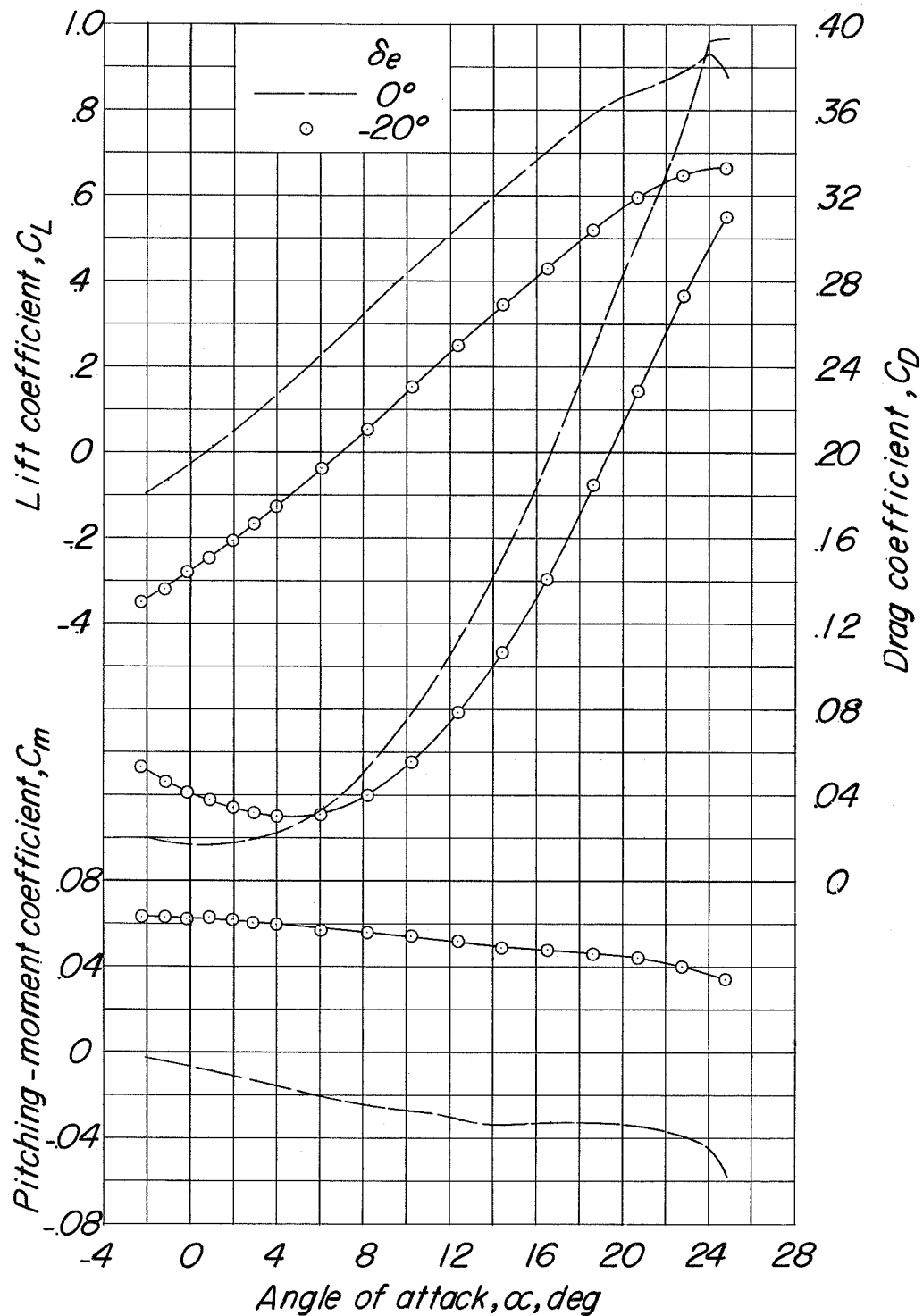


Figure 10.- Basic longitudinal characteristics for configuration BCWF₁V,
 $\delta_r = 0^\circ$, at a Mach number of 0.50.

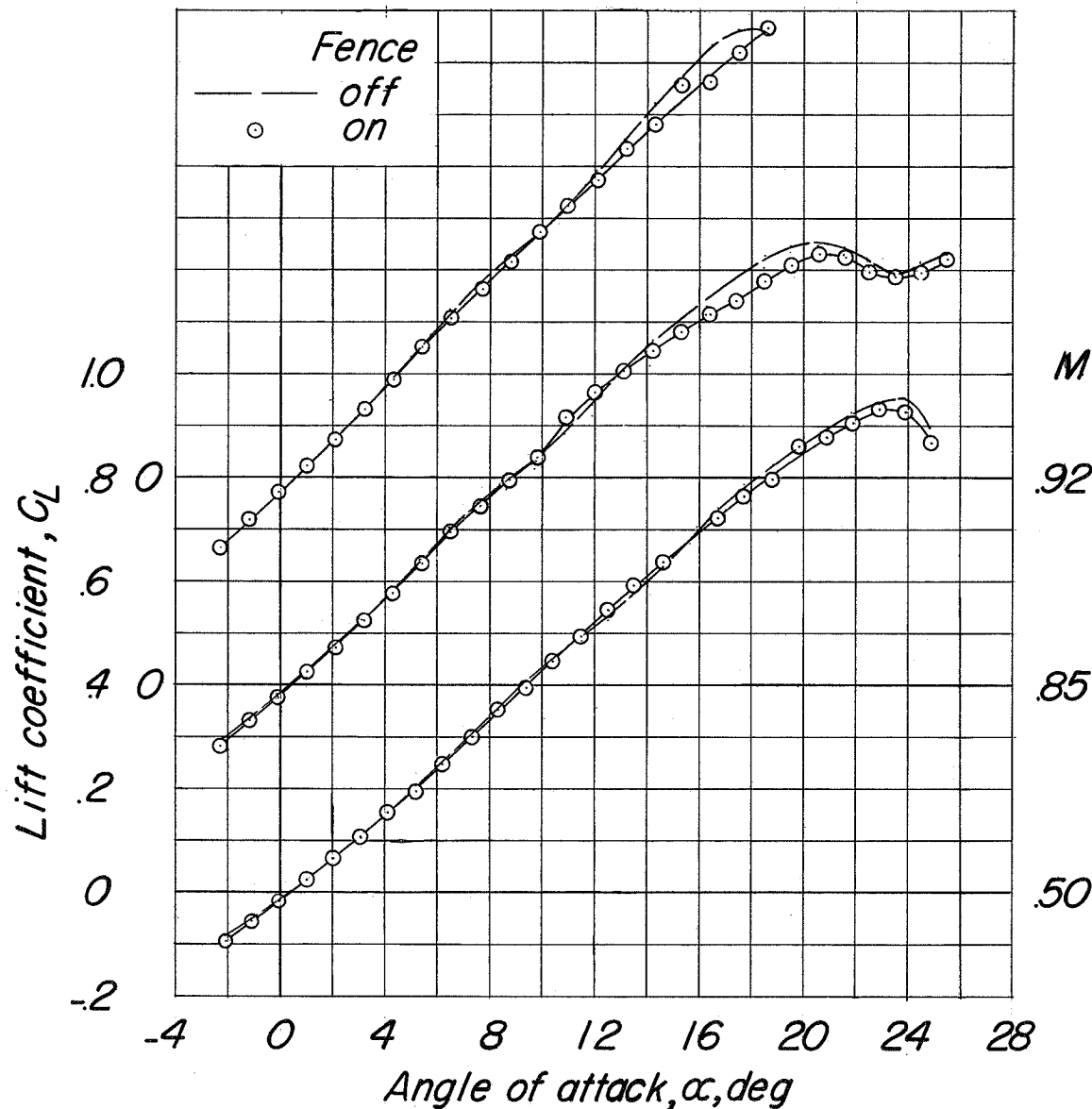
(a) C_L against α .

Figure 11.- Basic longitudinal characteristics for configuration BCWV, $\delta_e = 0^\circ$, $\delta_r = 0^\circ$, with and without fence 2.

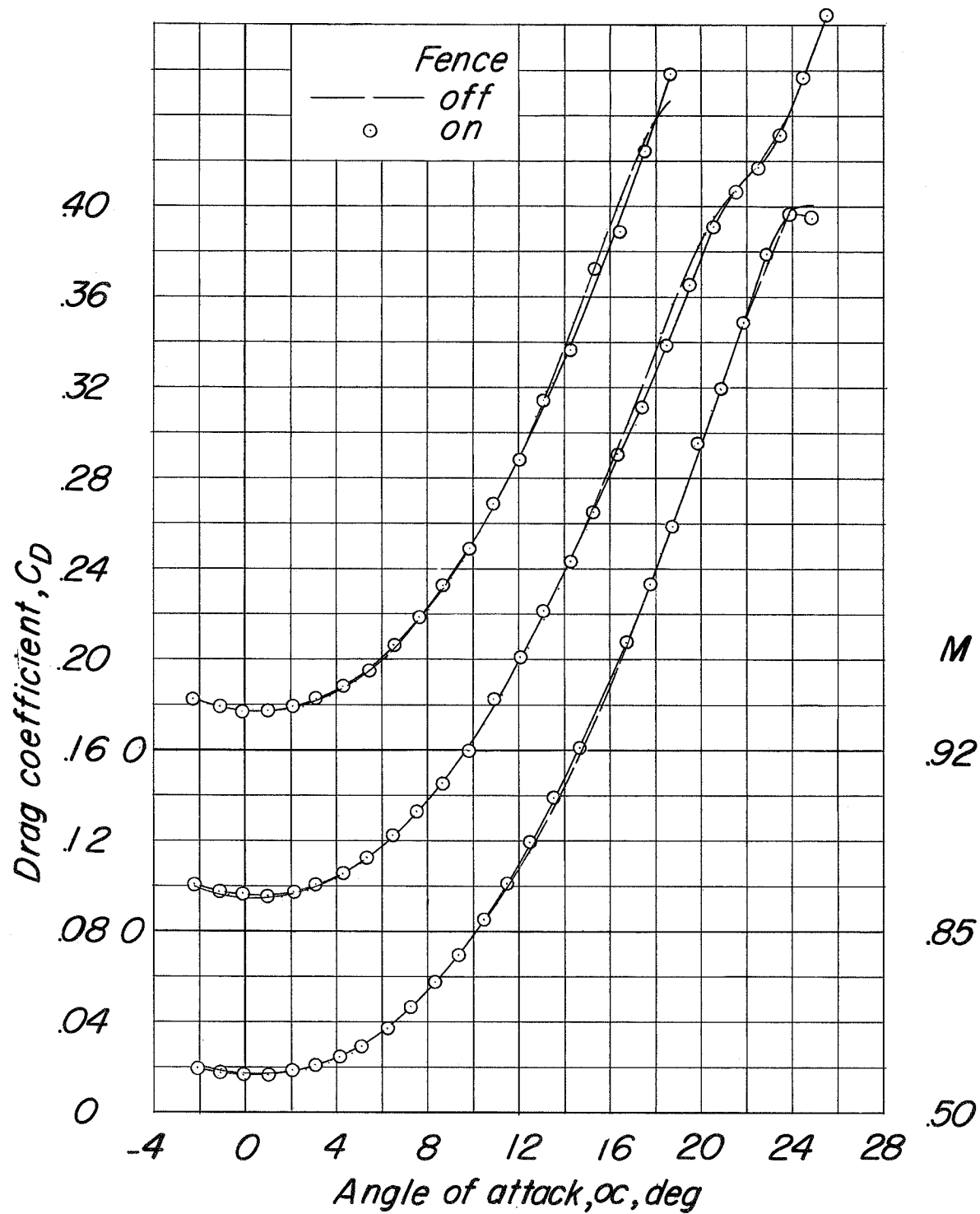
(b) C_D against α .

Figure 11.- Continued.

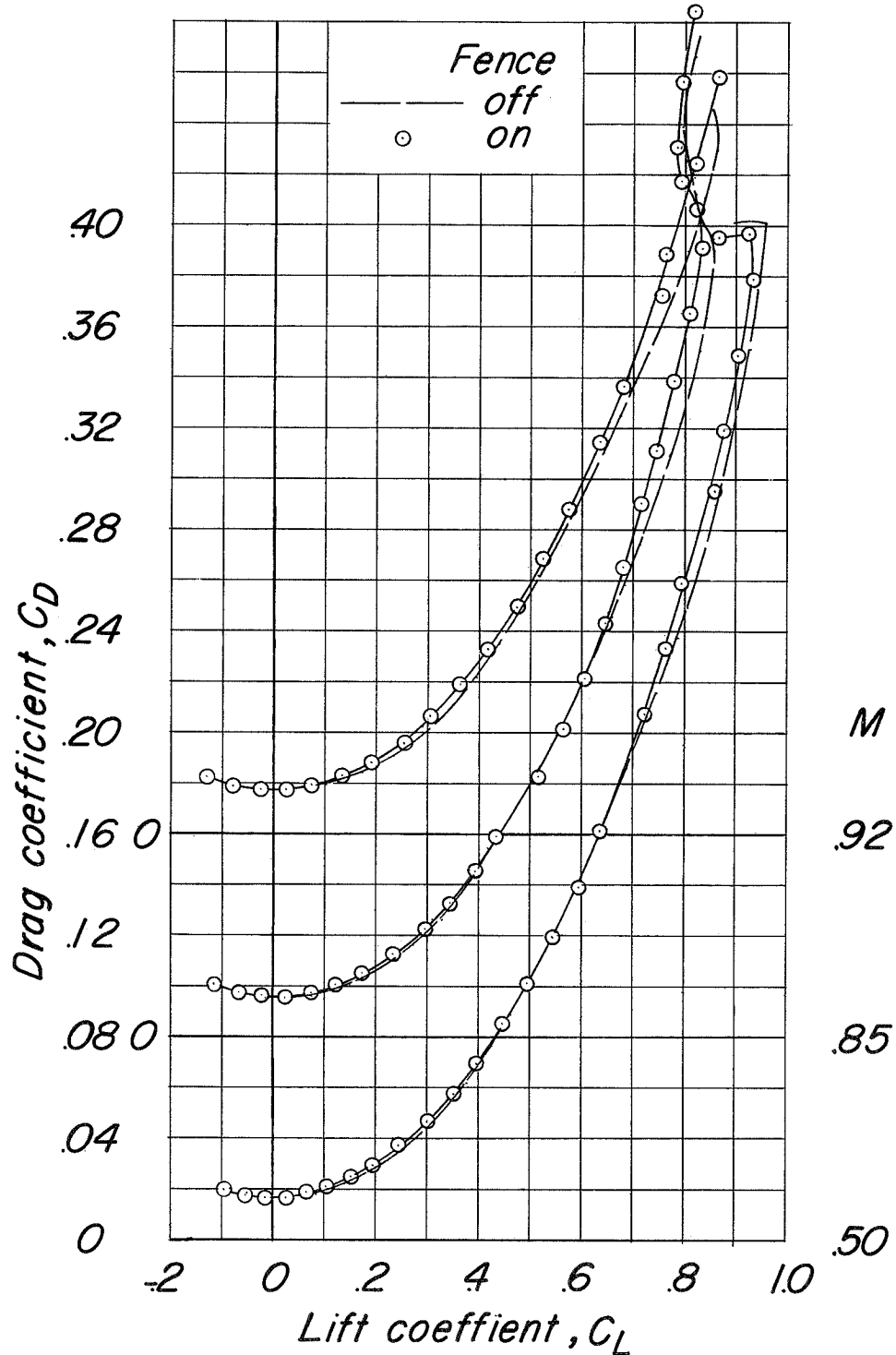
(c) C_D against C_L .

Figure 11.- Continued.

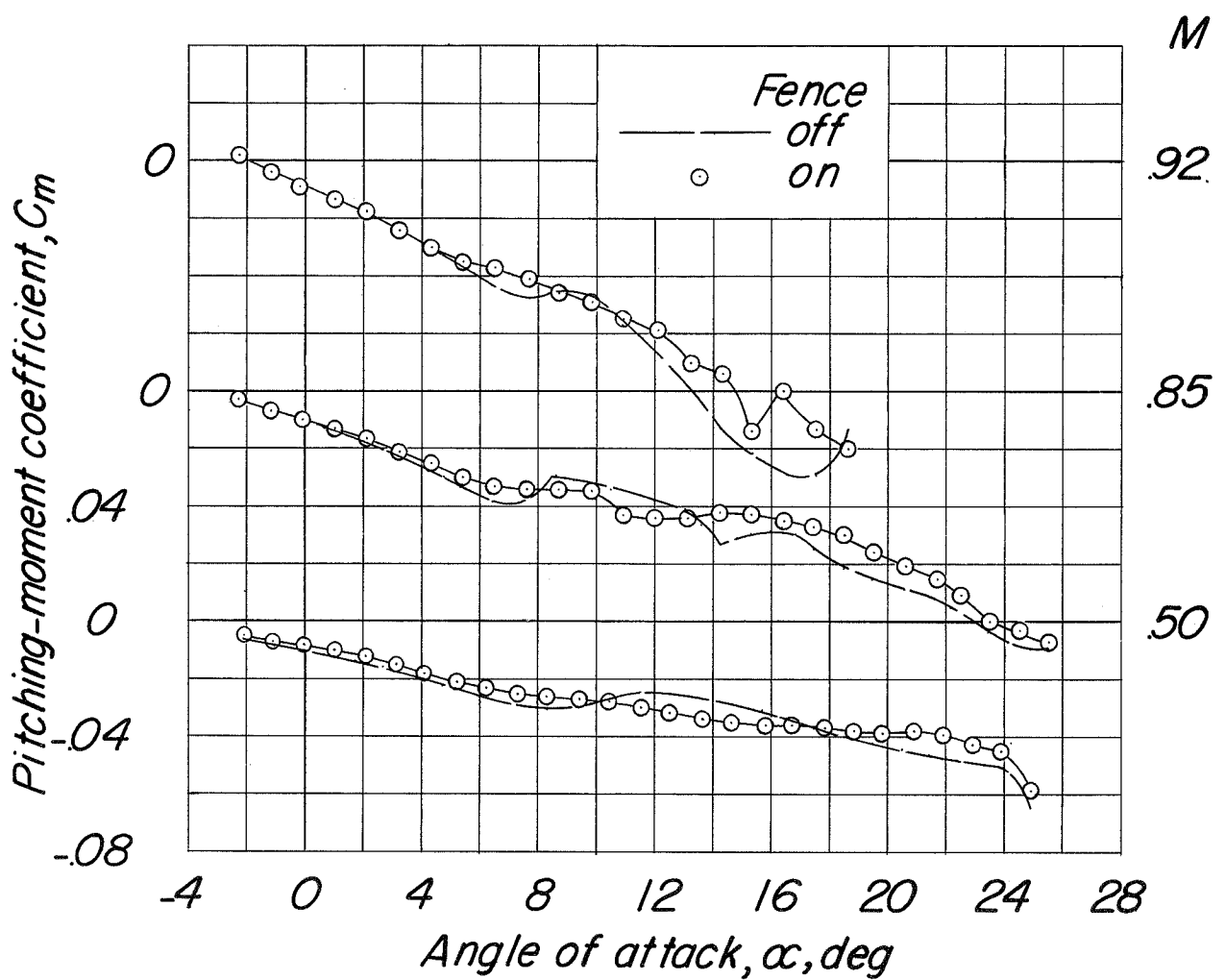
(d) C_m against α .

Figure 11.- Continued.

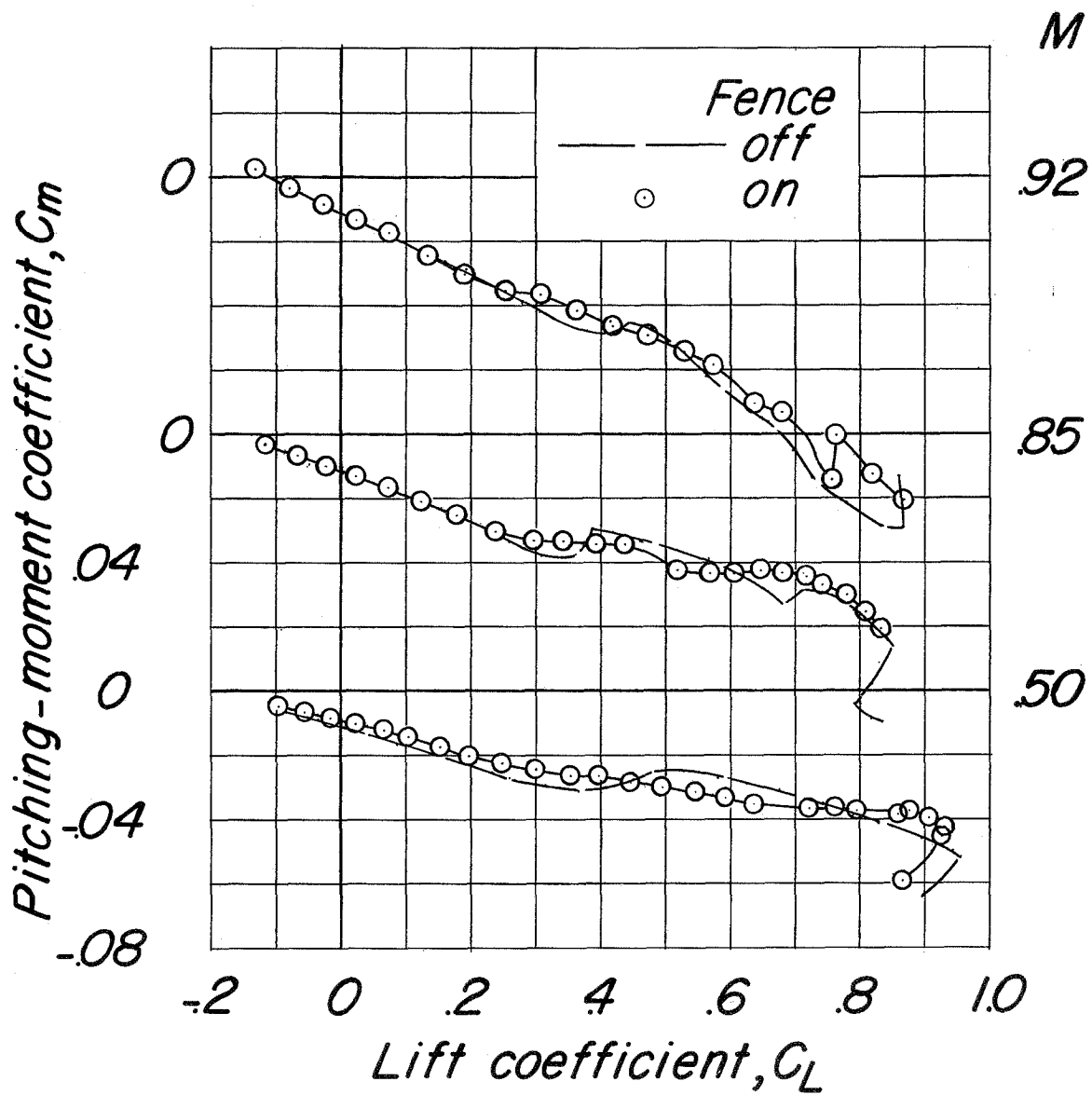
(e) C_m against C_L .

Figure 11.- Concluded.

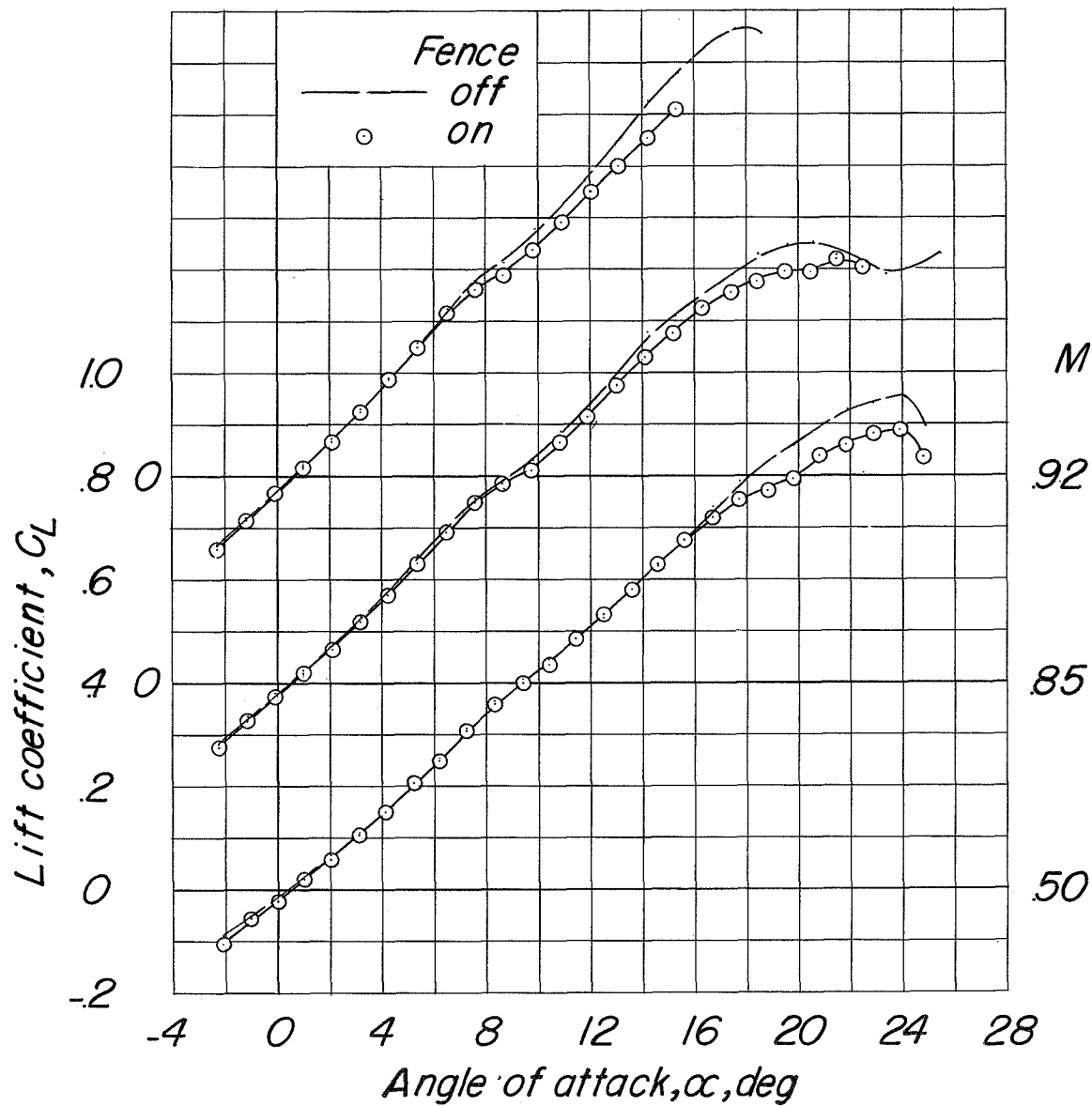
(a) C_L against α .

Figure 12.- Basic longitudinal characteristics for configuration BCWV, $\delta_e = 0^\circ$, $\delta_r = 0^\circ$, with and without fence 3.

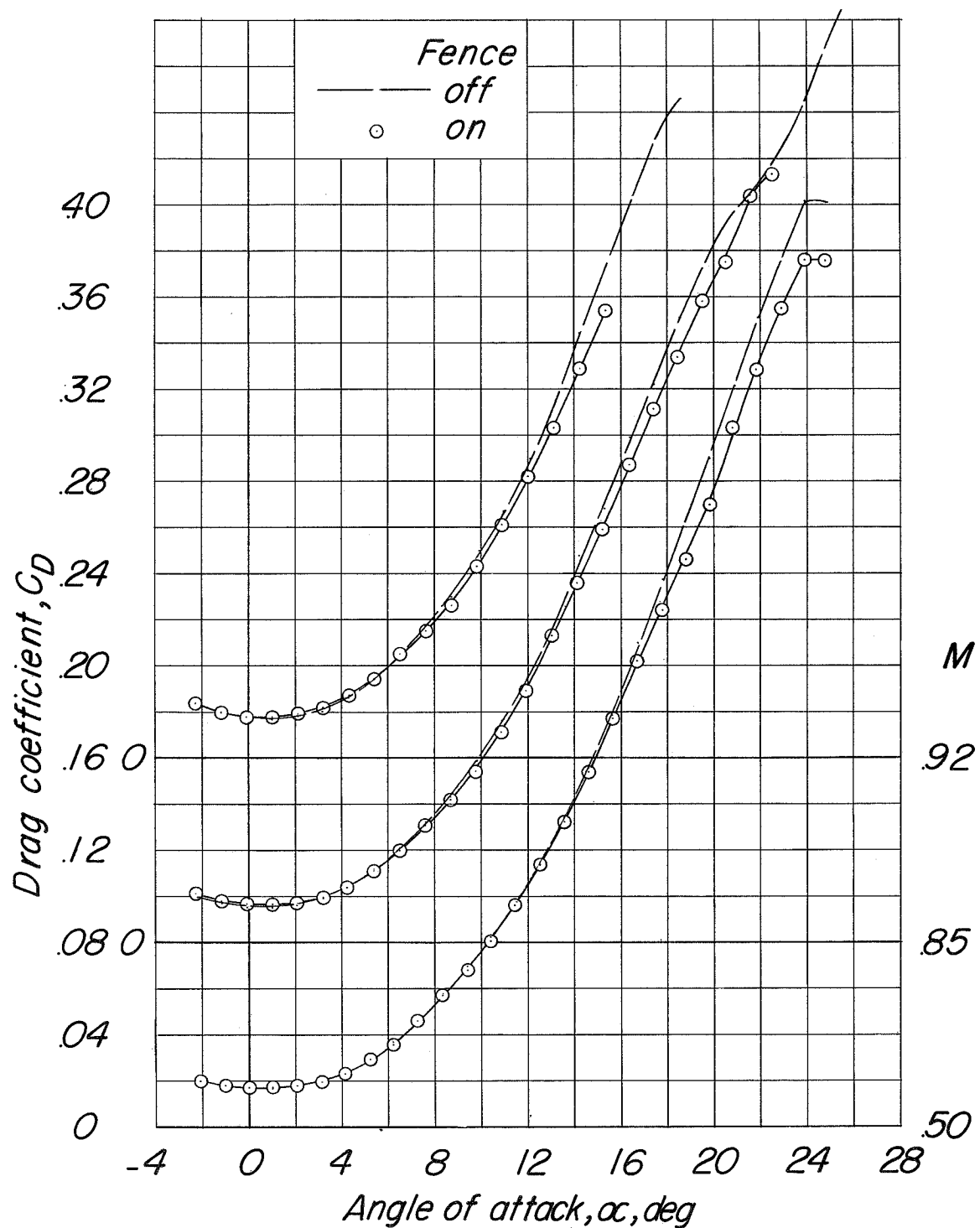
(b) C_D against α .

Figure 12.- Continued.

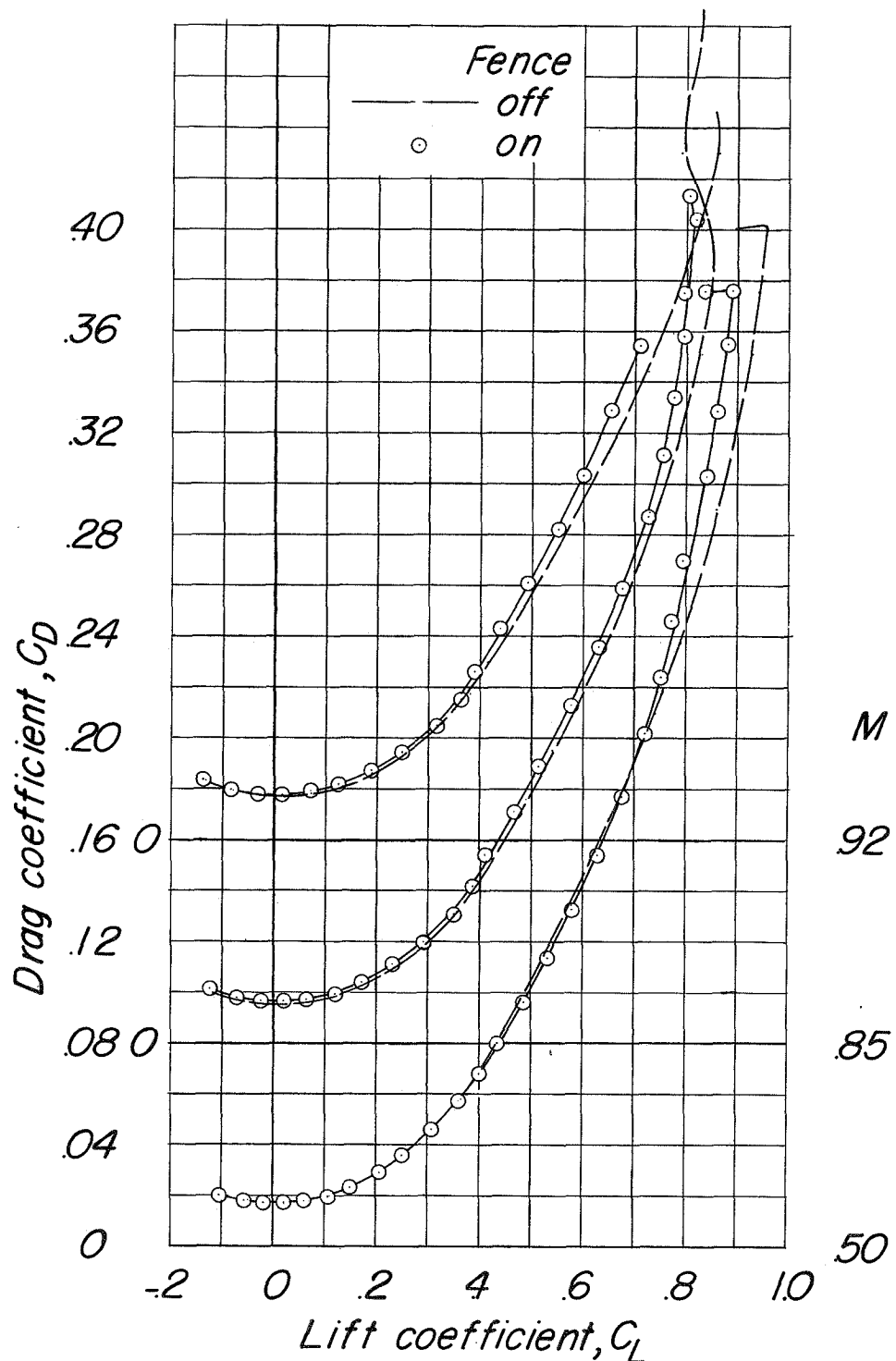
(c) C_D against C_L .

Figure 12.-- Continued.

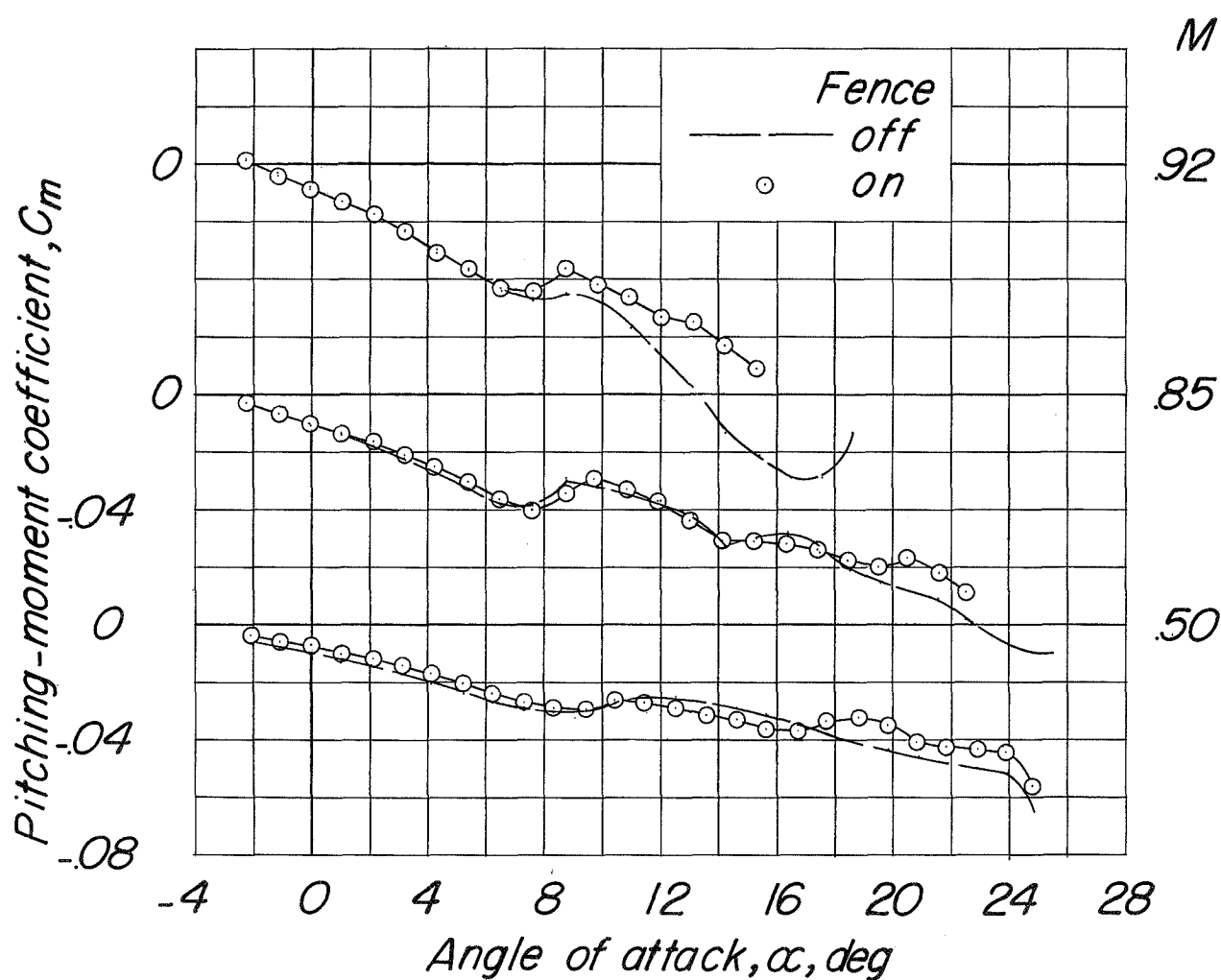
(d) C_m against α .

Figure 12.- Continued.

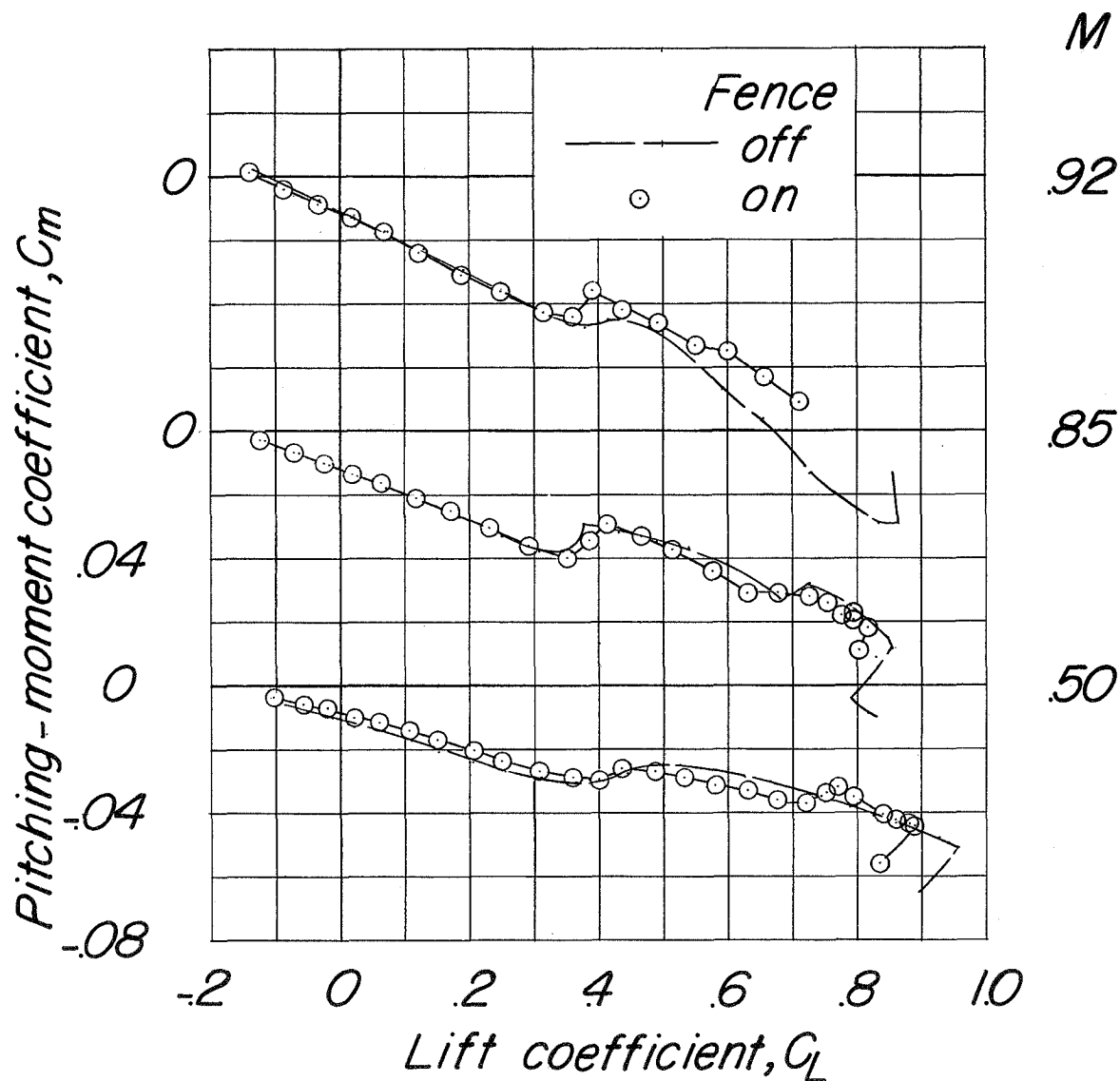
(e) C_m against C_L .

Figure 12.- Concluded.

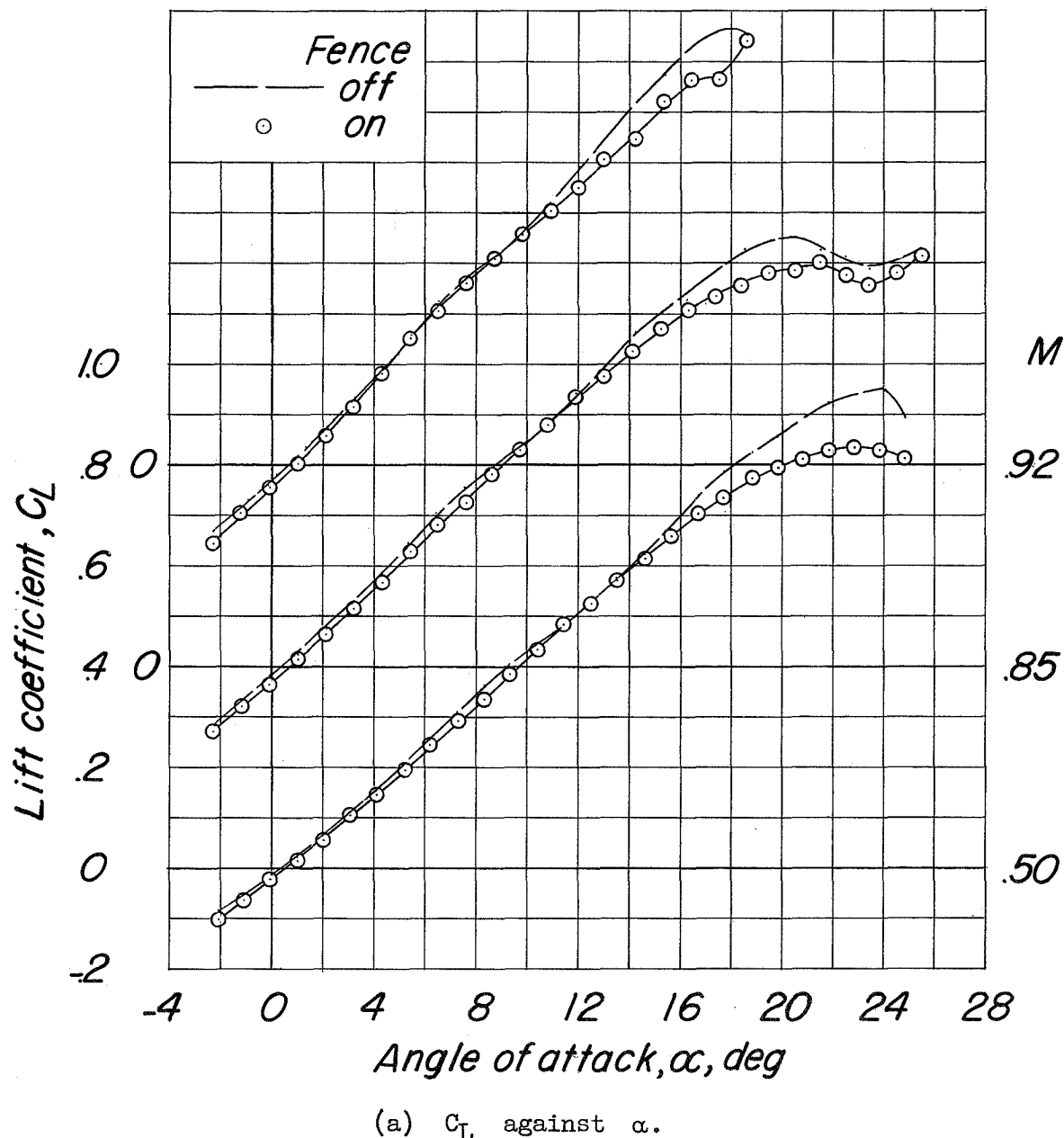


Figure 13.- Basic longitudinal characteristics for configuration BCWV,
 $\delta_e = 0^\circ$, $\delta_r = 0^\circ$, with and without fences 2 plus 3.

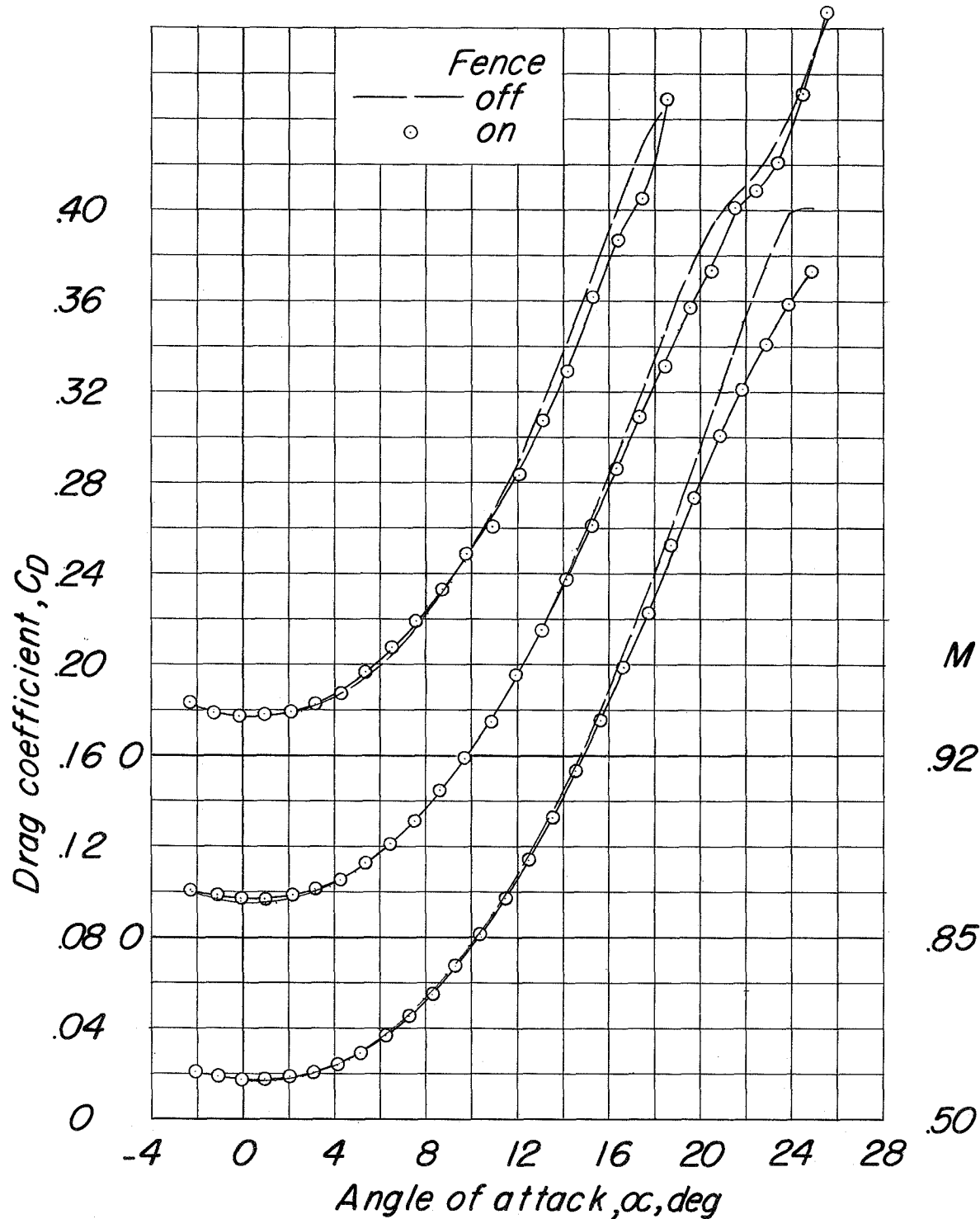
(b) C_D against α .

Figure 13.- Continued.

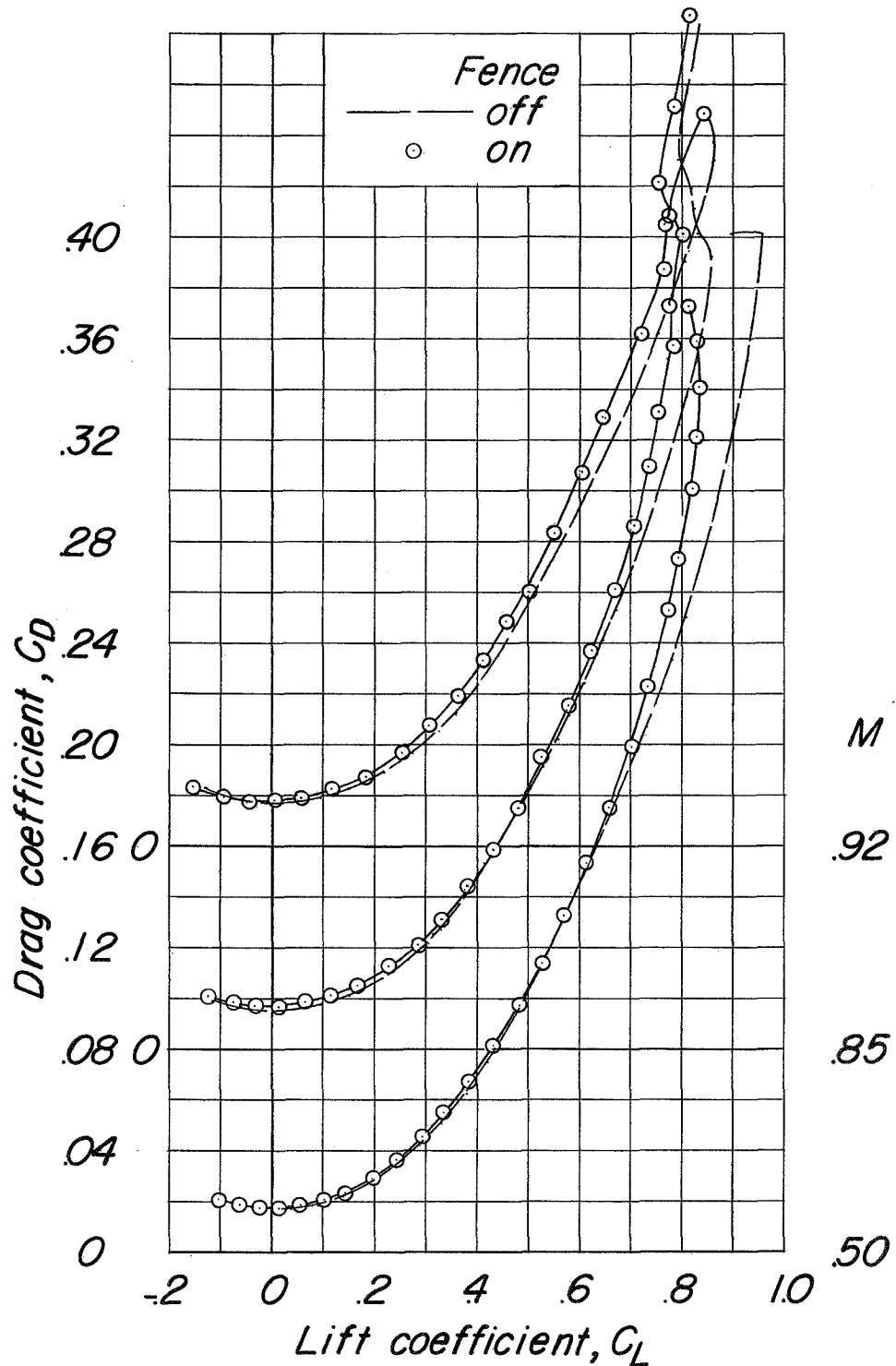
(c) C_D against C_L .

Figure 13.- Continued.

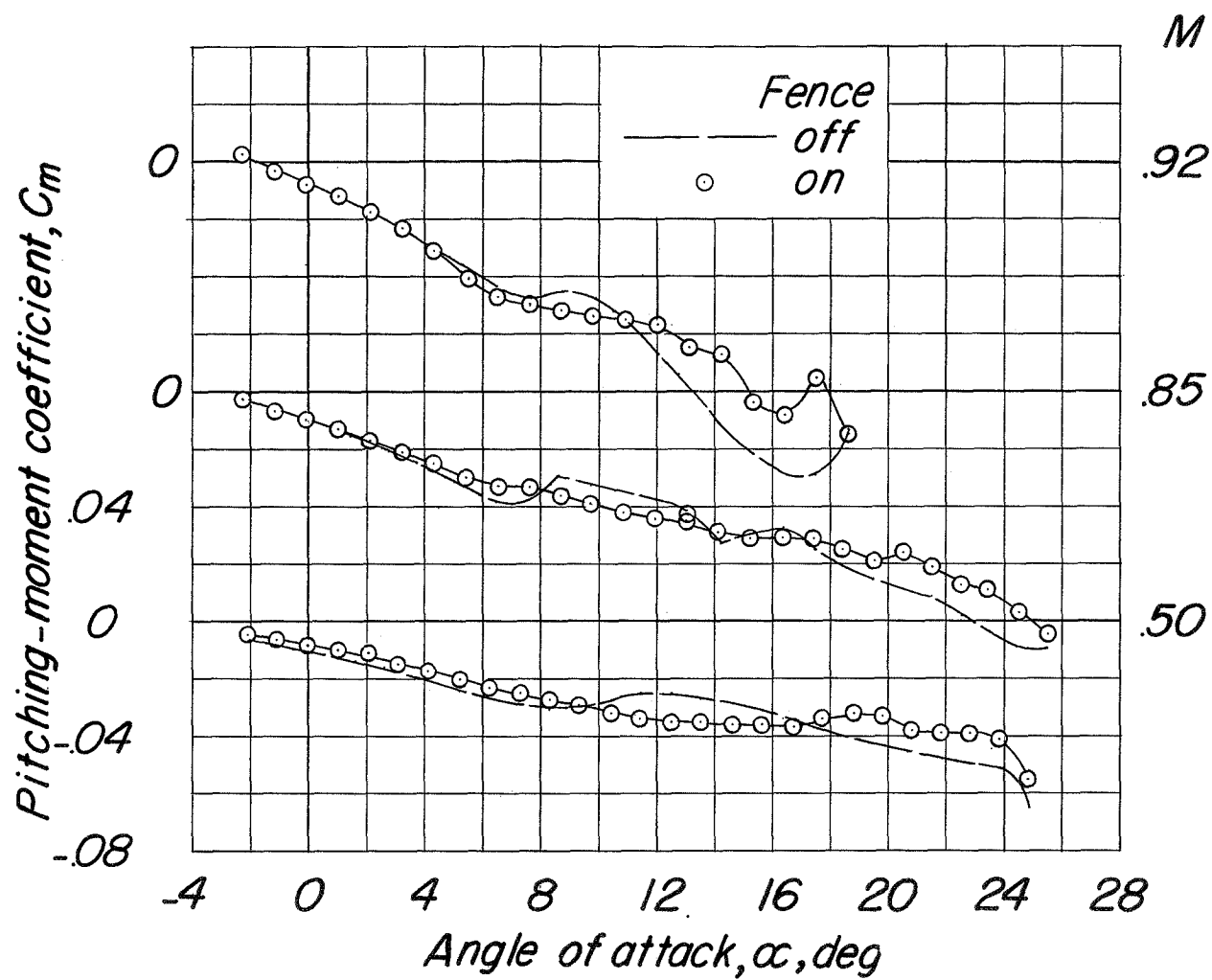
(d) C_m against α .

Figure 13.- Continued.

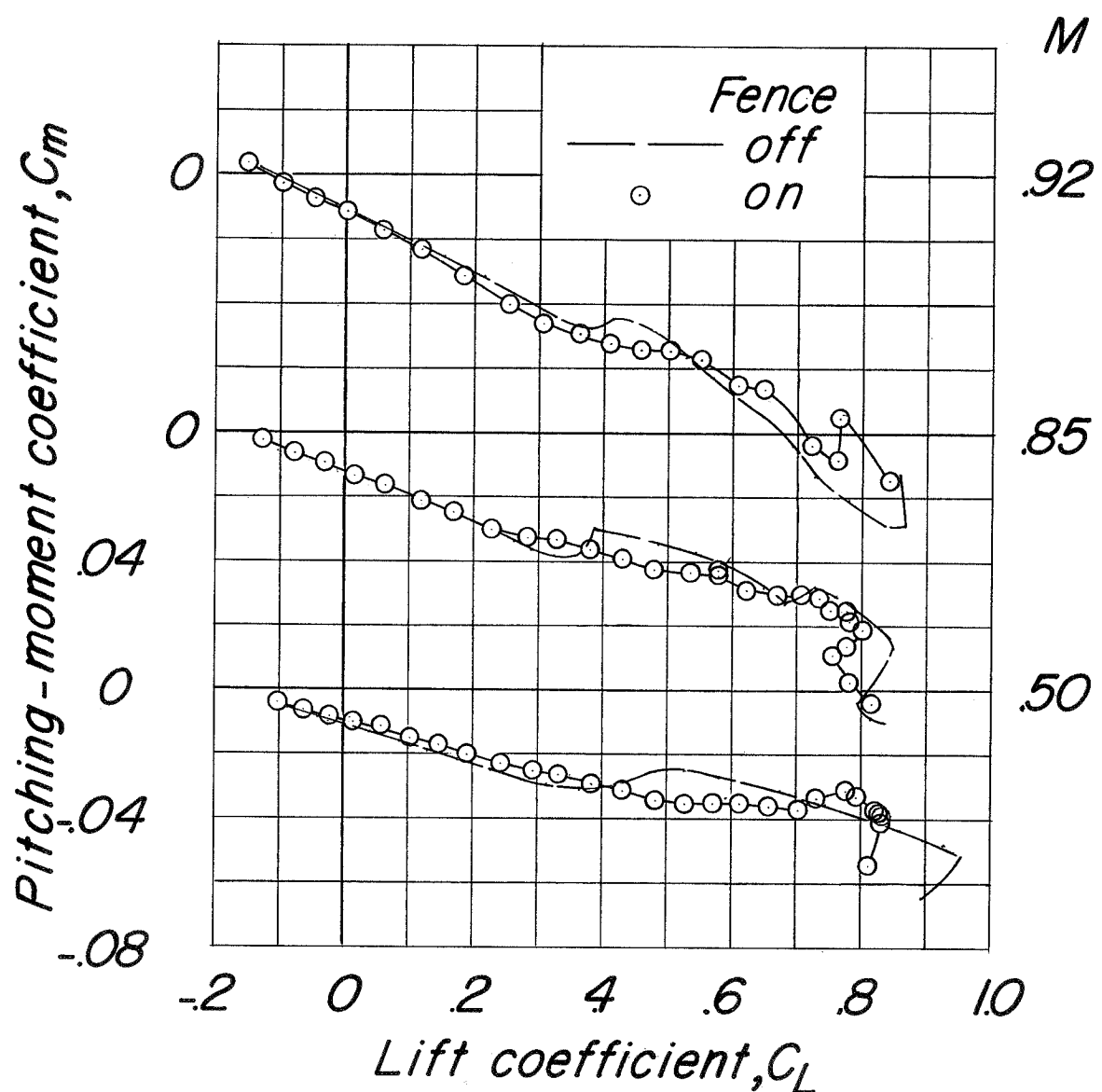
(e) C_m against C_L .

Figure 13.- Concluded.

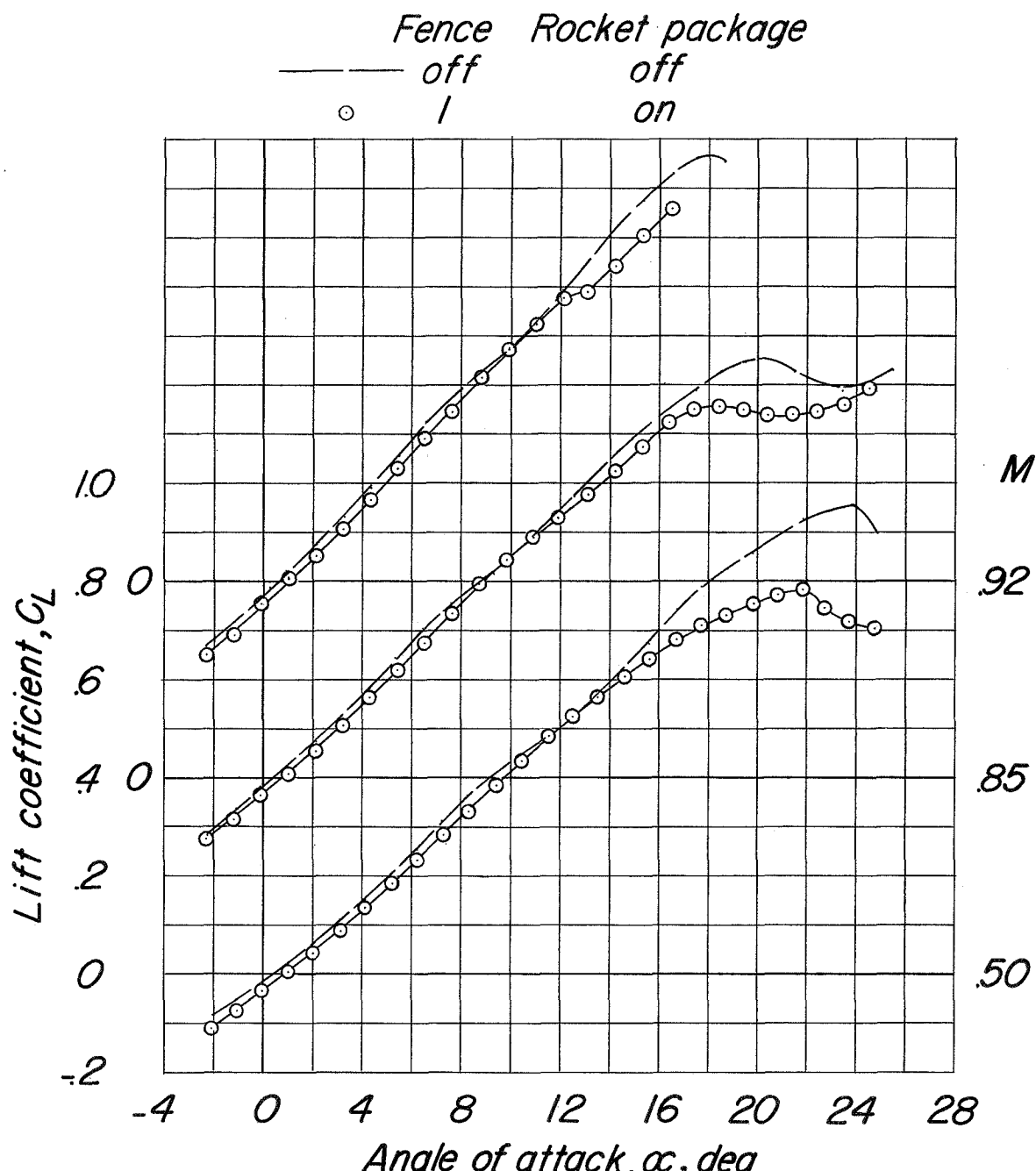
(a) C_L against α .

Figure 14.- Basic longitudinal characteristics for configuration BCWV, $\delta_e = 0^\circ$, $\delta_r = 0^\circ$, with and without fence 1 plus rocket package.

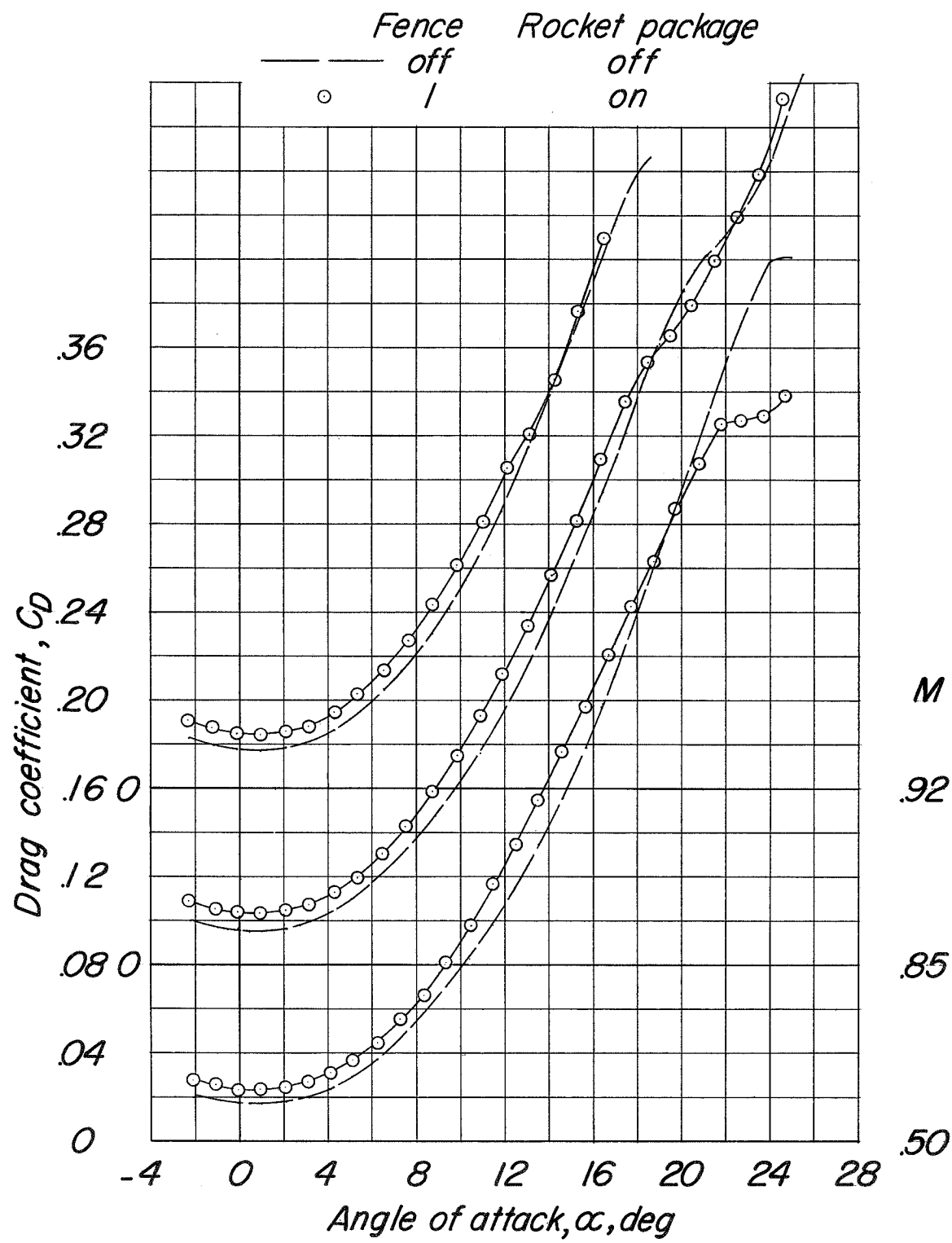
(b) C_D against α .

Figure 14.- Continued.

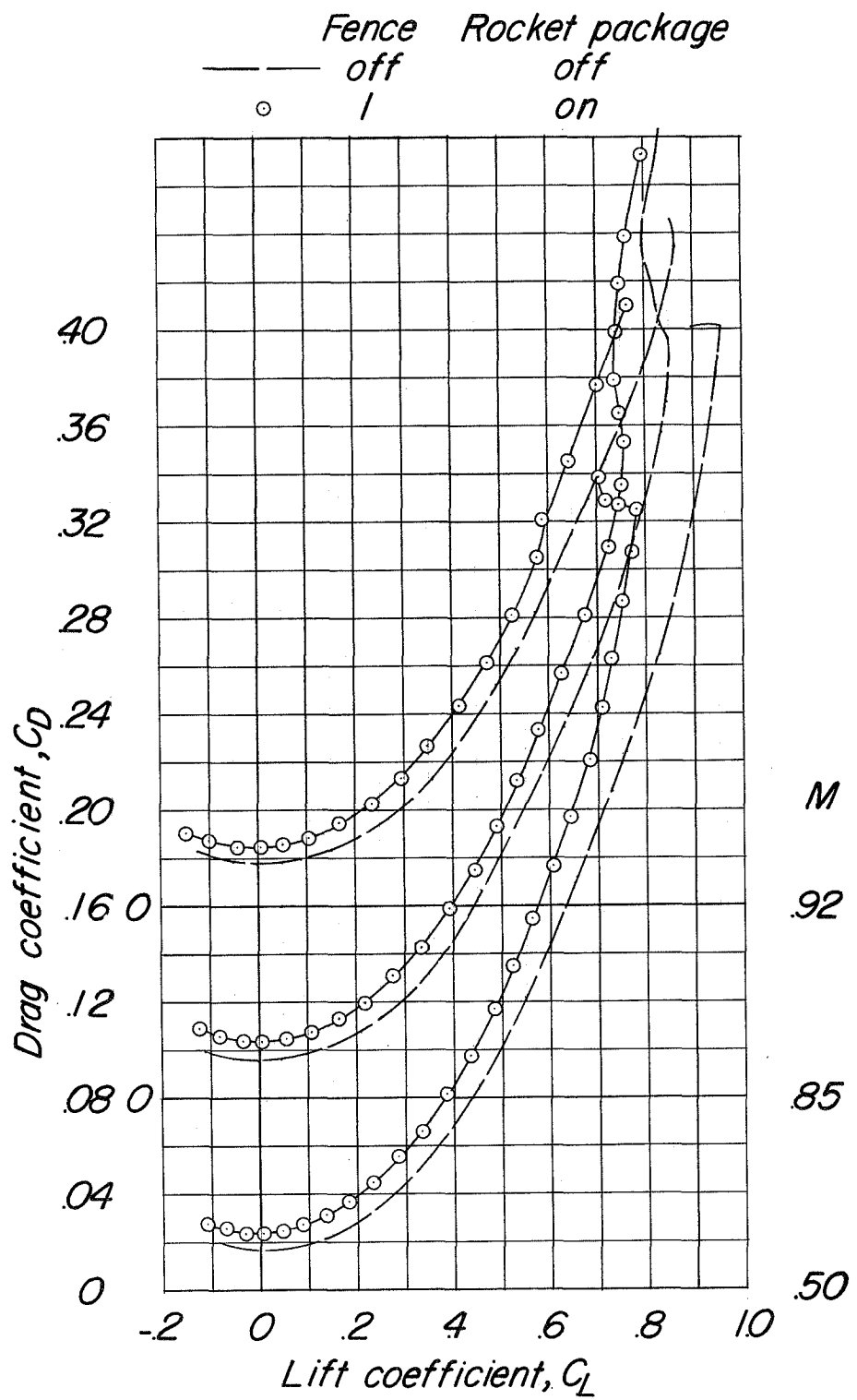
(c) C_D against C_L .

Figure 14.- Continued.

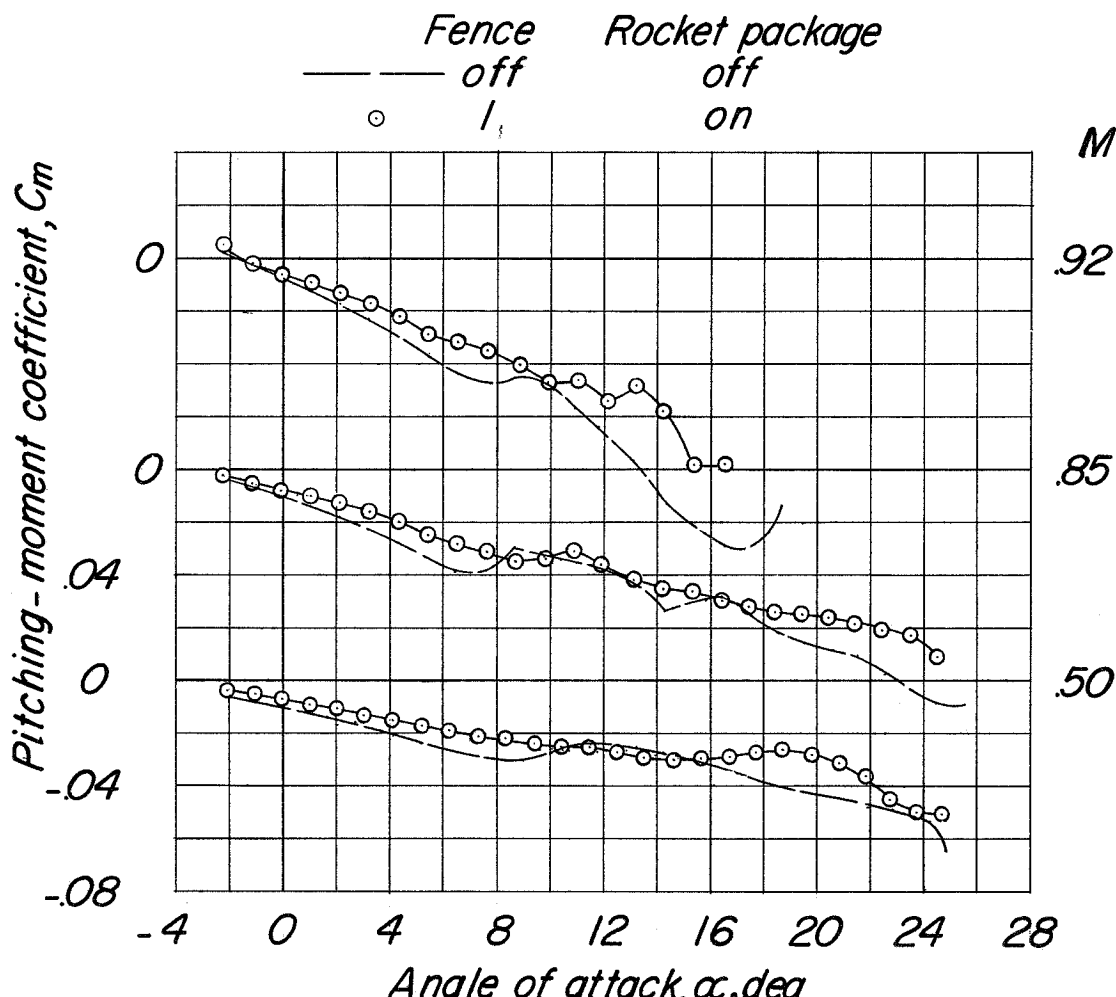


Figure 14.- Continued.

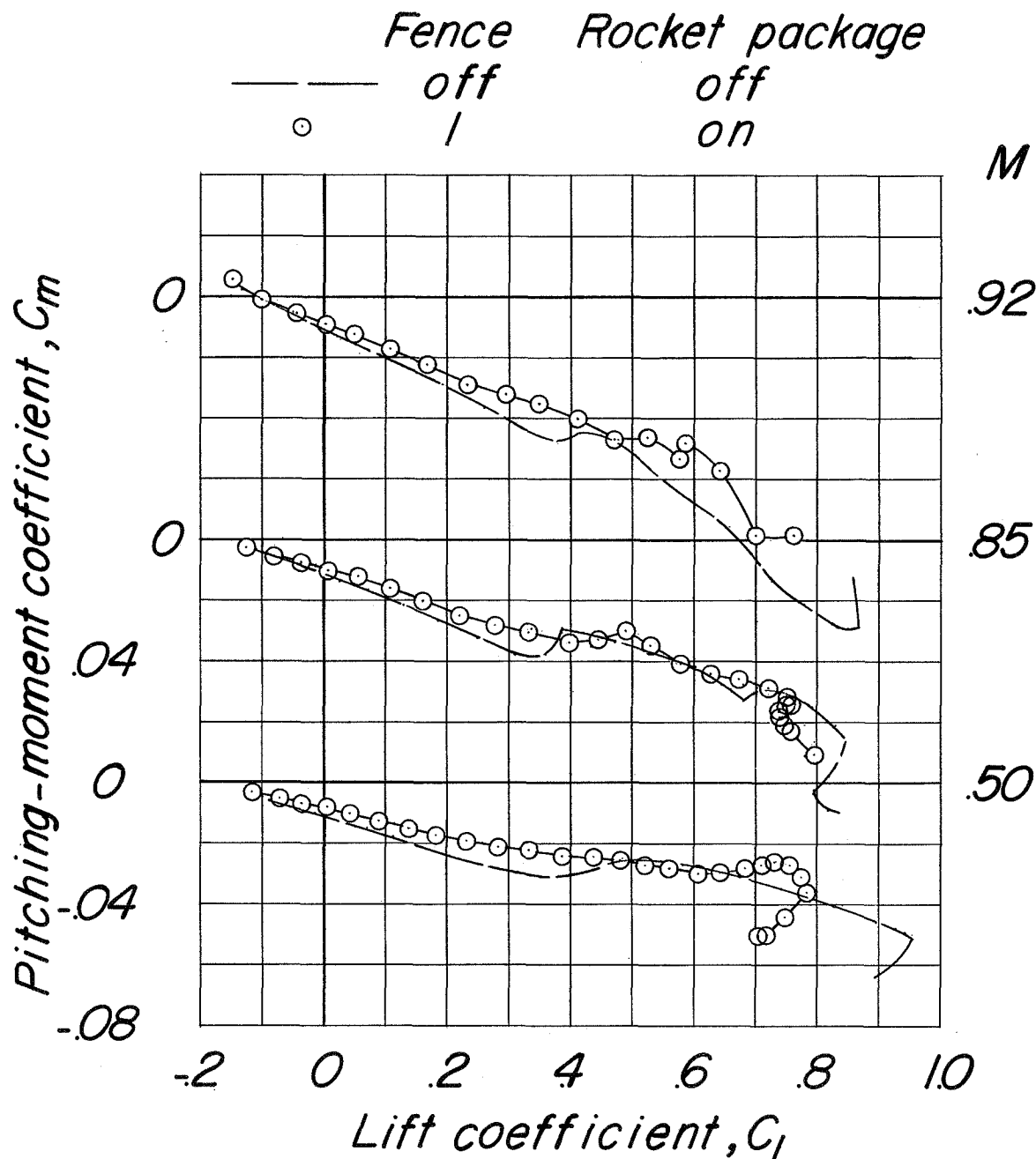
(e) C_m against C_L .

Figure 14.- Concluded.

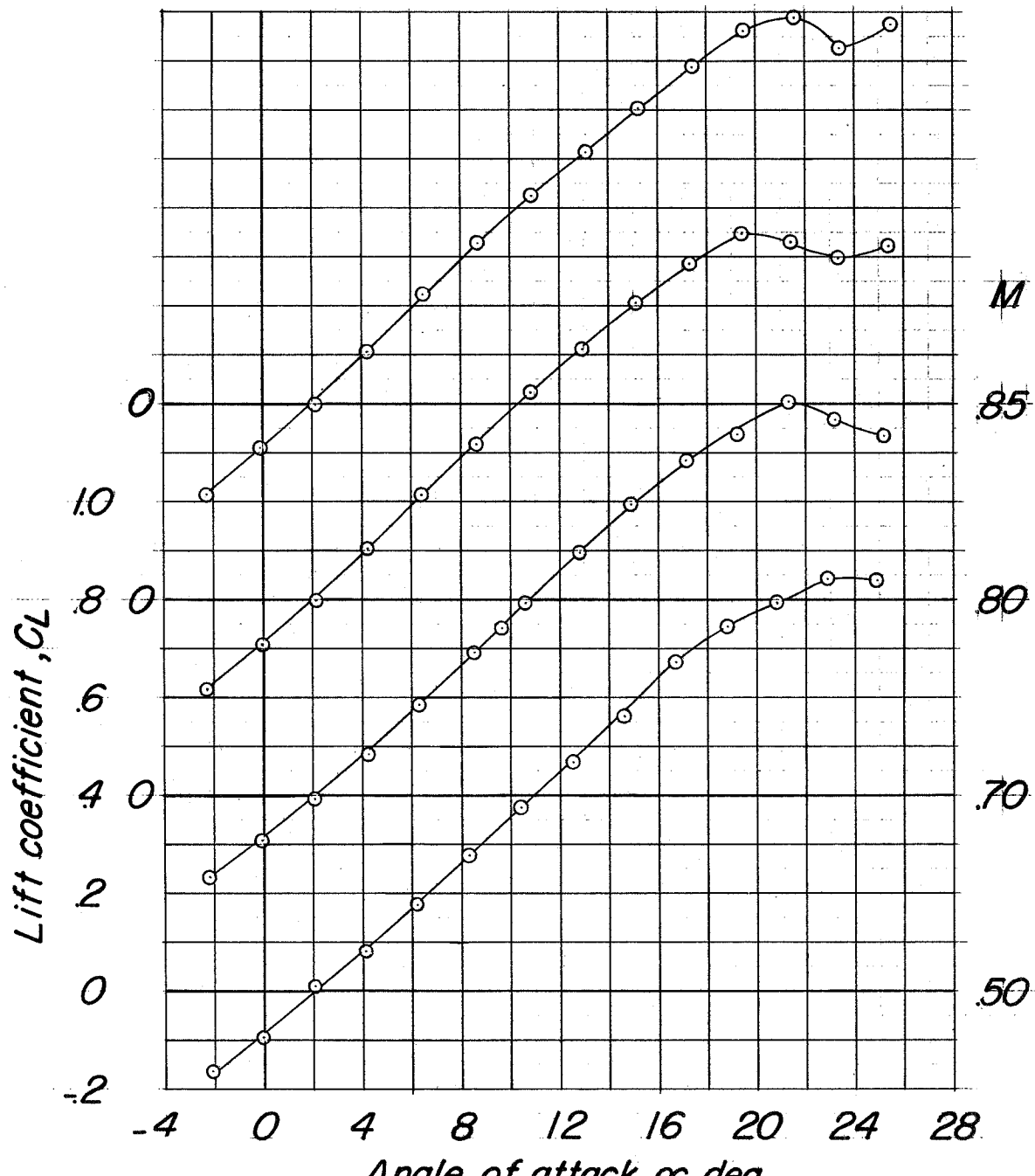
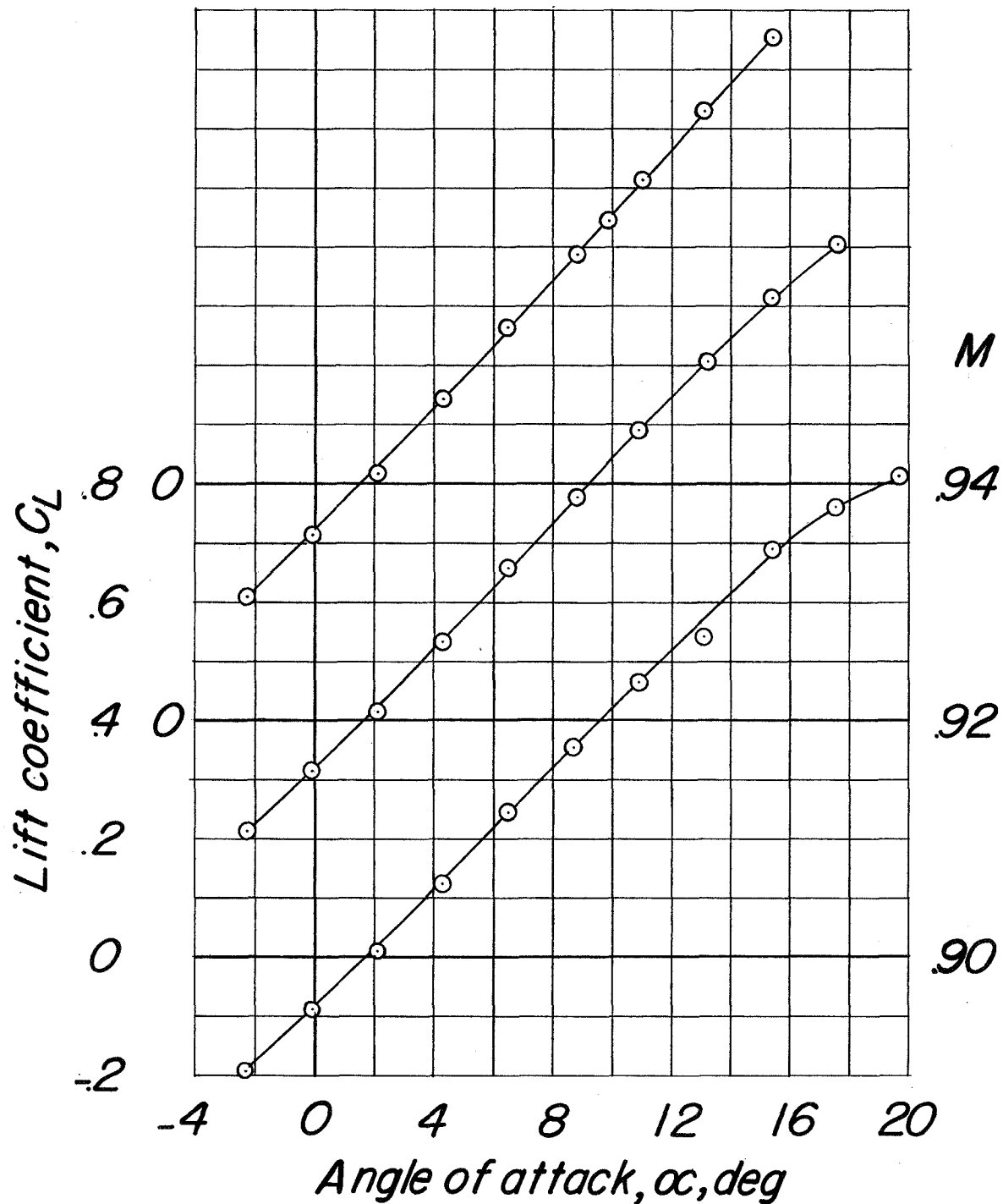
(a) C_L against α .

Figure 15.- Basic longitudinal characteristics for configuration BCWF₁V,
 $\delta_e = 0^\circ$ right and -10° left, $\delta_r = 0^\circ$.



(a) Concluded.

Figure 15.-- Continued.

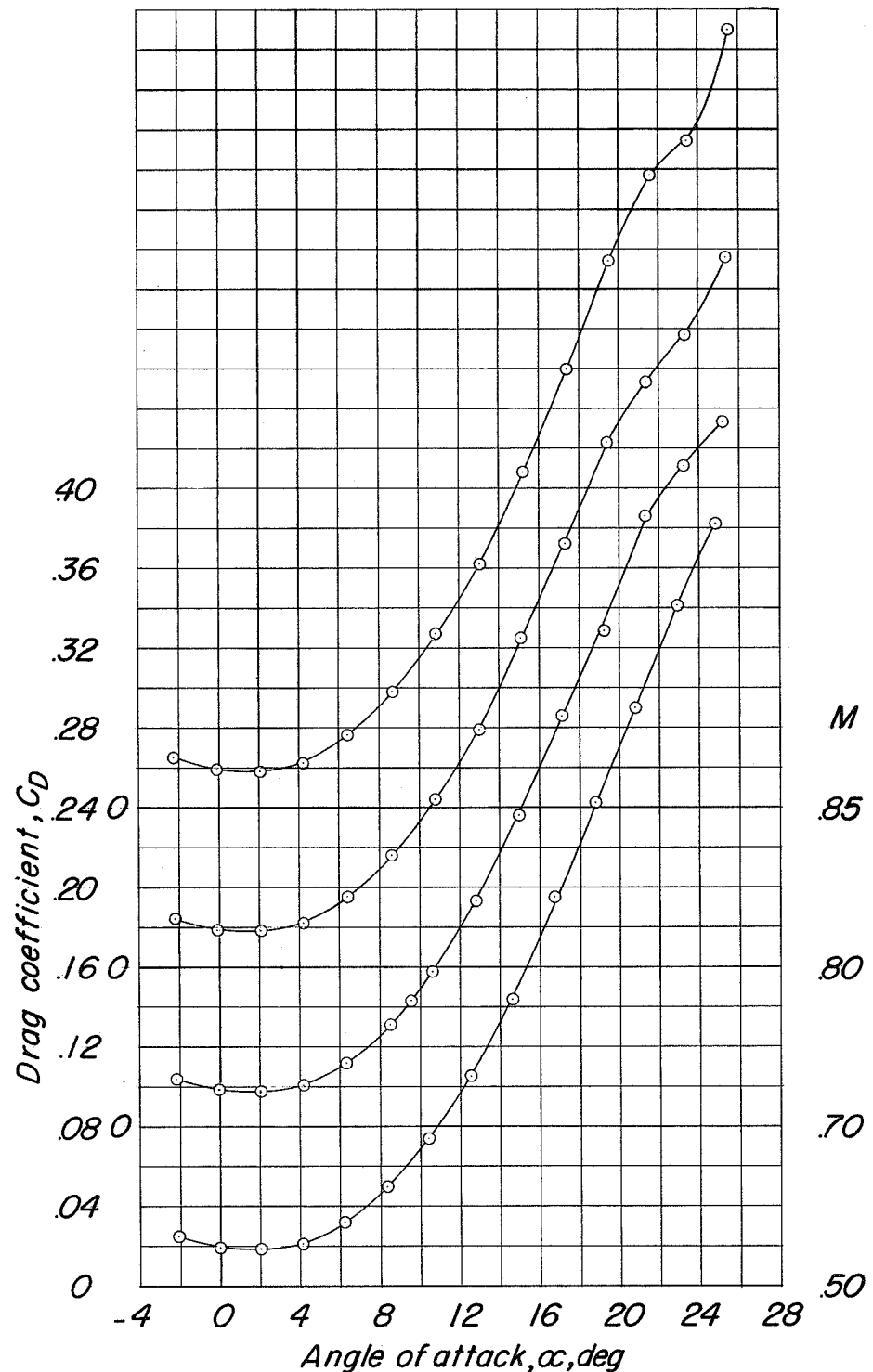
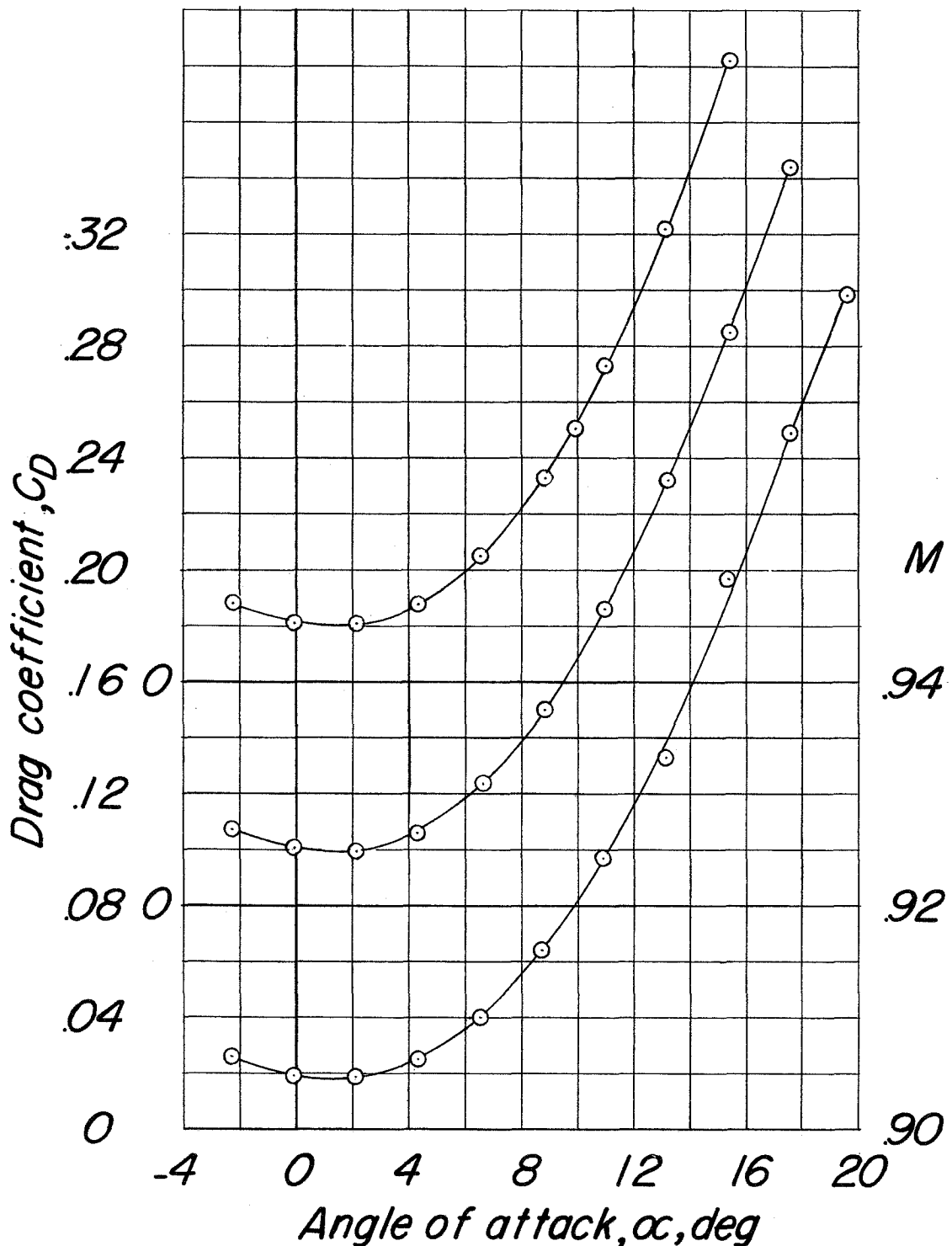
(b) C_D against α .

Figure 15.- Continued.



(b) Concluded.

Figure 15.- Continued.

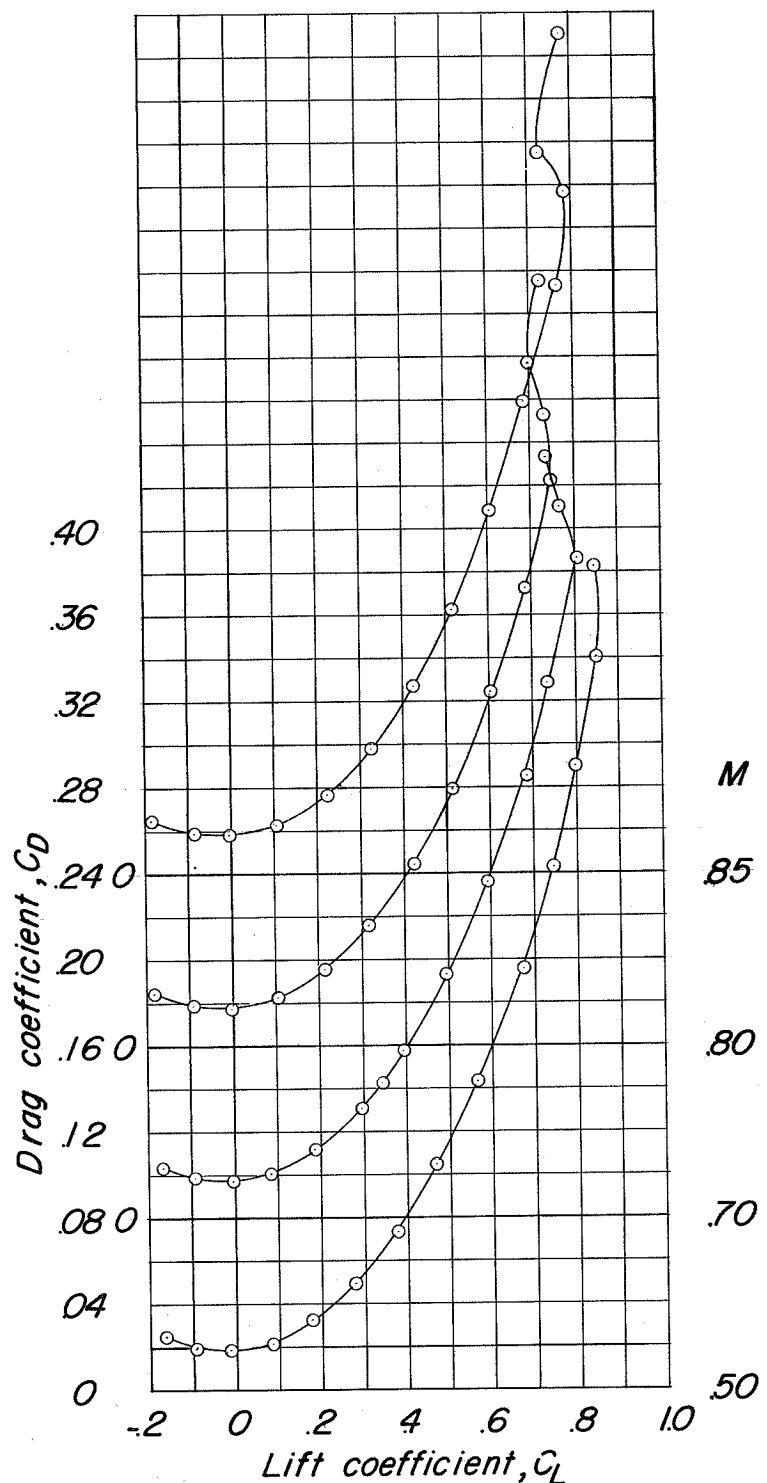
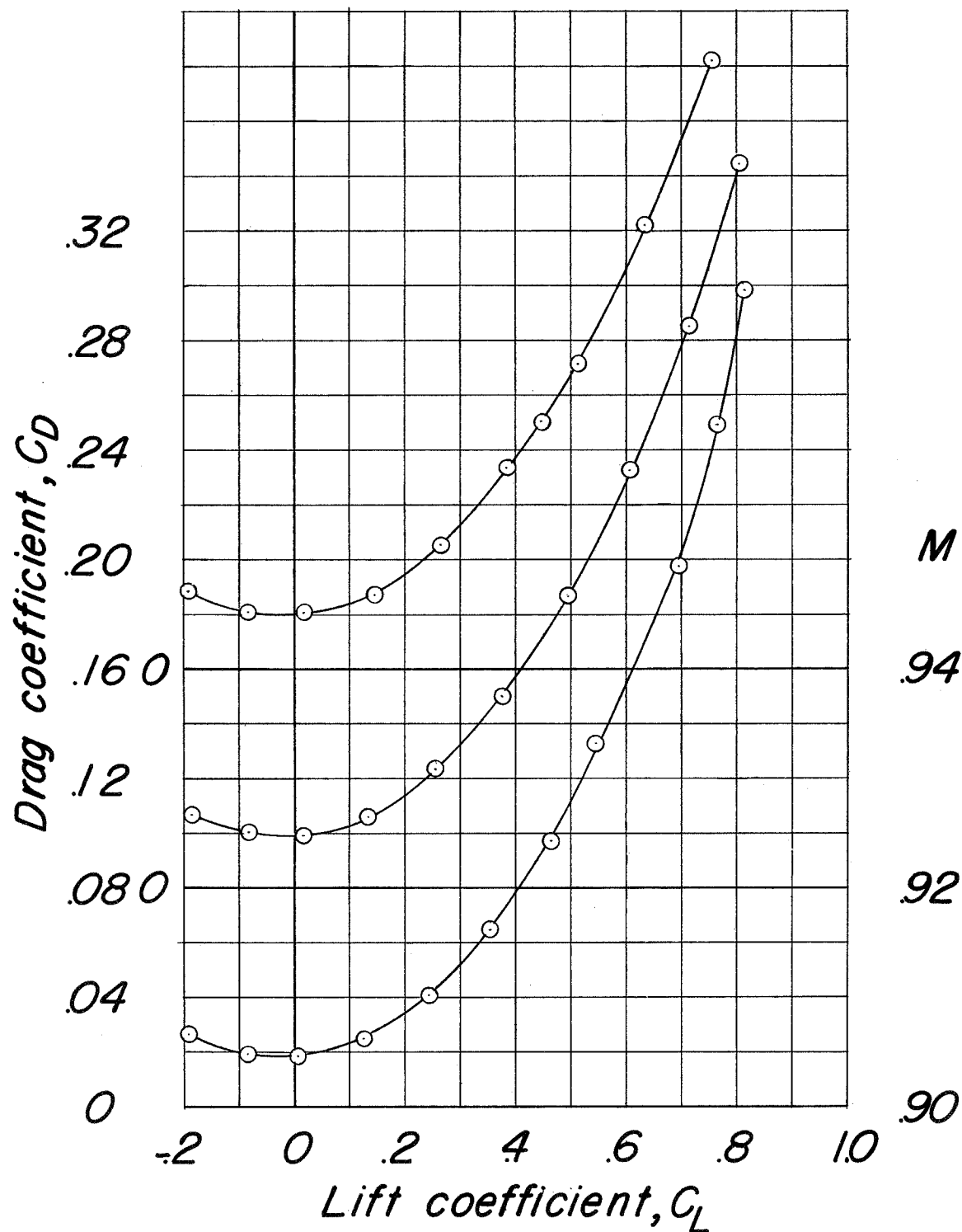
(c) C_D against C_L .

Figure 15.- Continued.



(c) Concluded.

Figure 15.- Continued.

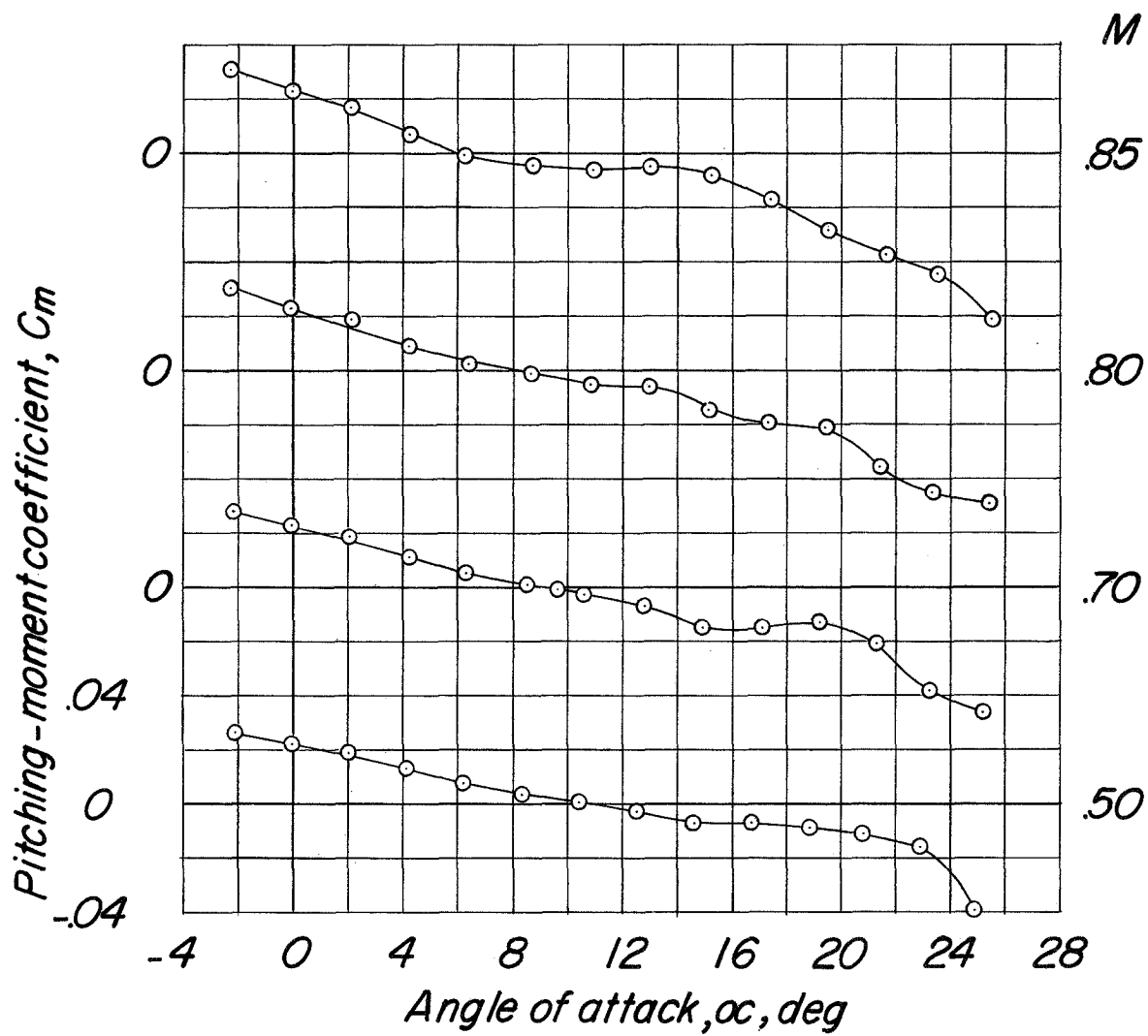
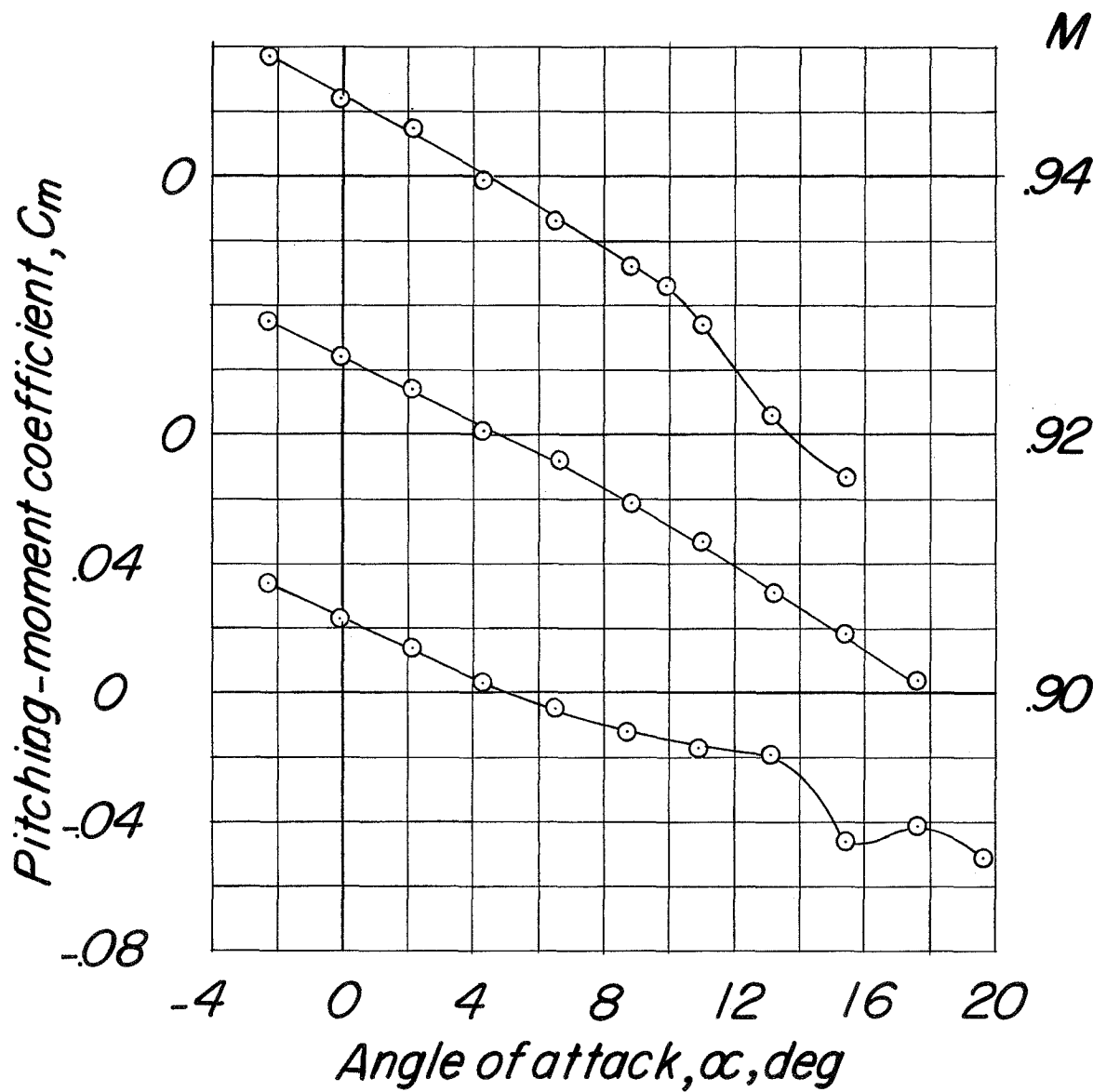
(a) C_m against α .

Figure 15.- Continued.



(d) Concluded.

Figure 15.- Continued.

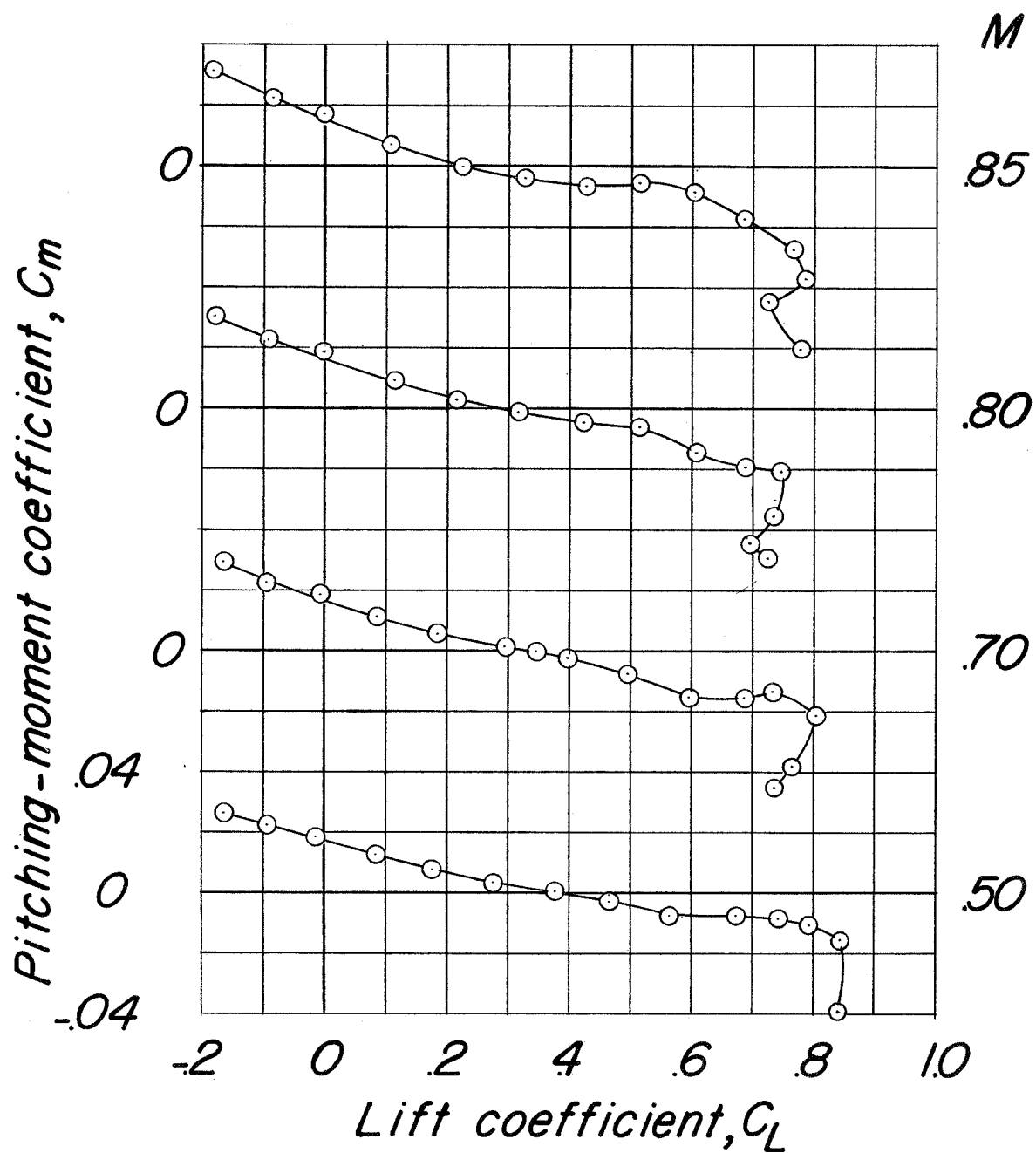
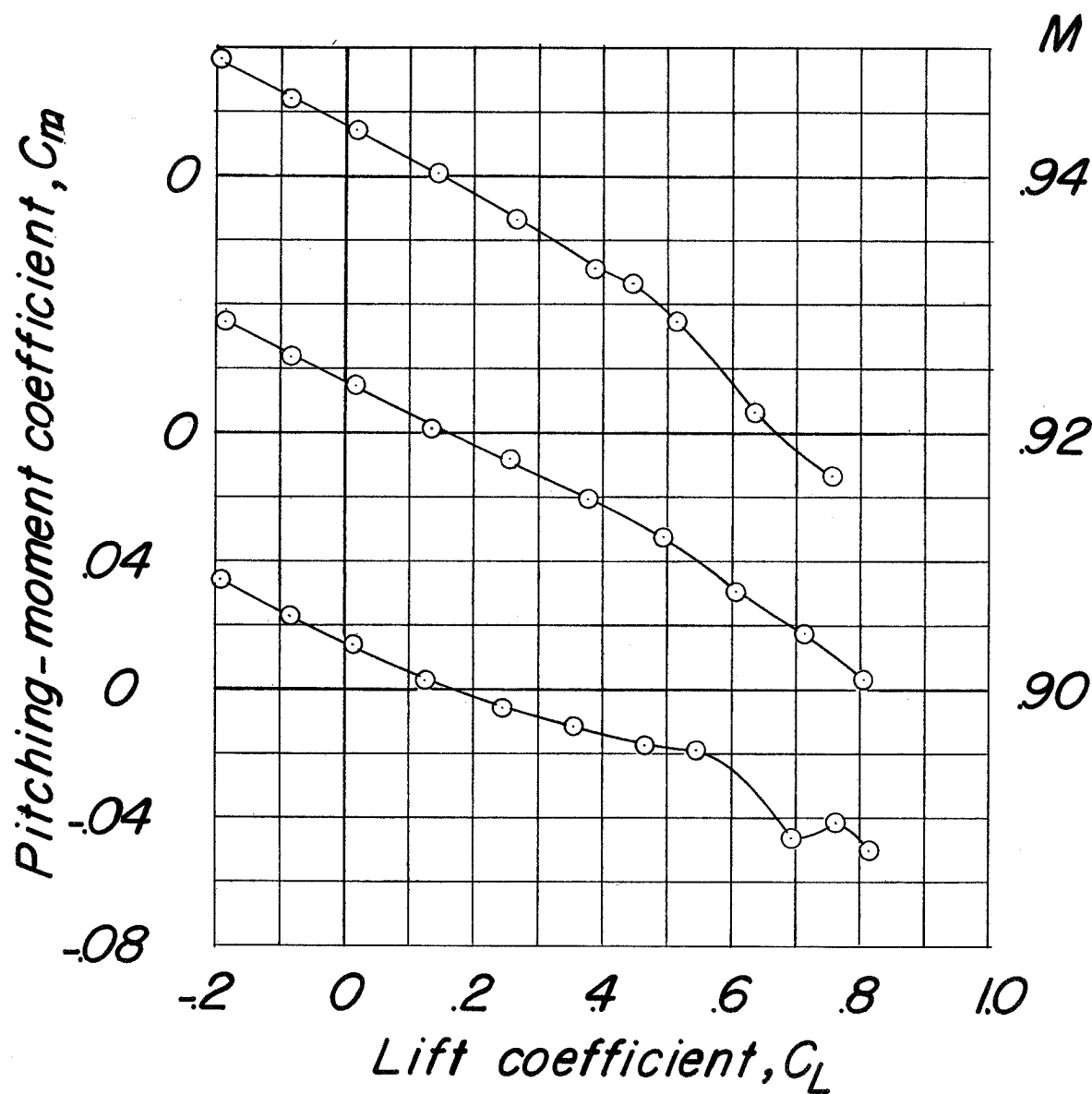
(e) C_m against C_L .

Figure 15.- Continued.



(e) Concluded.

Figure 15.- Concluded.

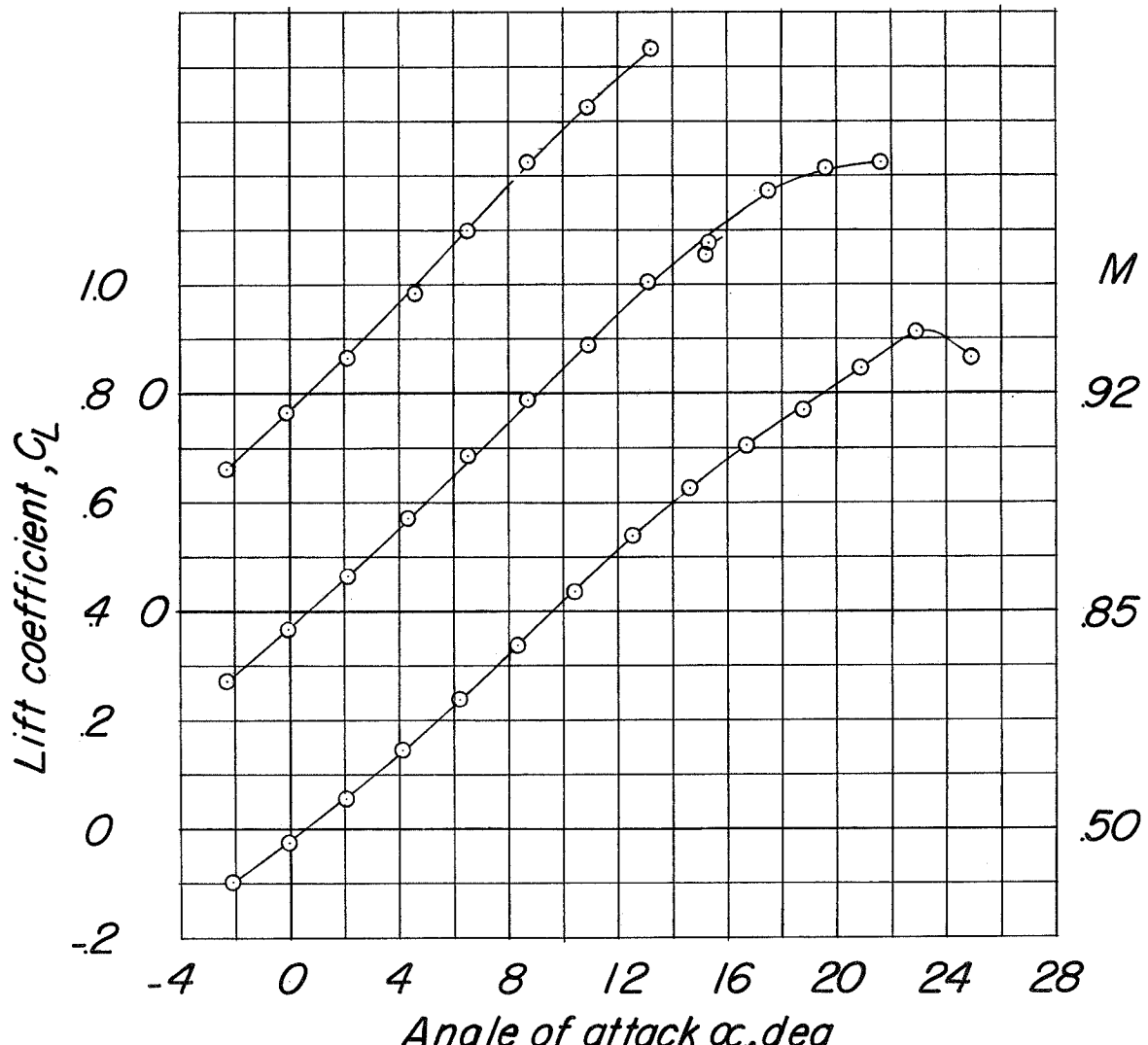
(a) C_L against α .

Figure 16.- Basic longitudinal characteristics for configuration BCWF₁ V,
 $\delta_r = 10^\circ$, $\delta_e = 0^\circ$.

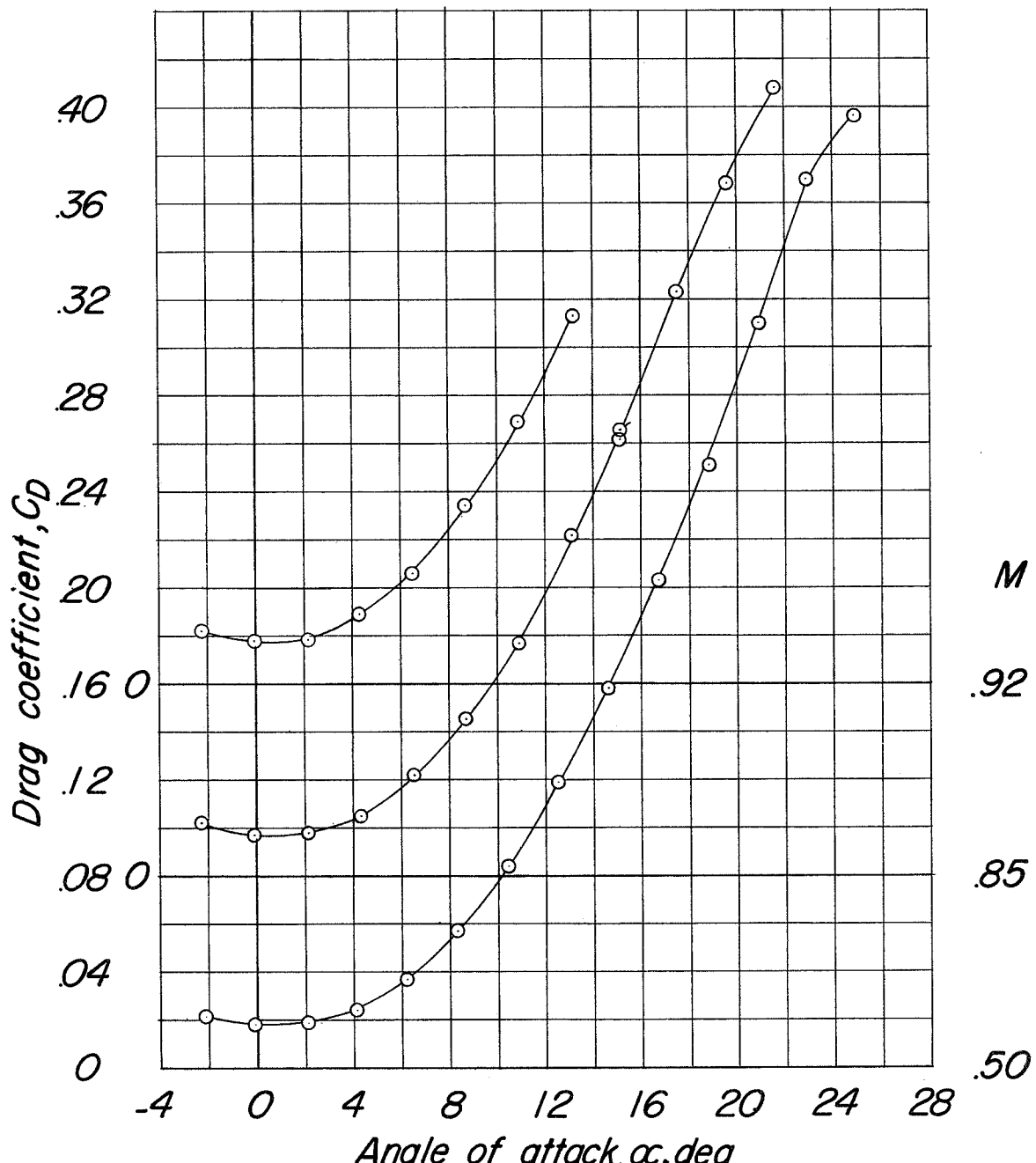
(b) C_D against α .

Figure 16.- Continued.

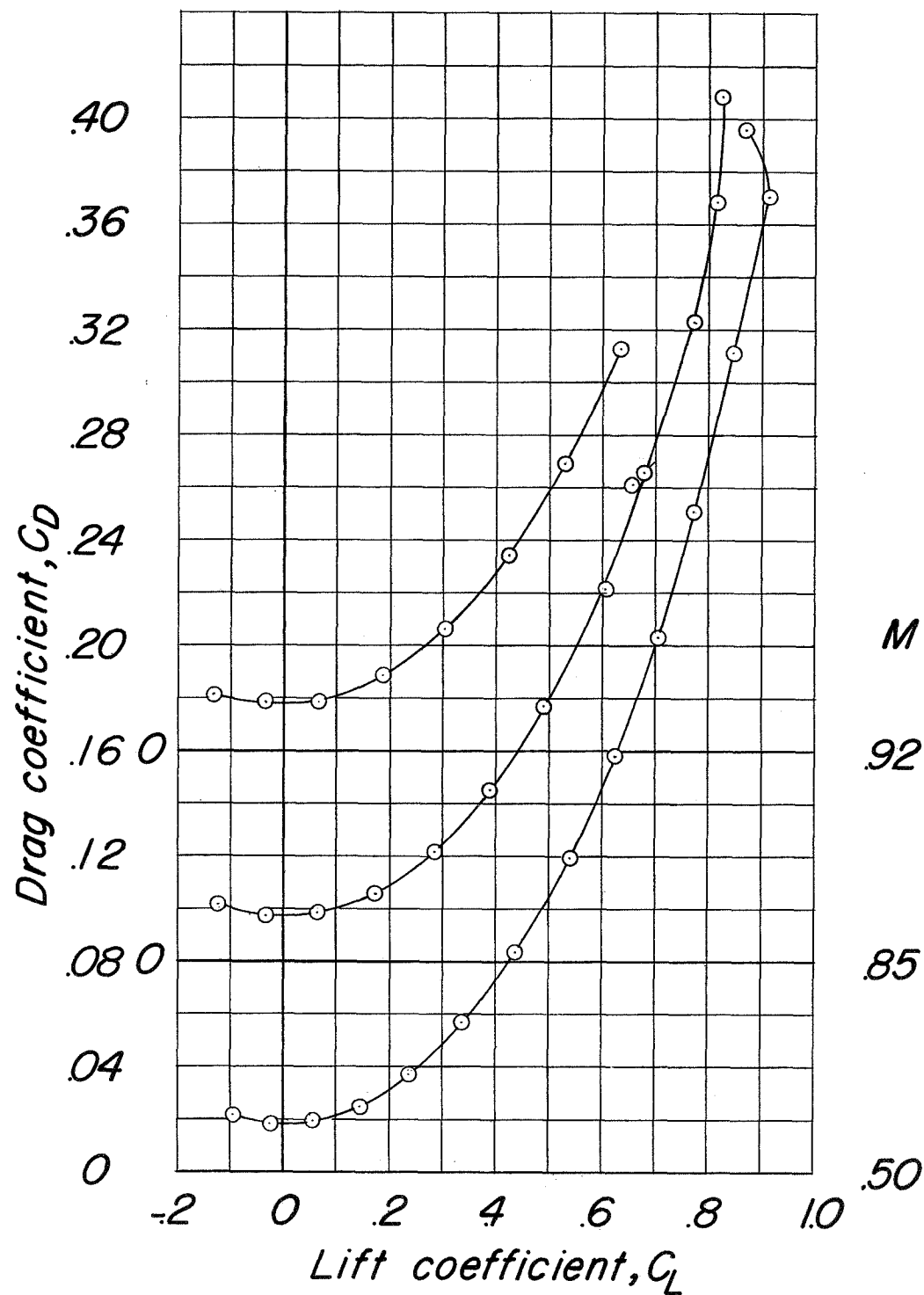
(c) C_D against C_L .

Figure 16.- Continued.

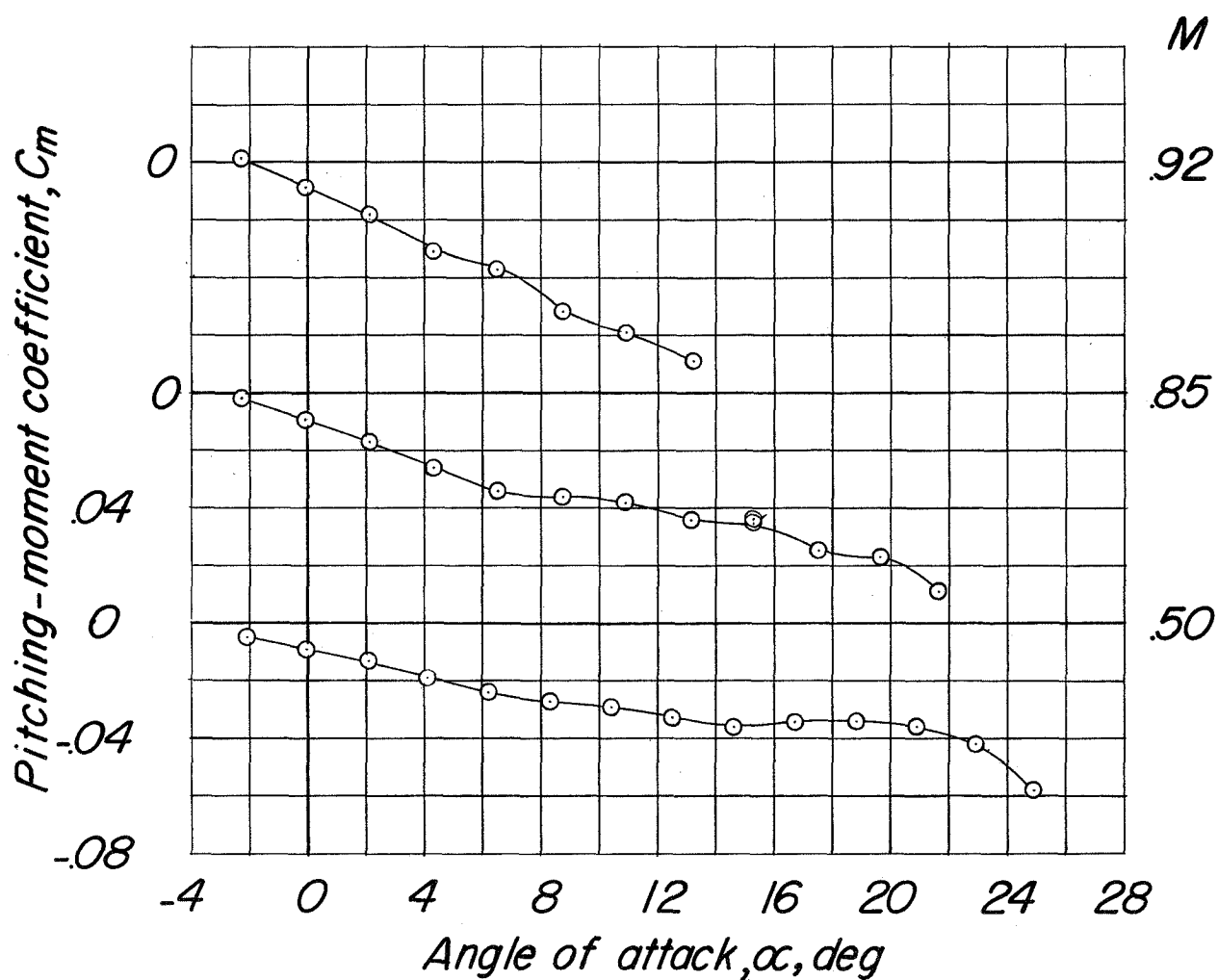
(d) C_m against α .

Figure 16.- Continued.

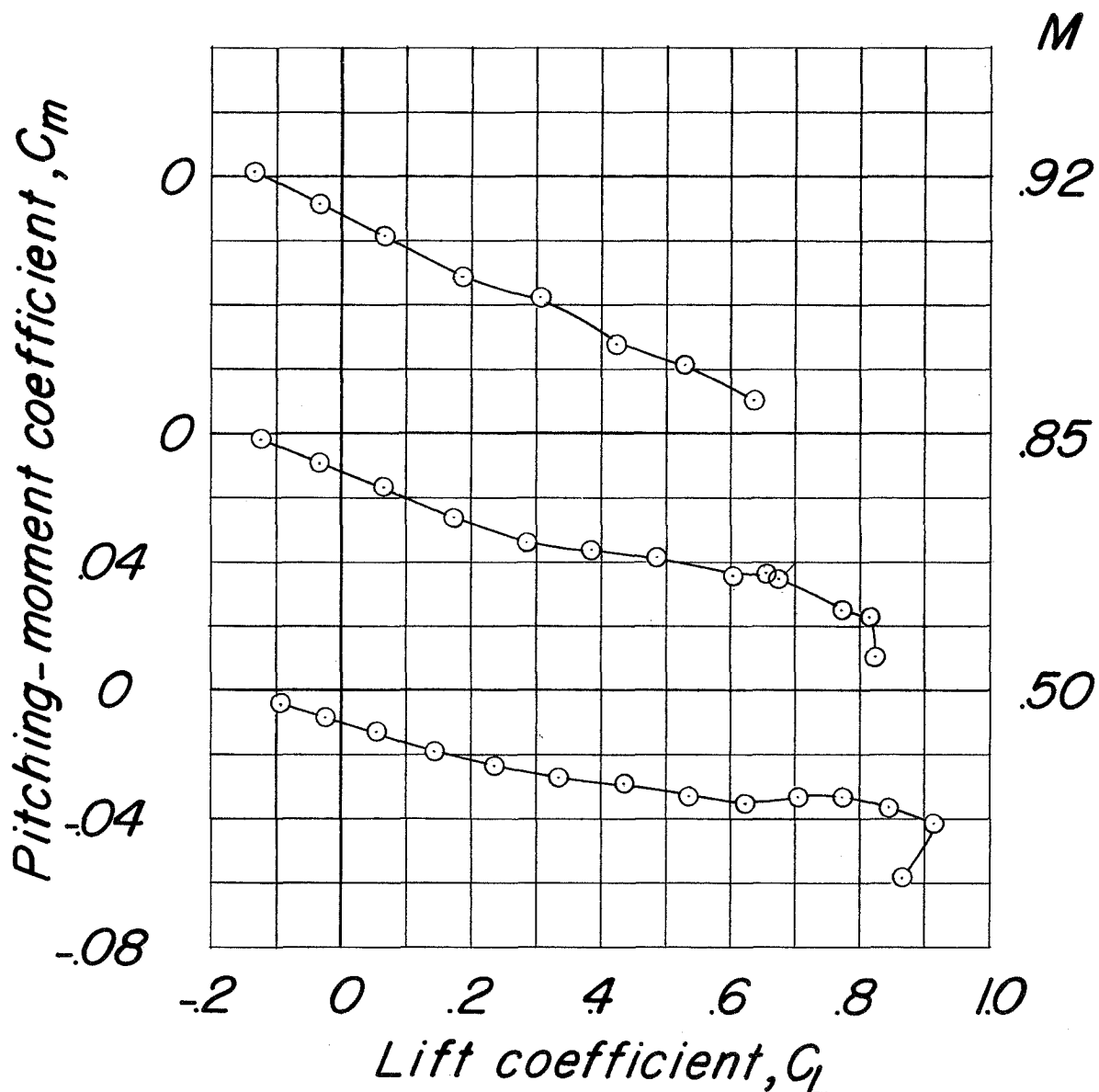
(e) C_m against C_L .

Figure 16.- Concluded.

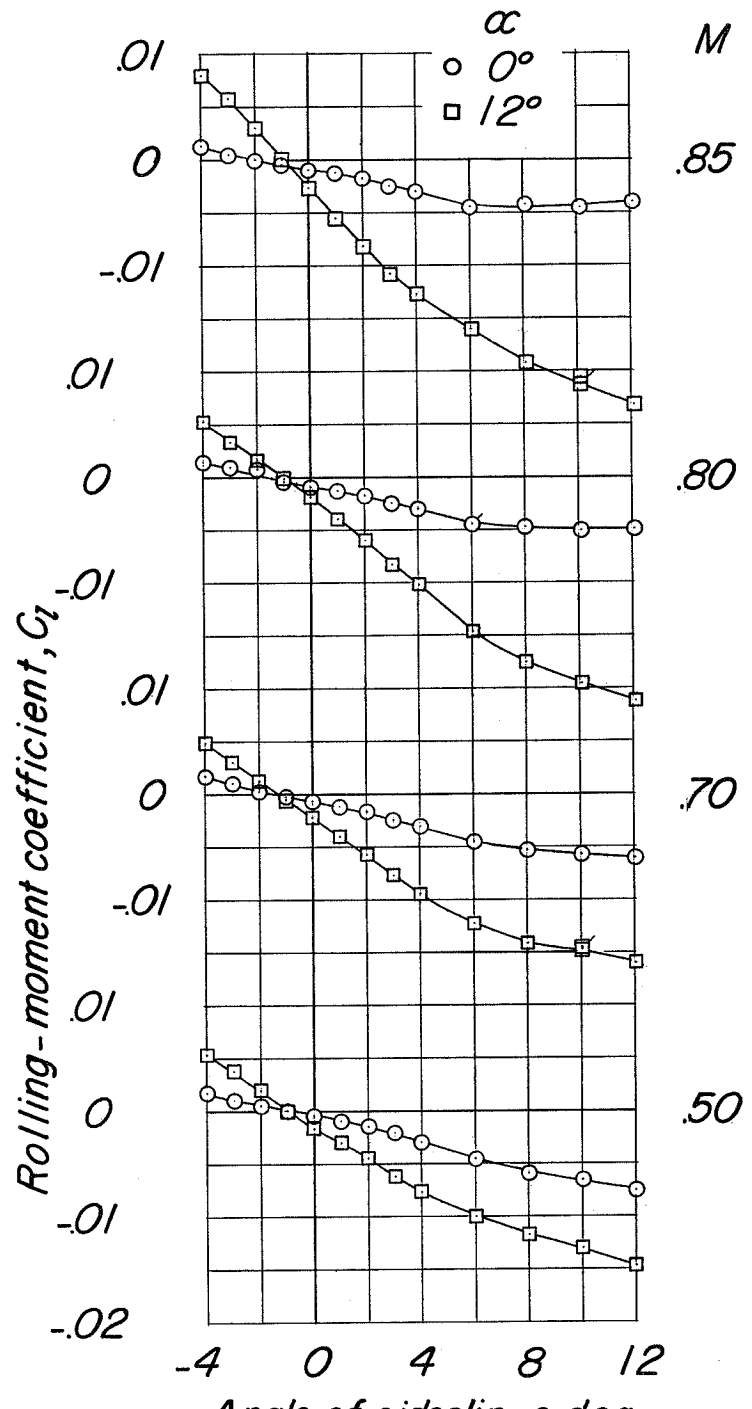
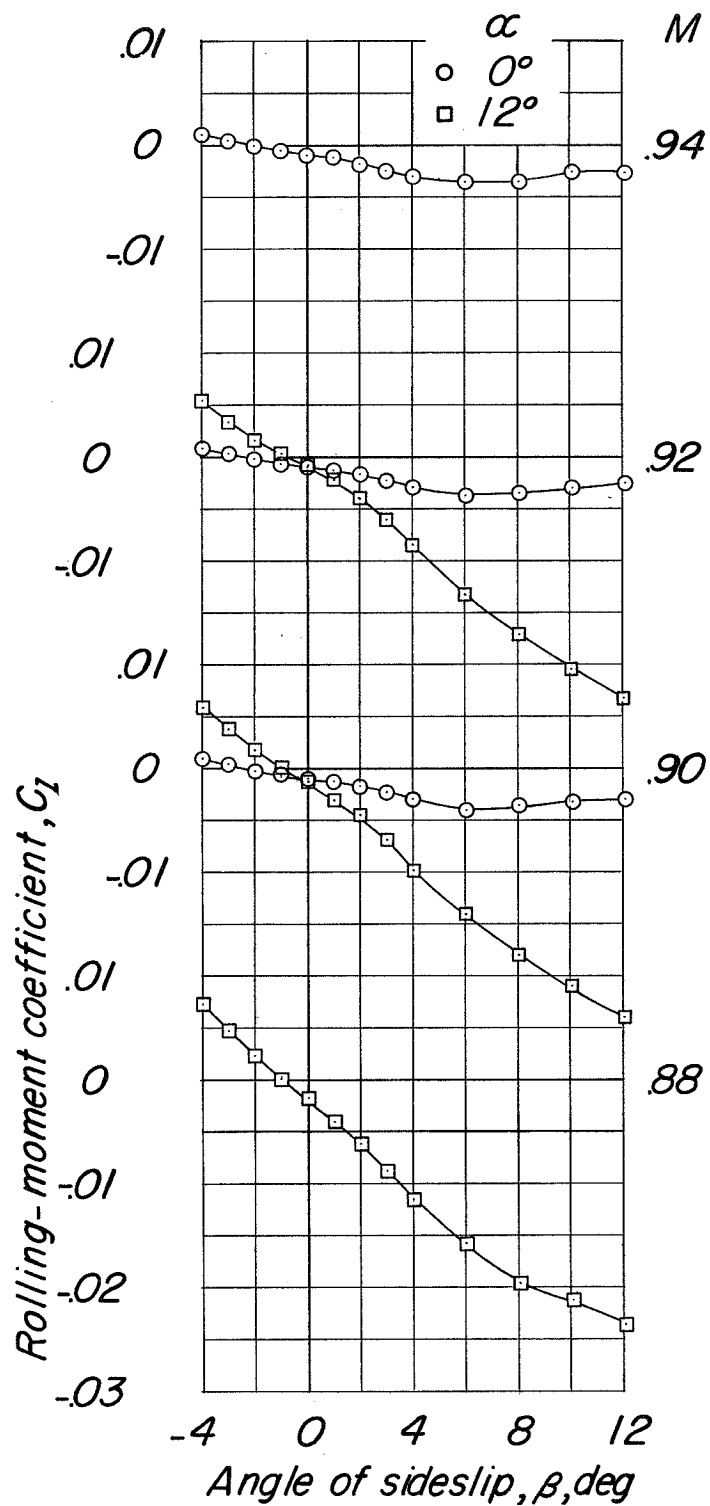
(a) C_l against β .

Figure 17.- Variation of lateral coefficients with angle of sideslip for configuration BCWV, $\delta_e = 0^\circ$, $\delta_r = 0^\circ$.



(a) Concluded.

Figure 17.- Continued.

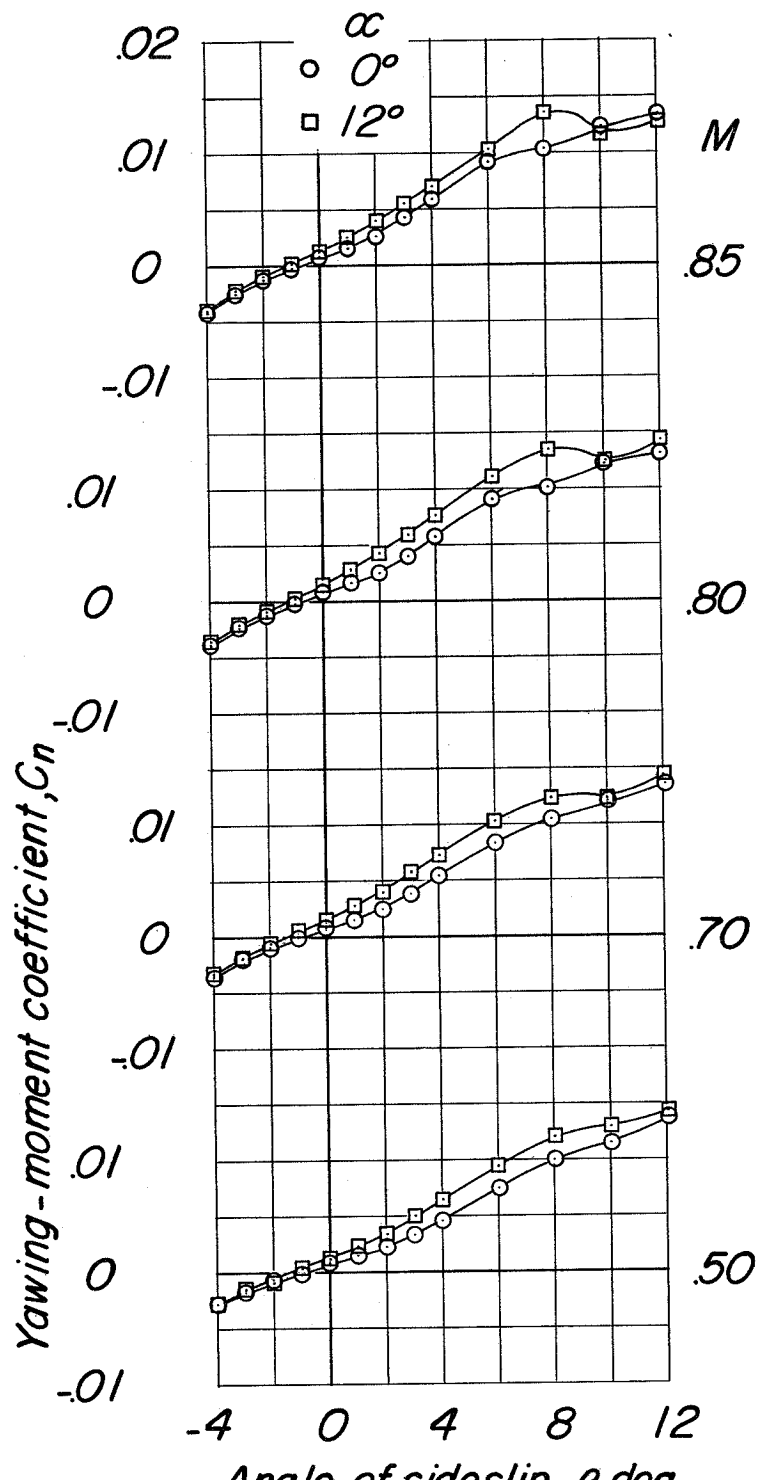
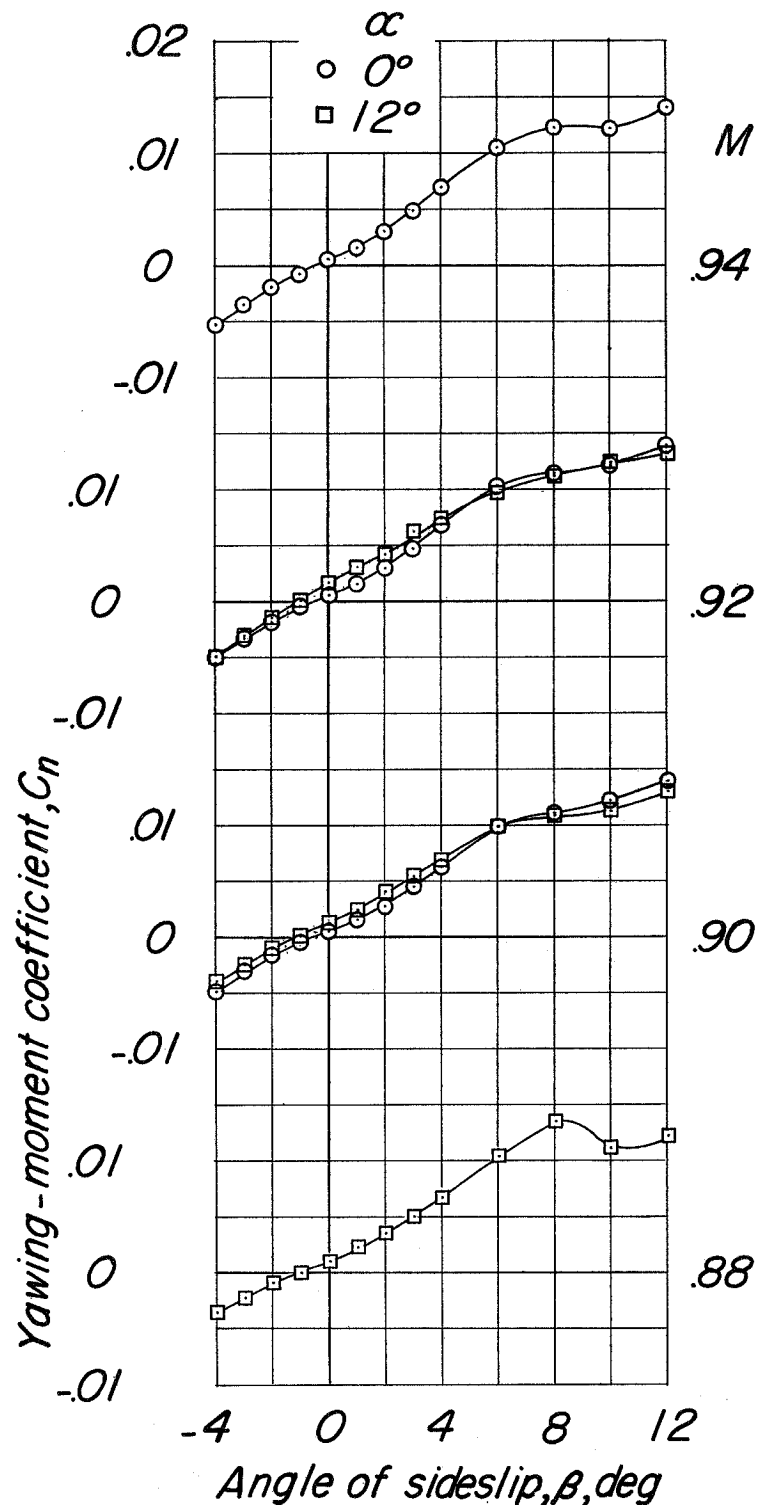
(b) C_n against β .

Figure 17.-- Continued.



(b) Concluded.

Figure 17.- Continued.

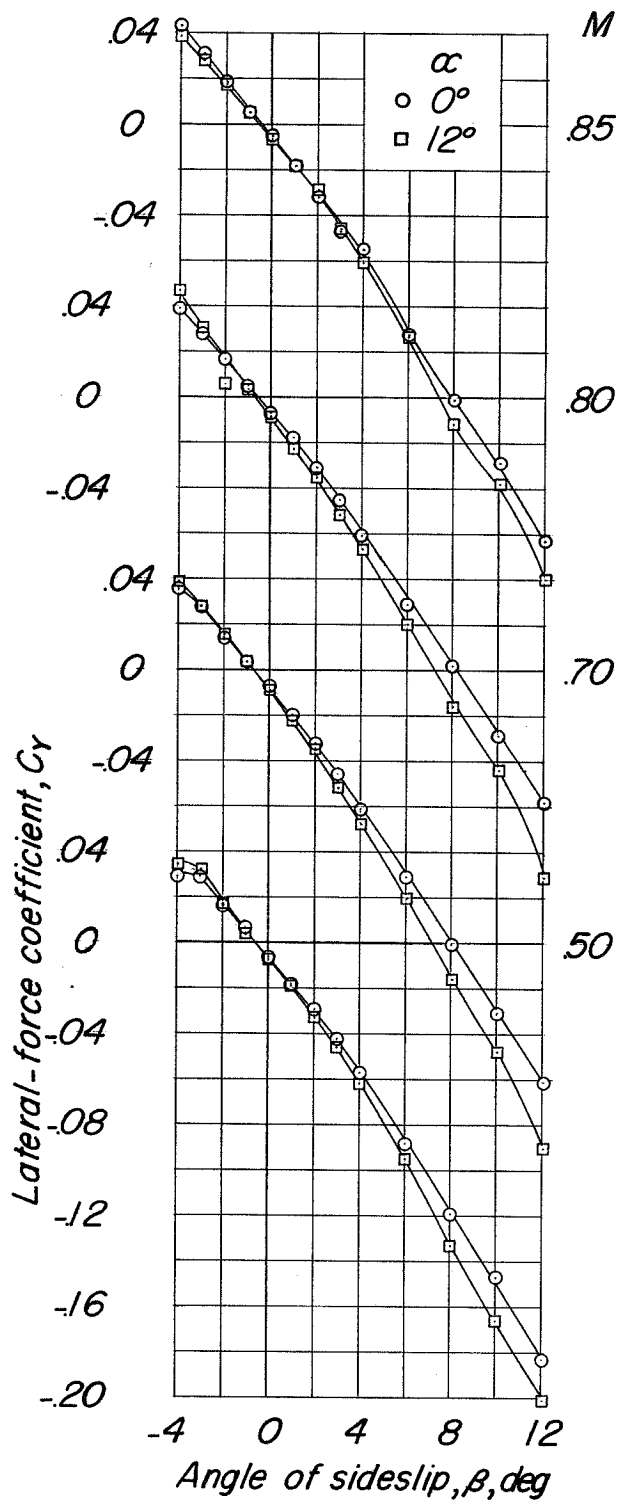
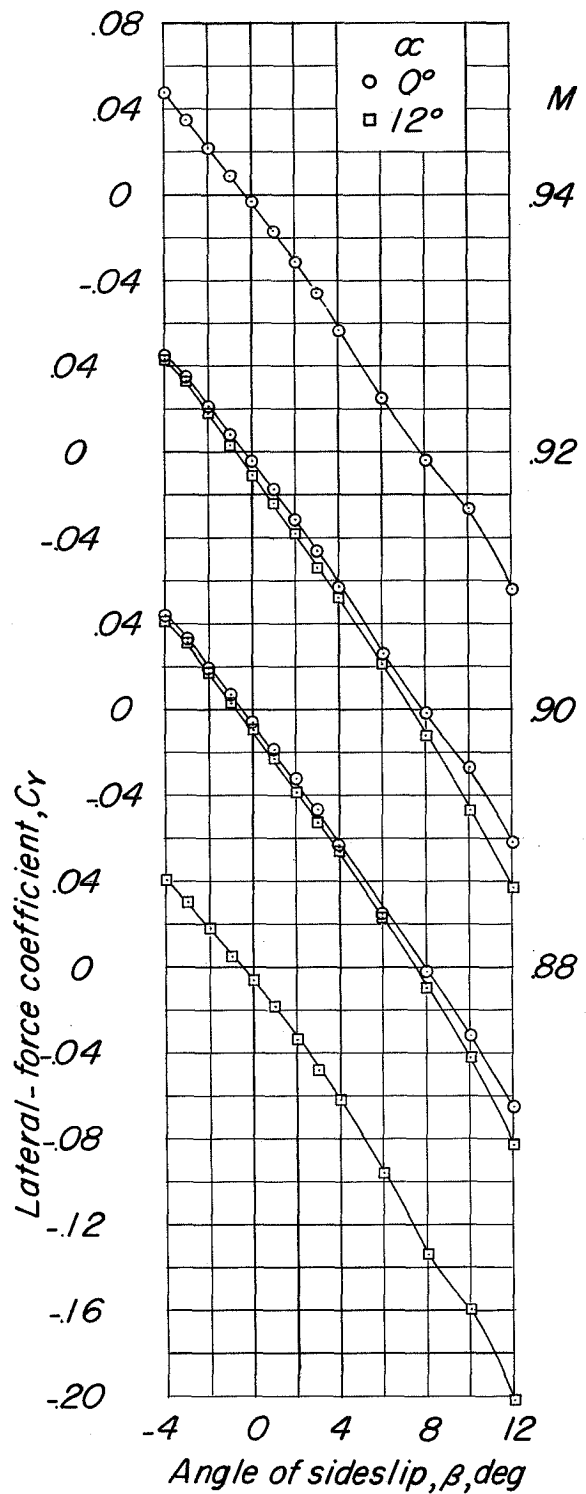
(c) C_y against β .

Figure 17.- Continued.



(c) Concluded.

Figure 17.- Concluded.

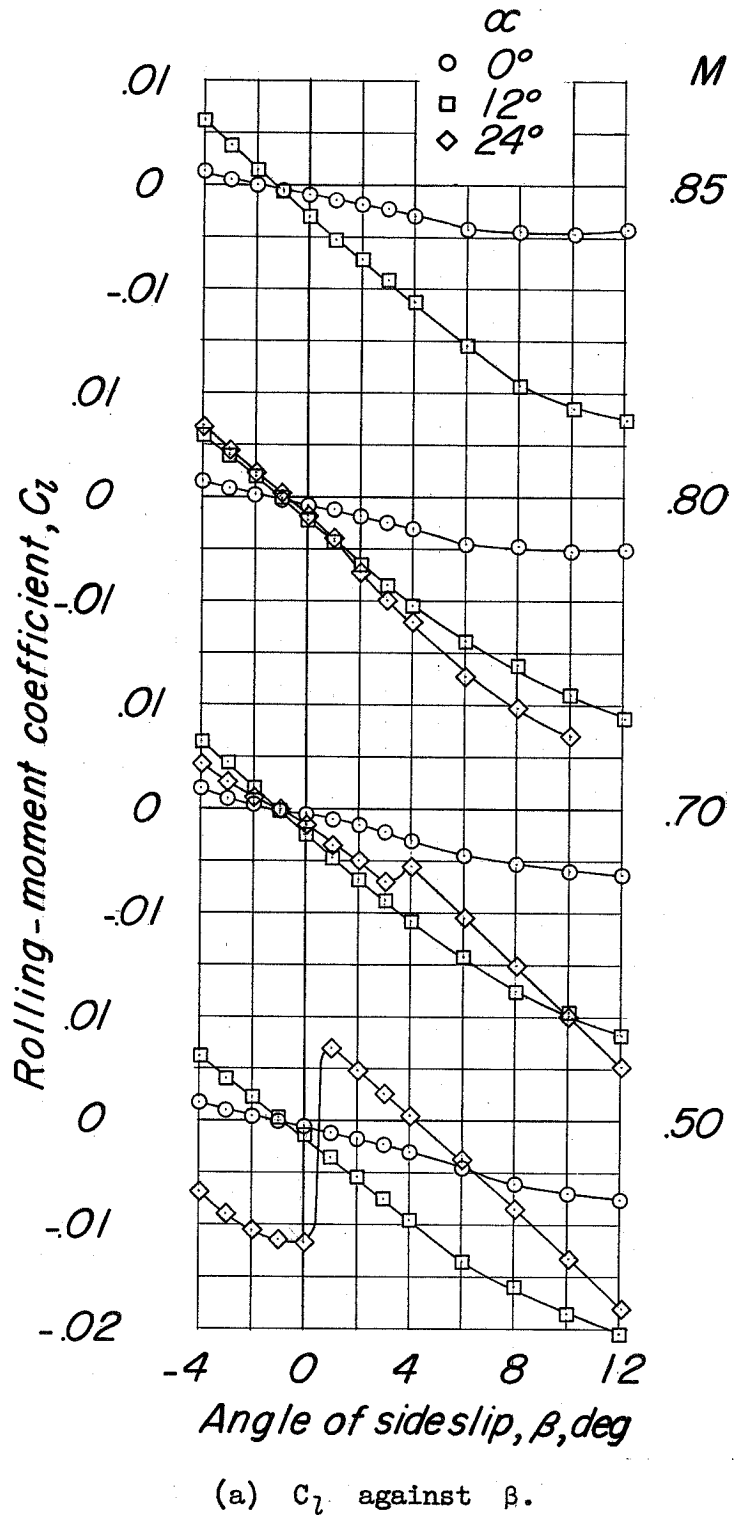
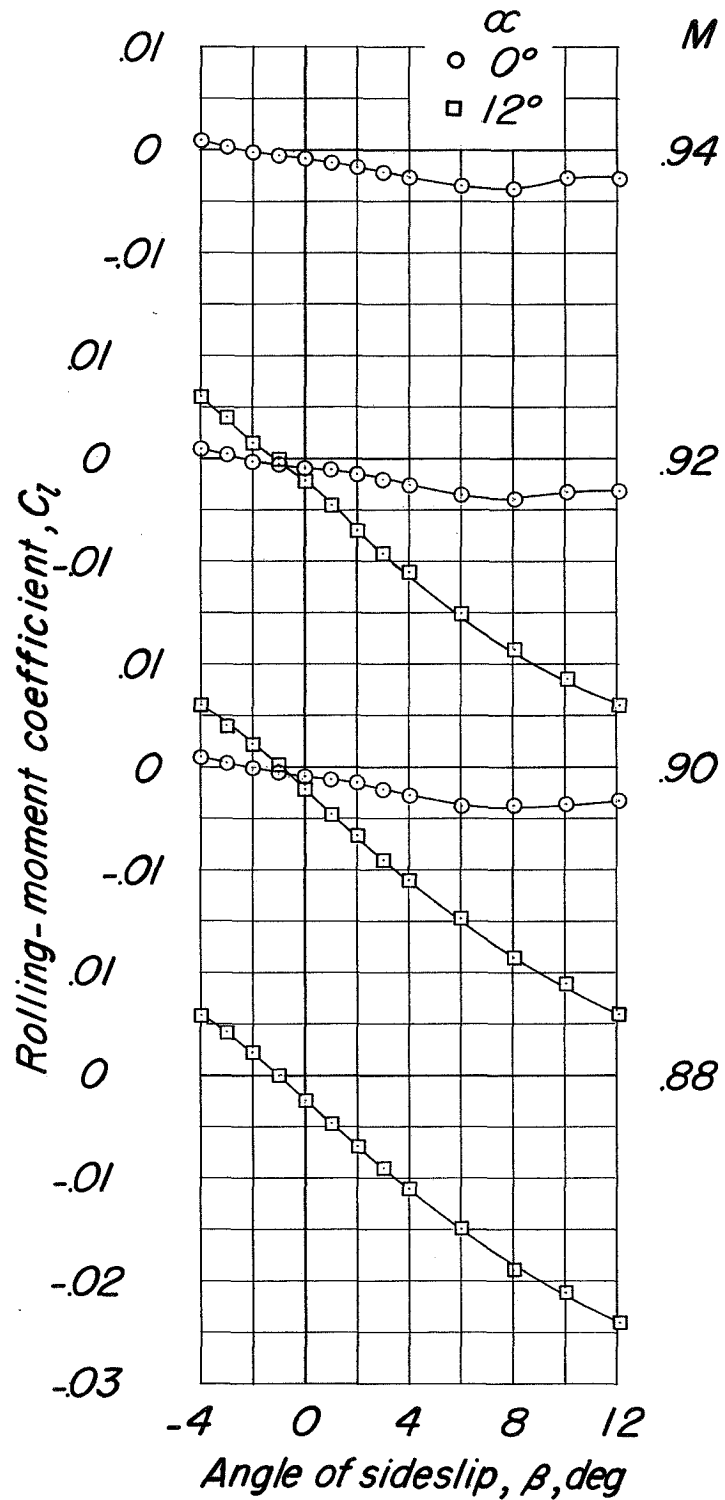
(a) C_l against β .

Figure 18.- Variation of lateral coefficients with angle of sideslip for configuration BCWF₁V, $\delta_e = 0^\circ$, $\delta_r = 0^\circ$.



(a) Concluded.

Figure 18.- Continued.

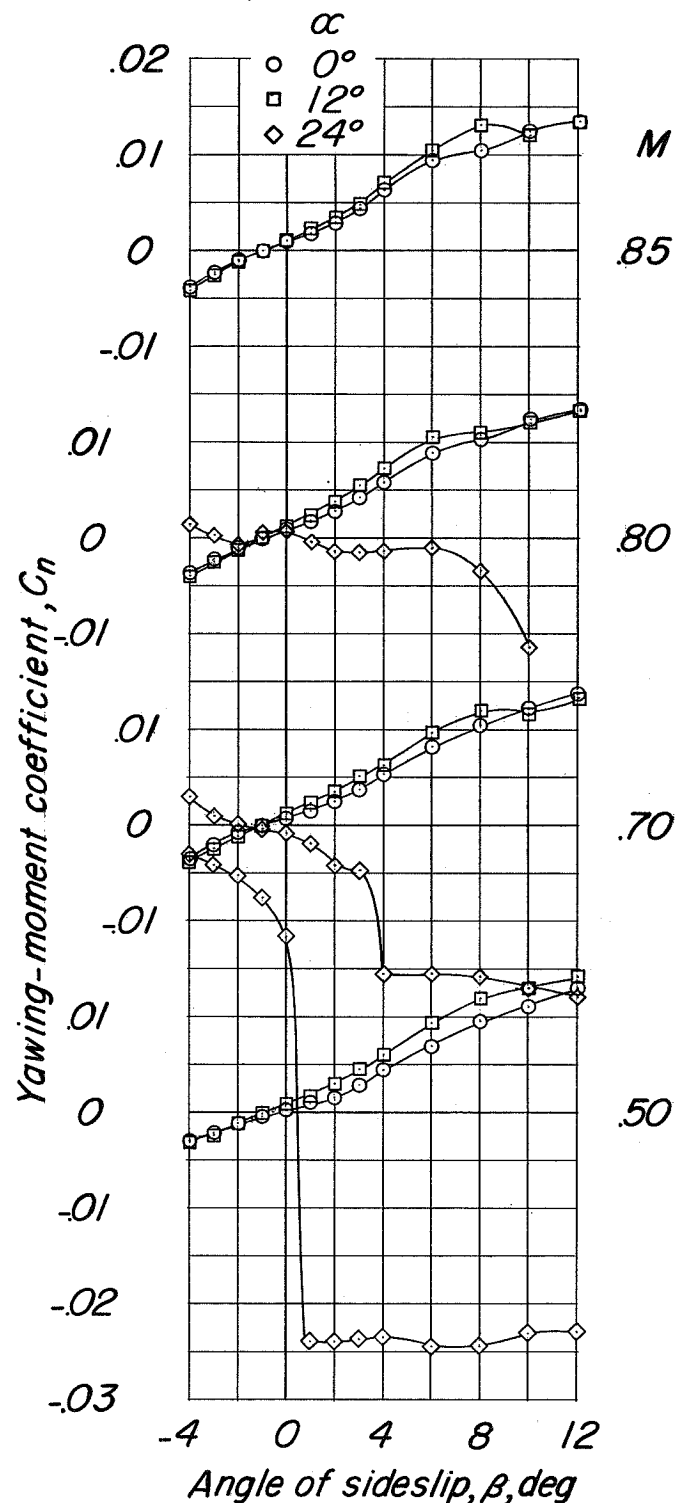
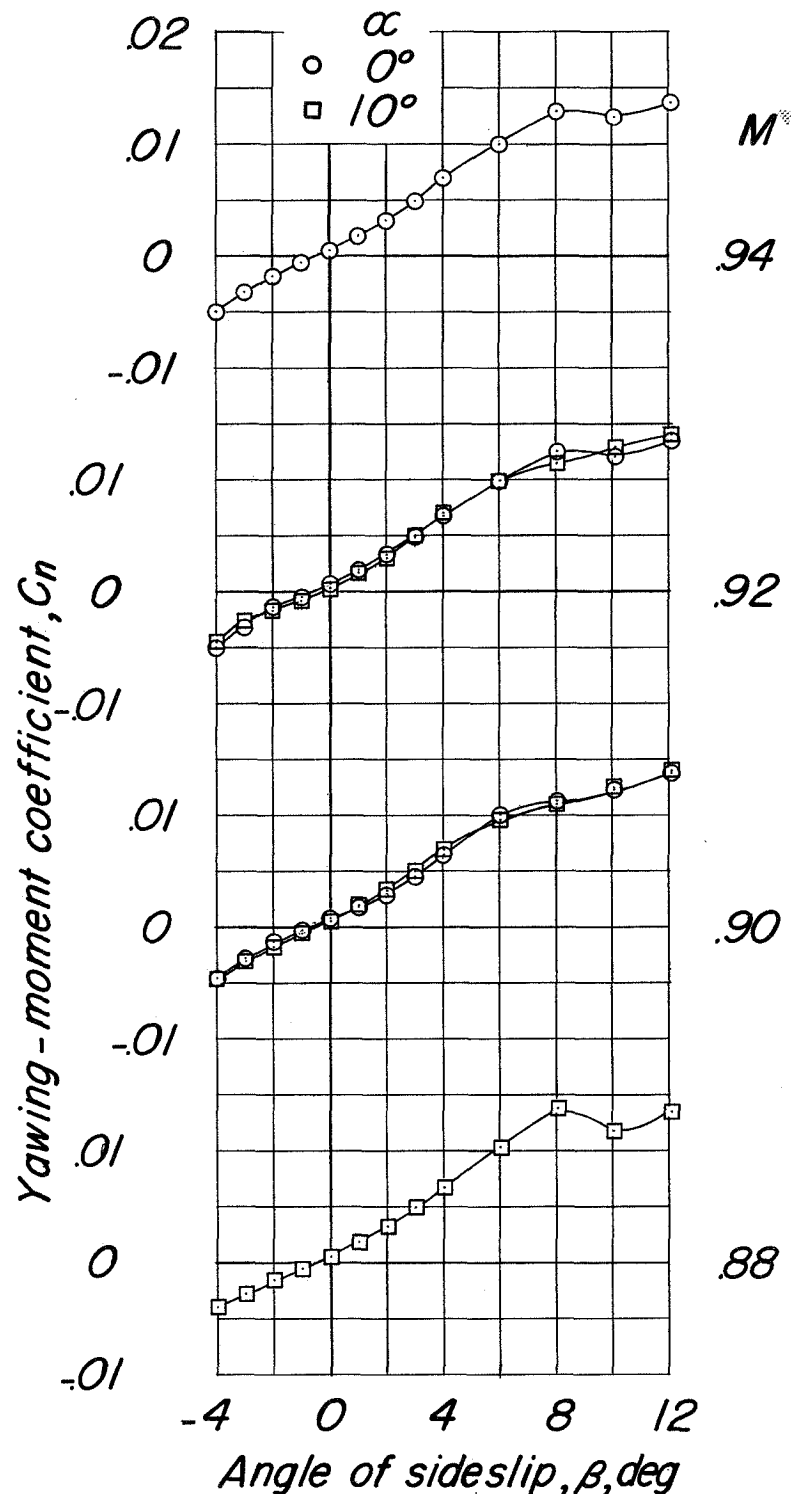


Figure 18.- Continued.



(b) Concluded.

Figure 18.- Continued.

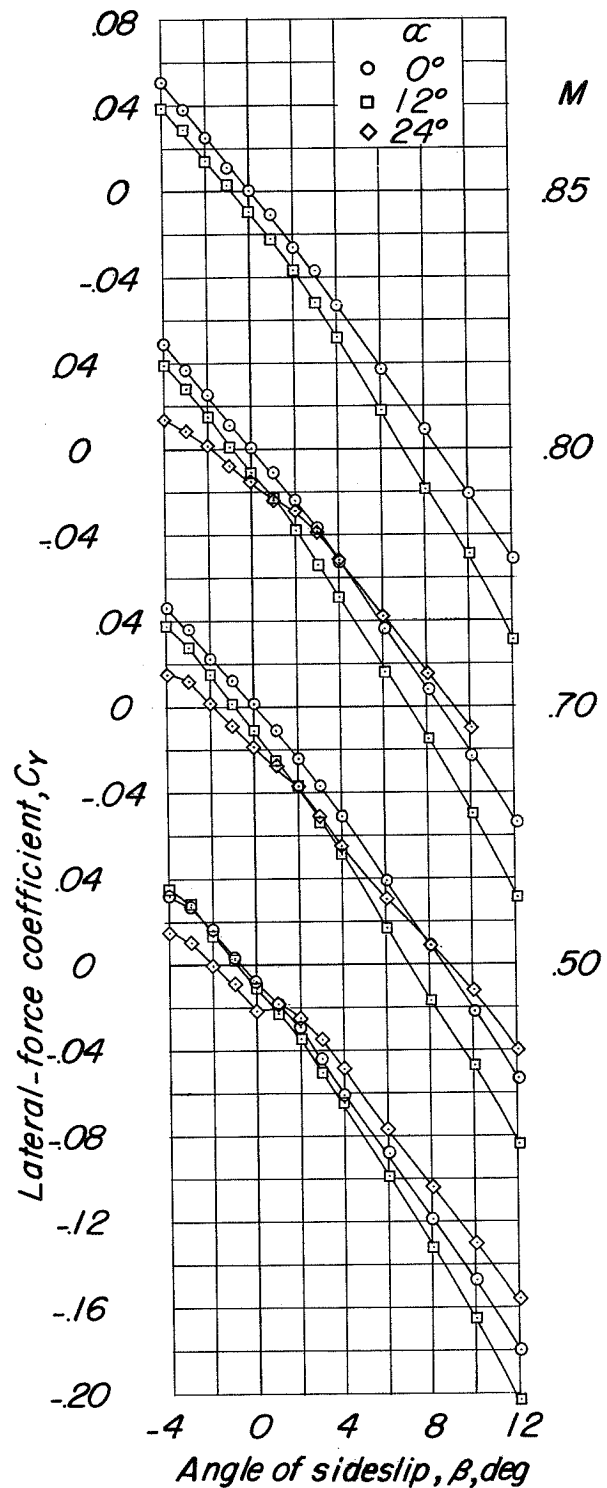
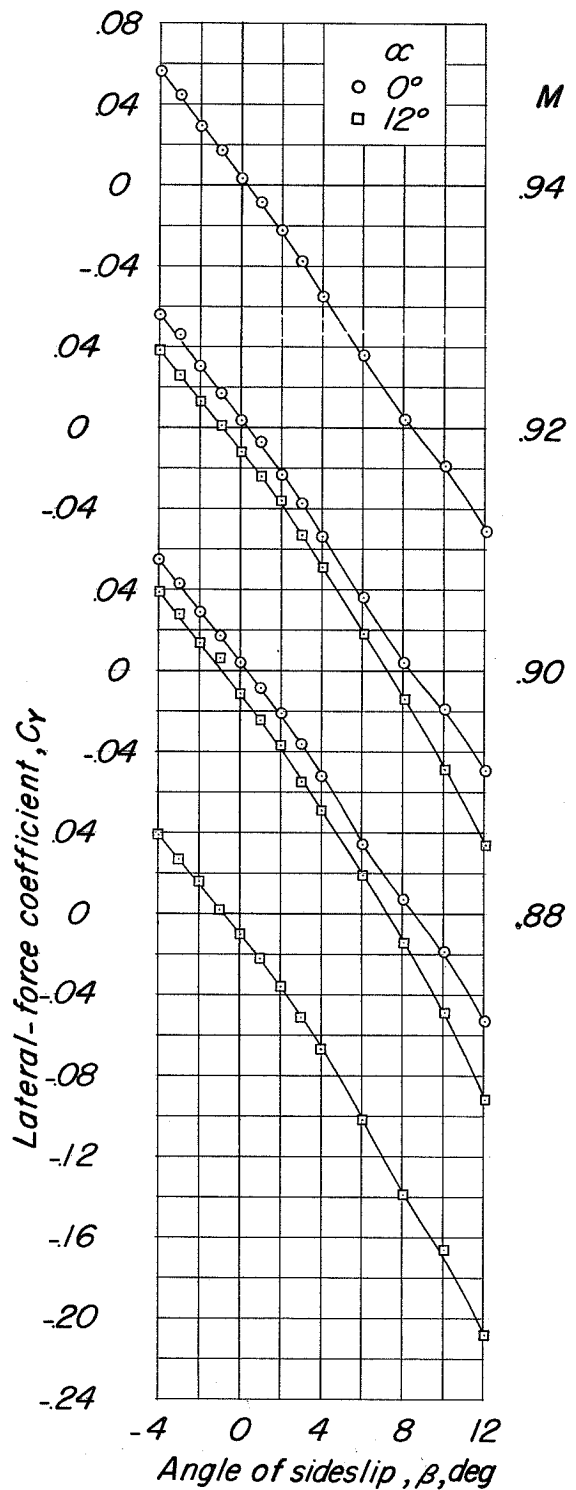
(c) C_Y against β .

Figure 18.- Continued.



(c) Concluded.

Figure 18.- Concluded.

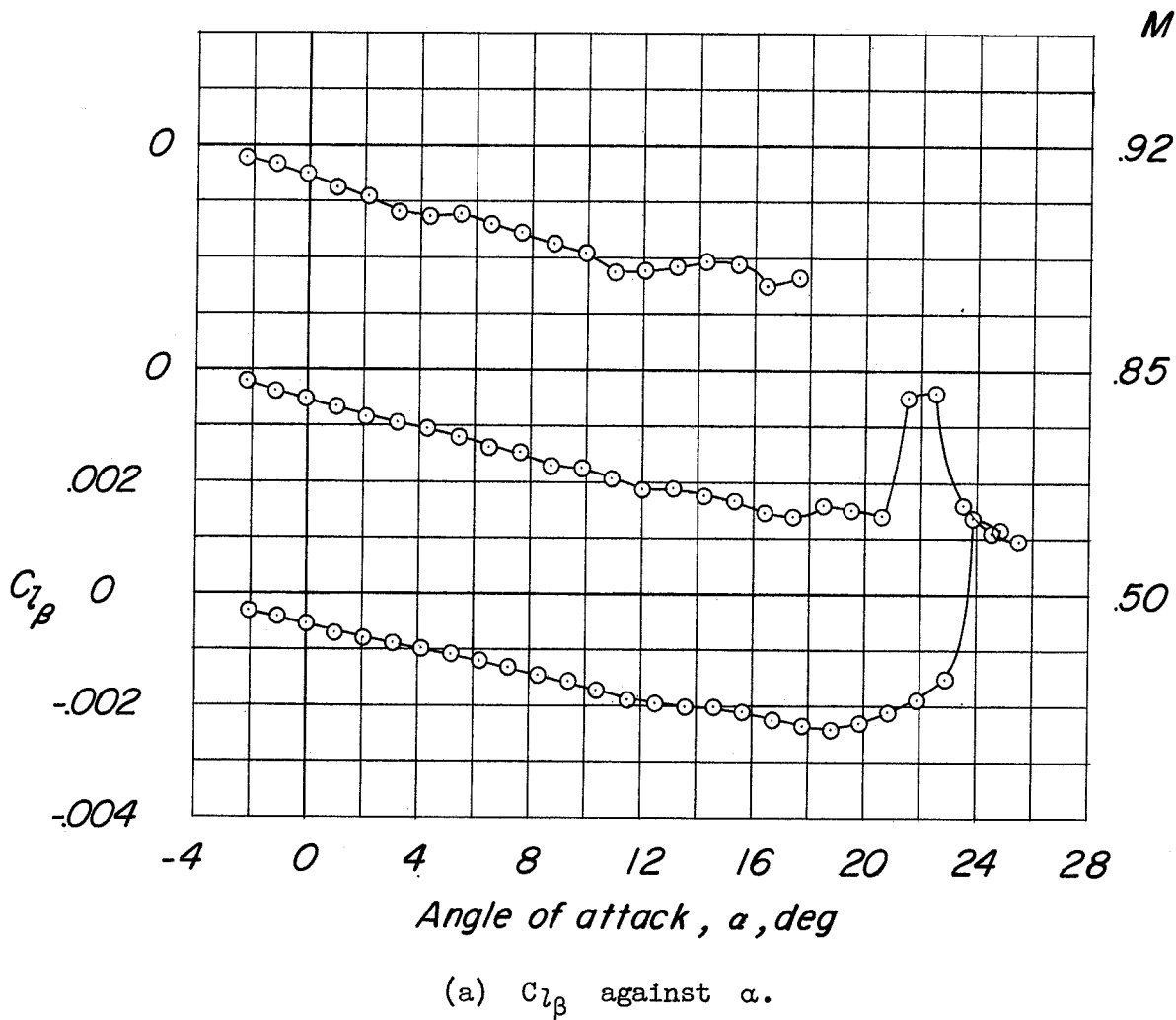
(a) $C_{l\beta}$ against α .

Figure 19.- Variation of lateral-stability parameters with angle of attack for configuration ECWF₁V, $\delta_e = 0^\circ$, $\delta_r = 0^\circ$. (Lateral-stability parameters evaluated from angle-of-attack tests at $\beta = \pm 4^\circ$.)

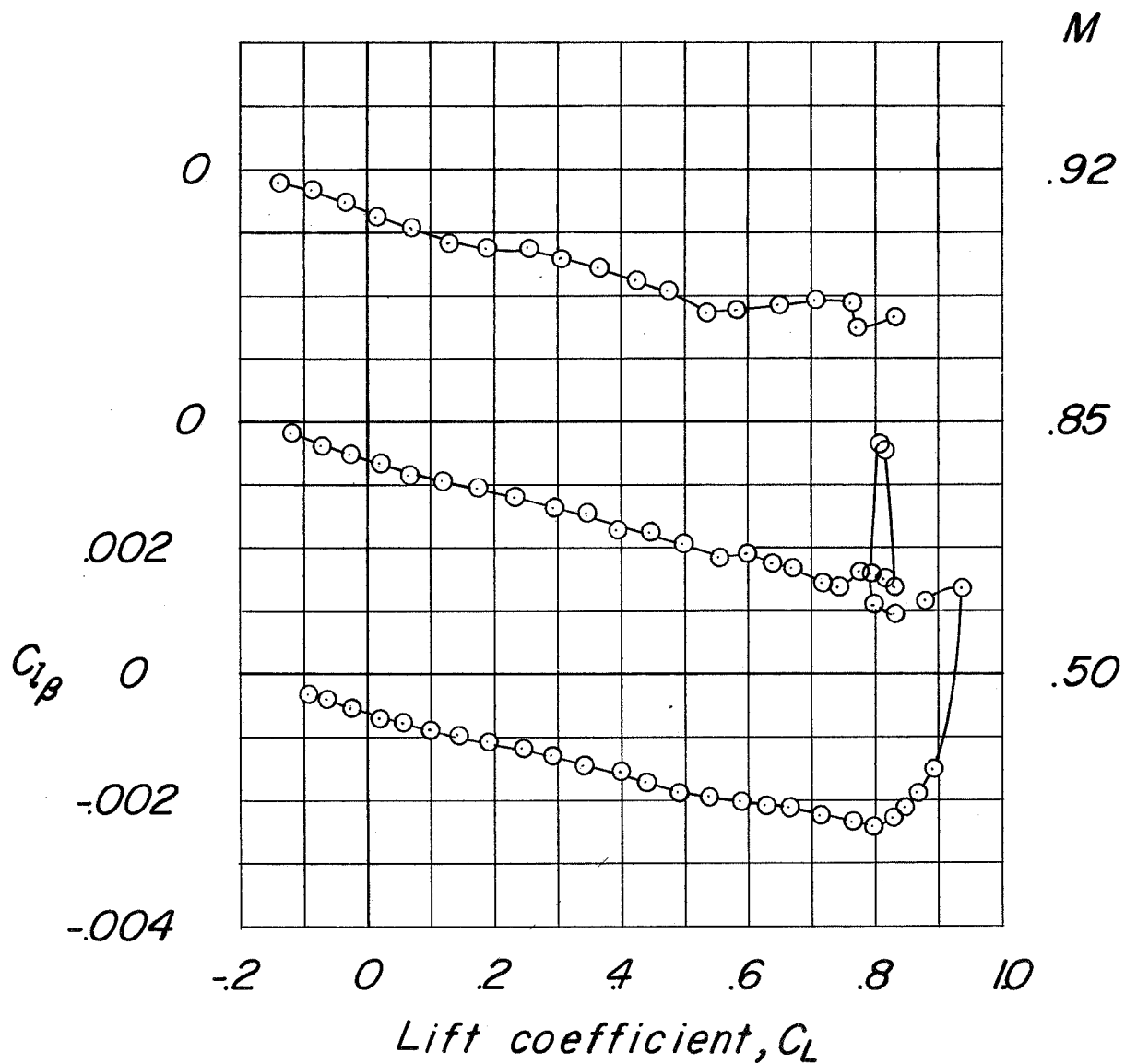
(b) $C_{l\beta}$ against C_L .

Figure 19.- Continued.

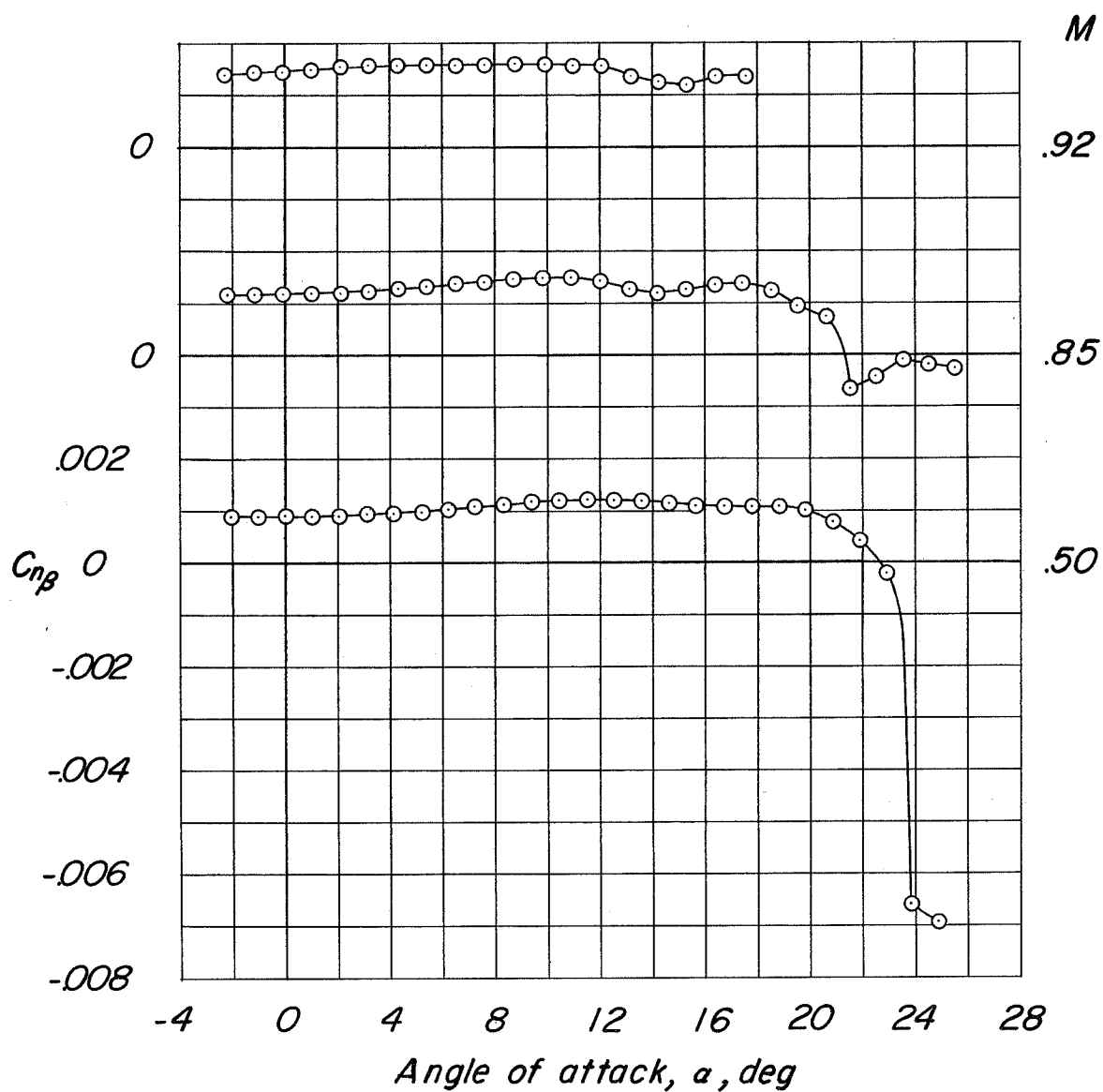
(c) C_{n_B} against α .

Figure 19.- Continued.

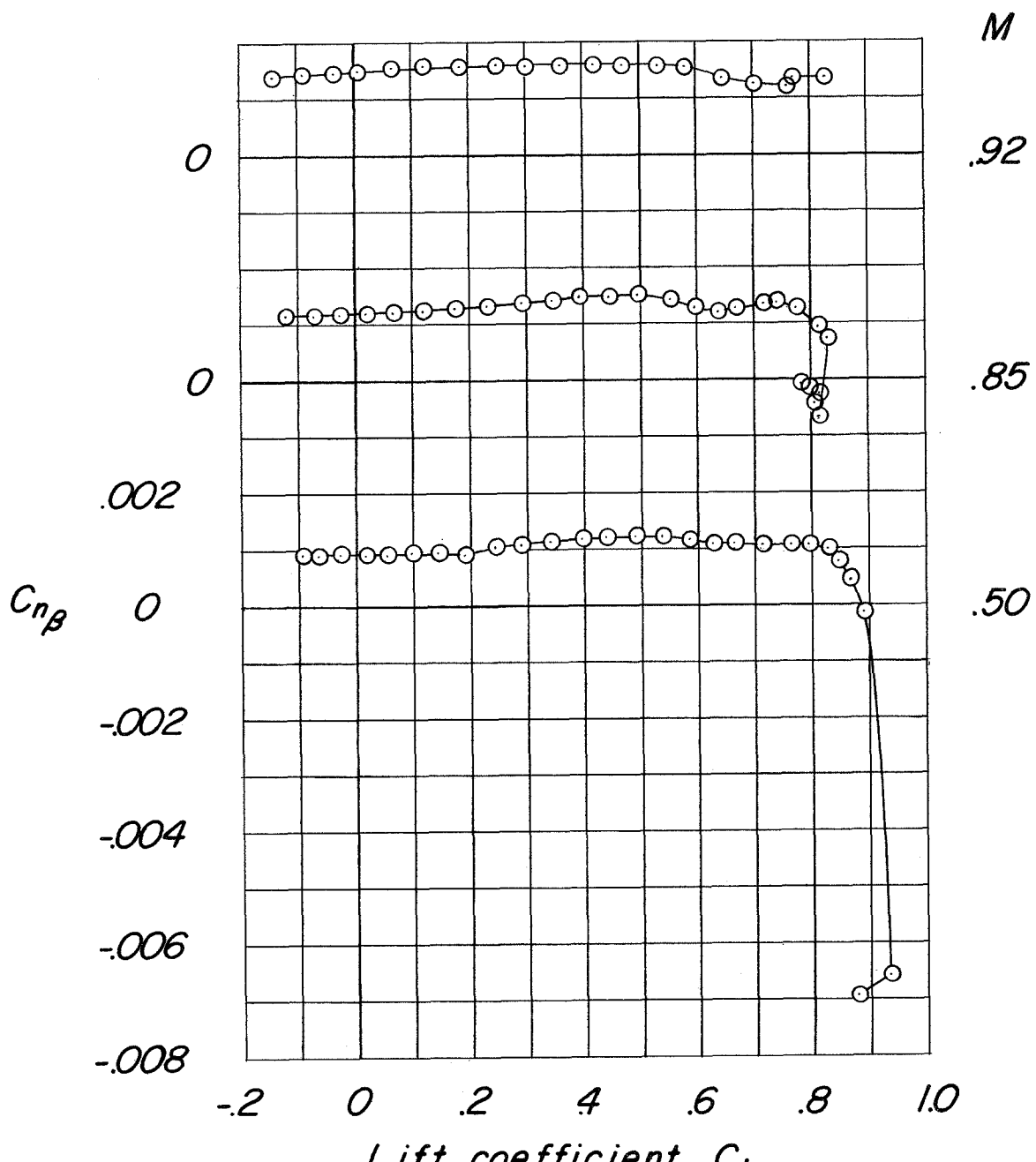
(d) $C_{n\beta}$ against C_L .

Figure 19.- Continued.

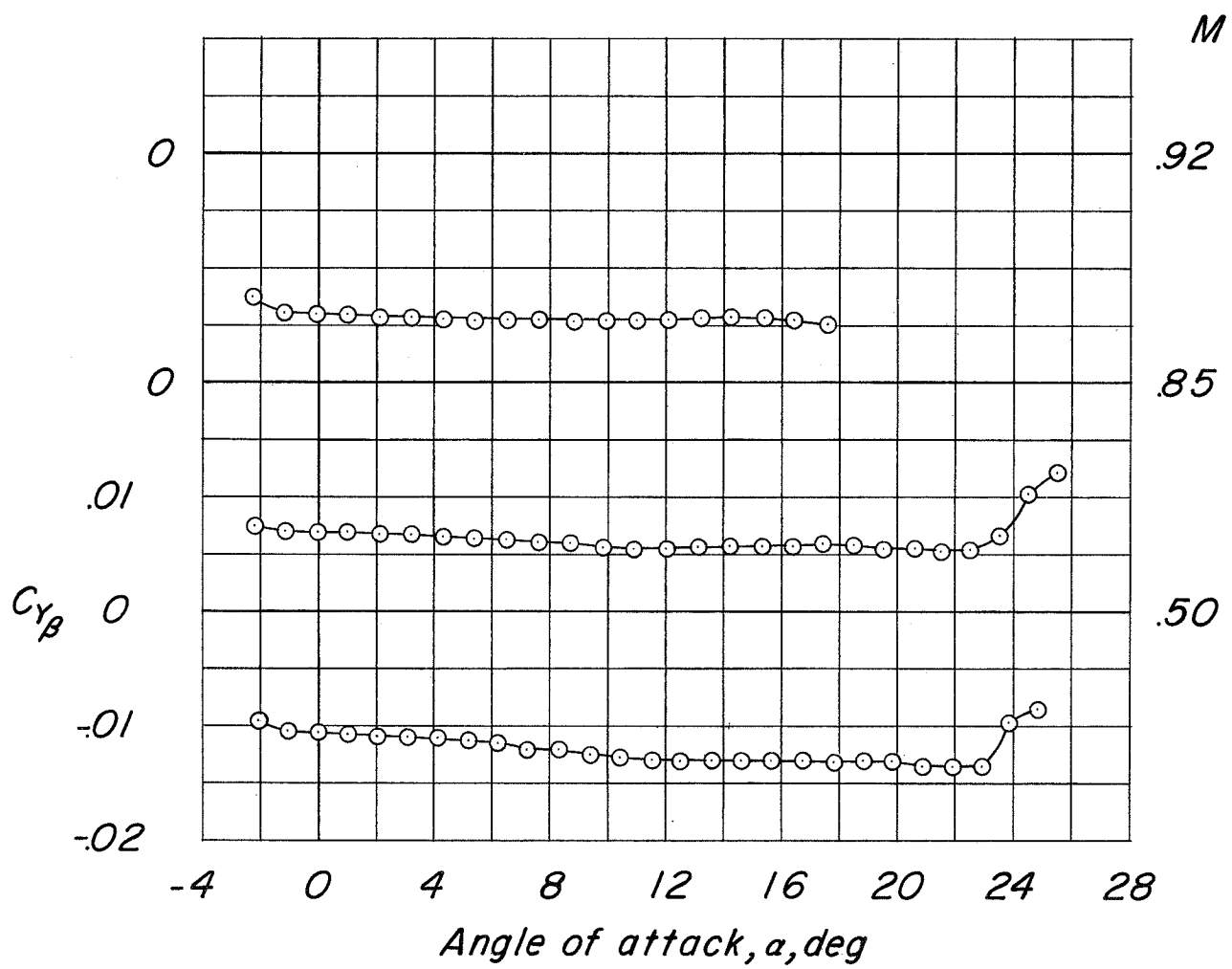
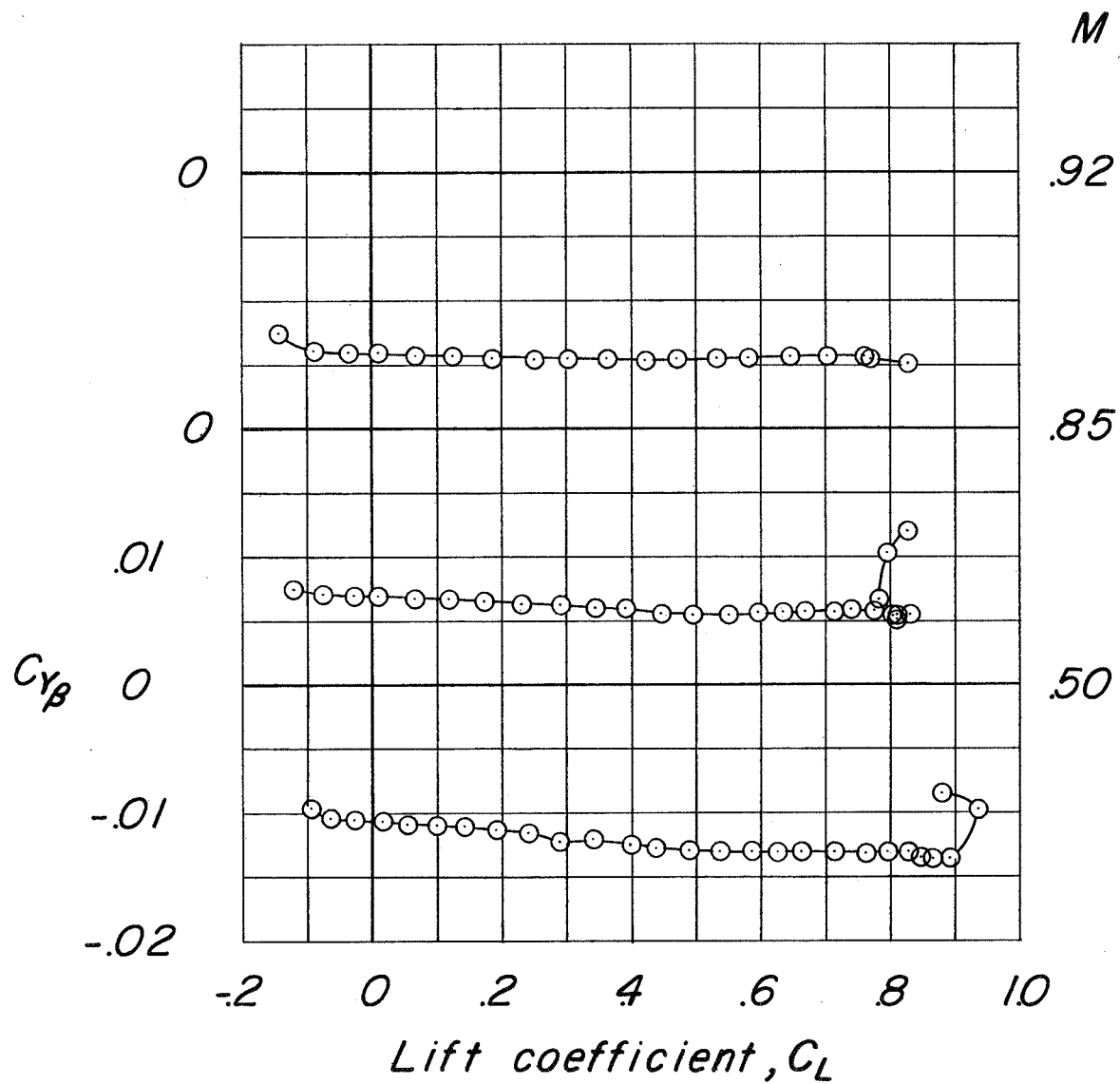
(e) $C_{L\beta}$ against α .

Figure 19.- Continued.



(f) $C_{Y\beta}$ against C_L .

Figure 19.- Concluded.

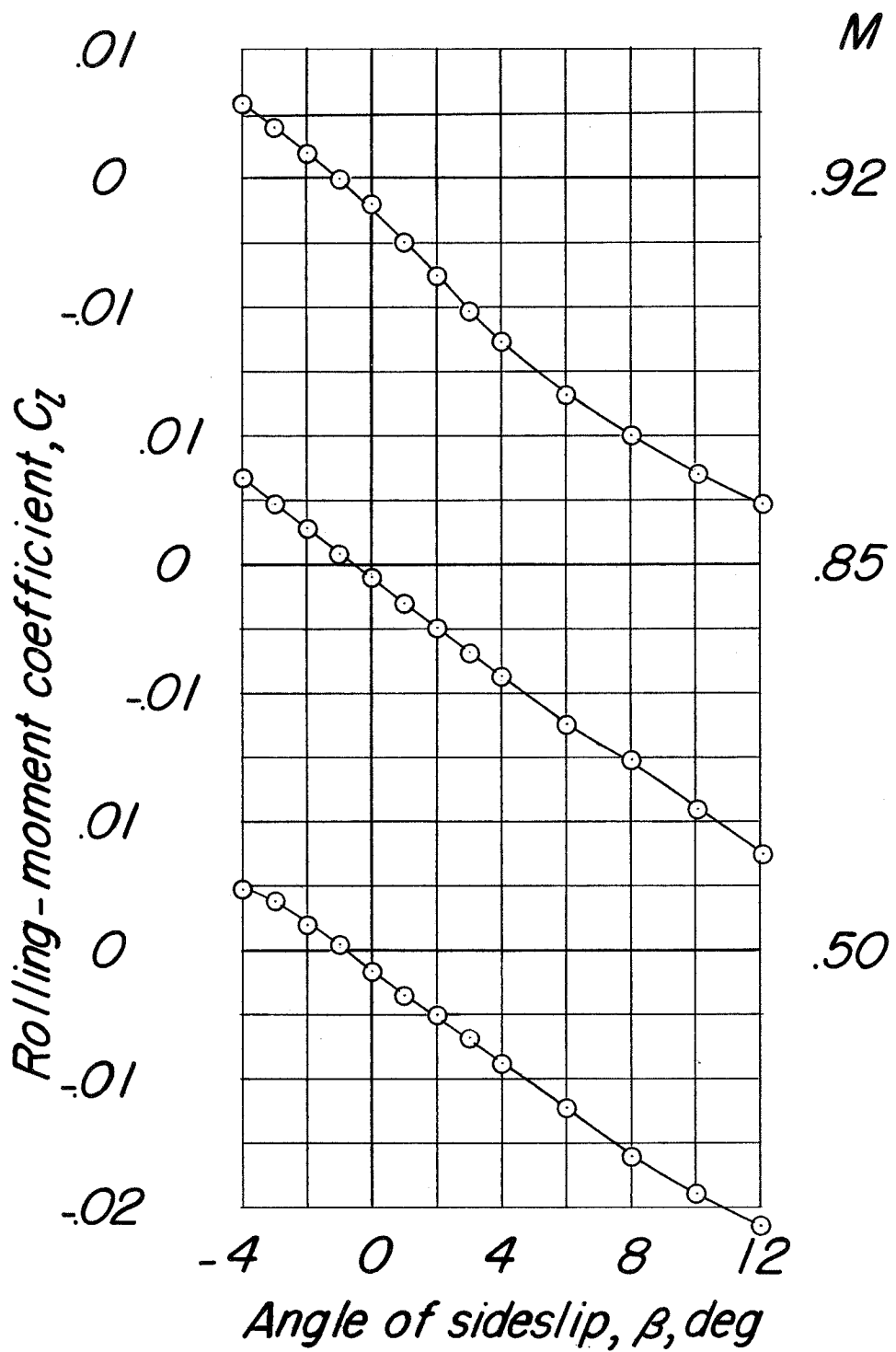
(a) C_l against β .

Figure 20.- Variation of lateral coefficients with angle of sideslip for configuration BCW_{F1+RPV}, $\delta_e = 0^\circ$, $\delta_r = 0^\circ$. $\alpha = 12^\circ$.

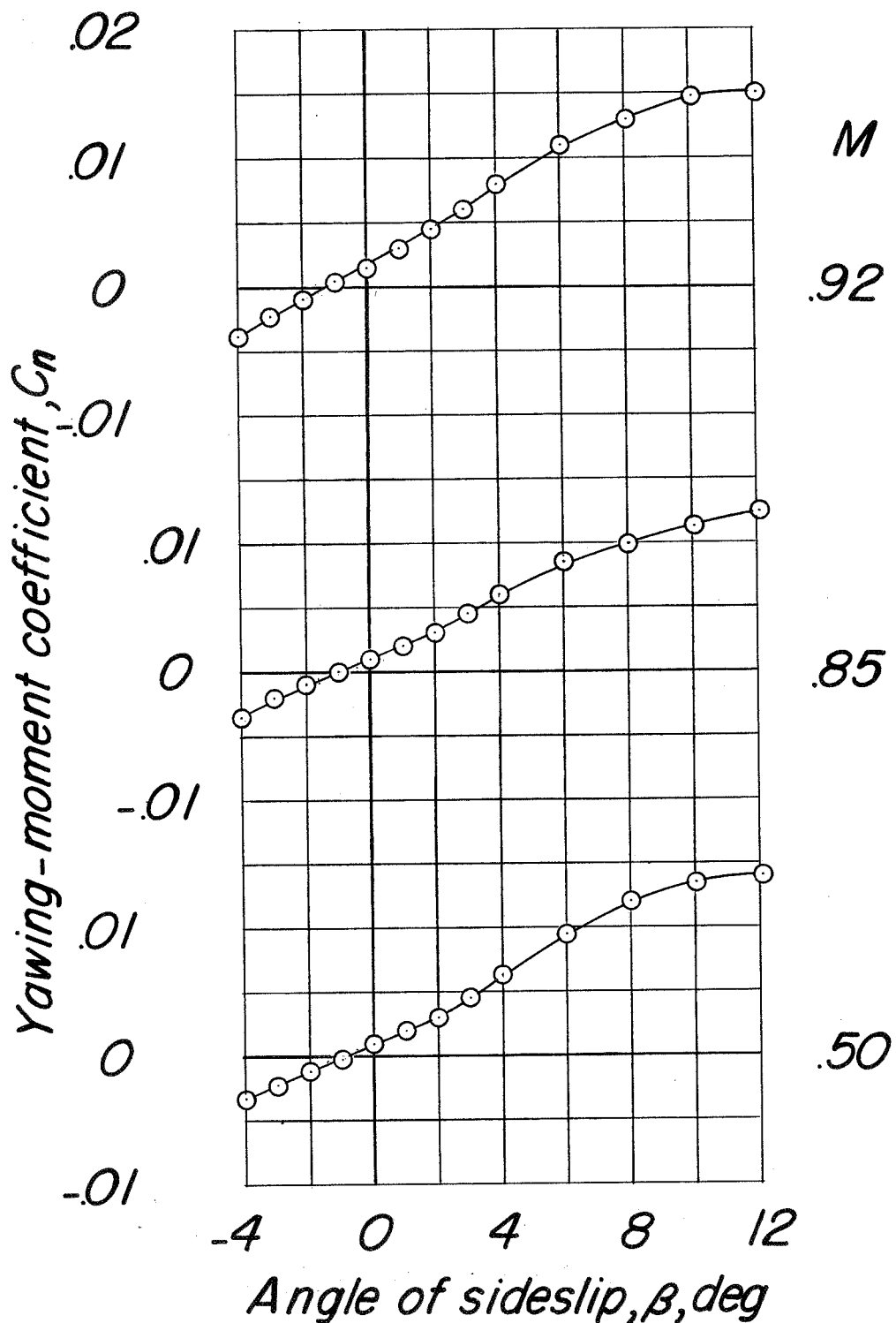
(b) C_n against β .

Figure 20.- Continued.

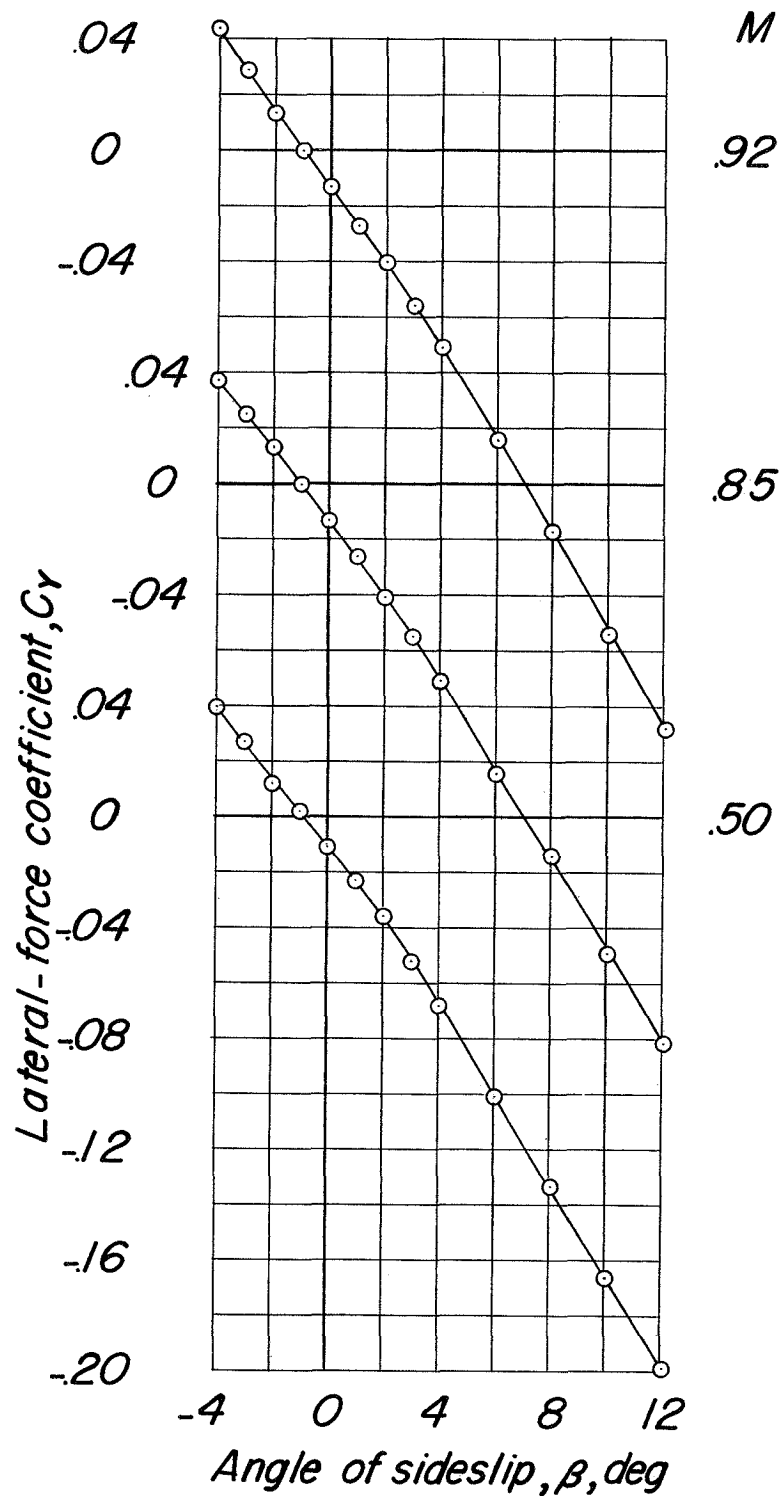
(c) C_Y against β .

Figure 20..- Concluded.

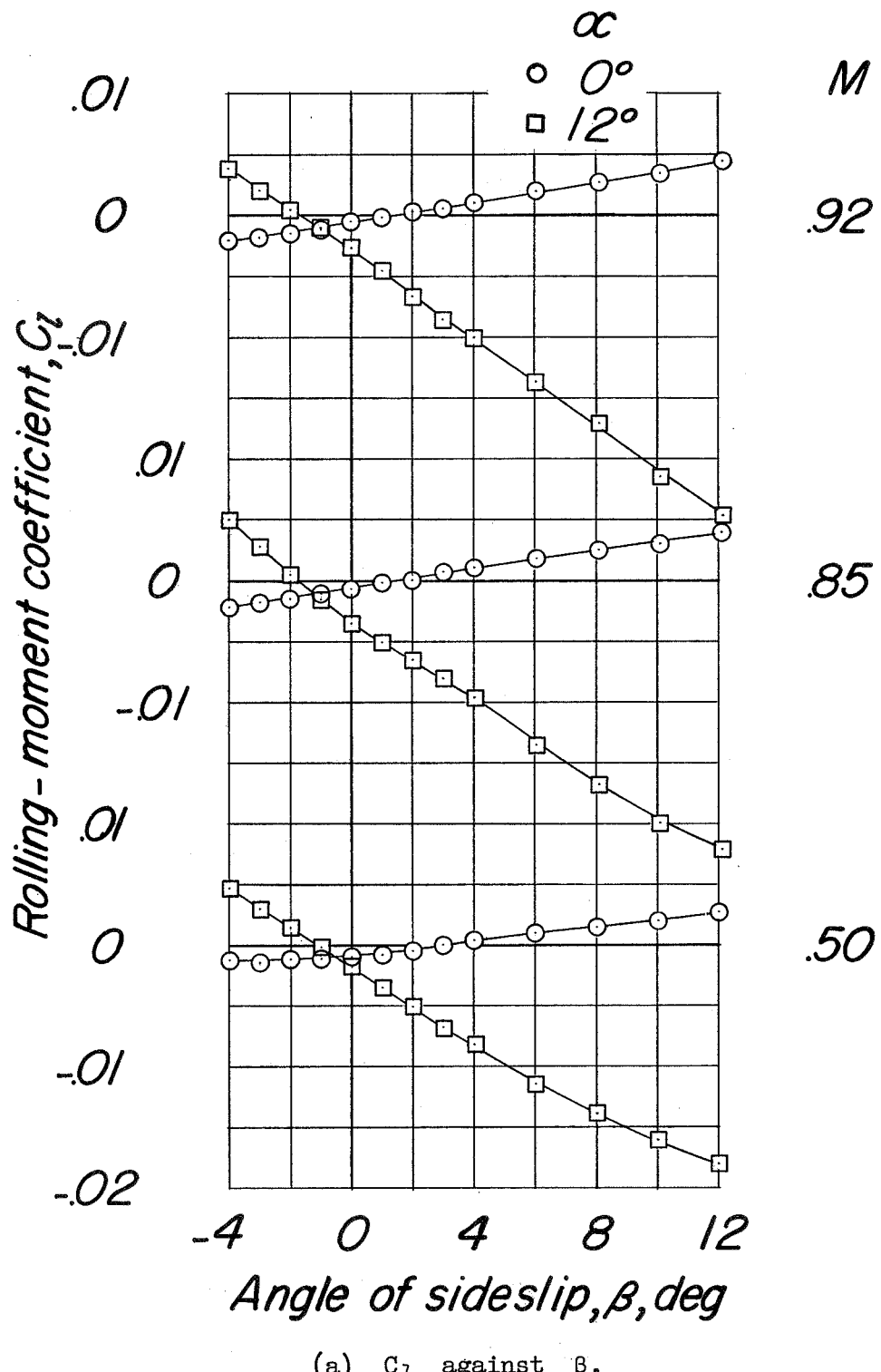
(a) C_l against β .

Figure 21.- Variation of lateral coefficients with angle of sideslip for configuration BCWF₁, $\delta_e = 0^\circ$.

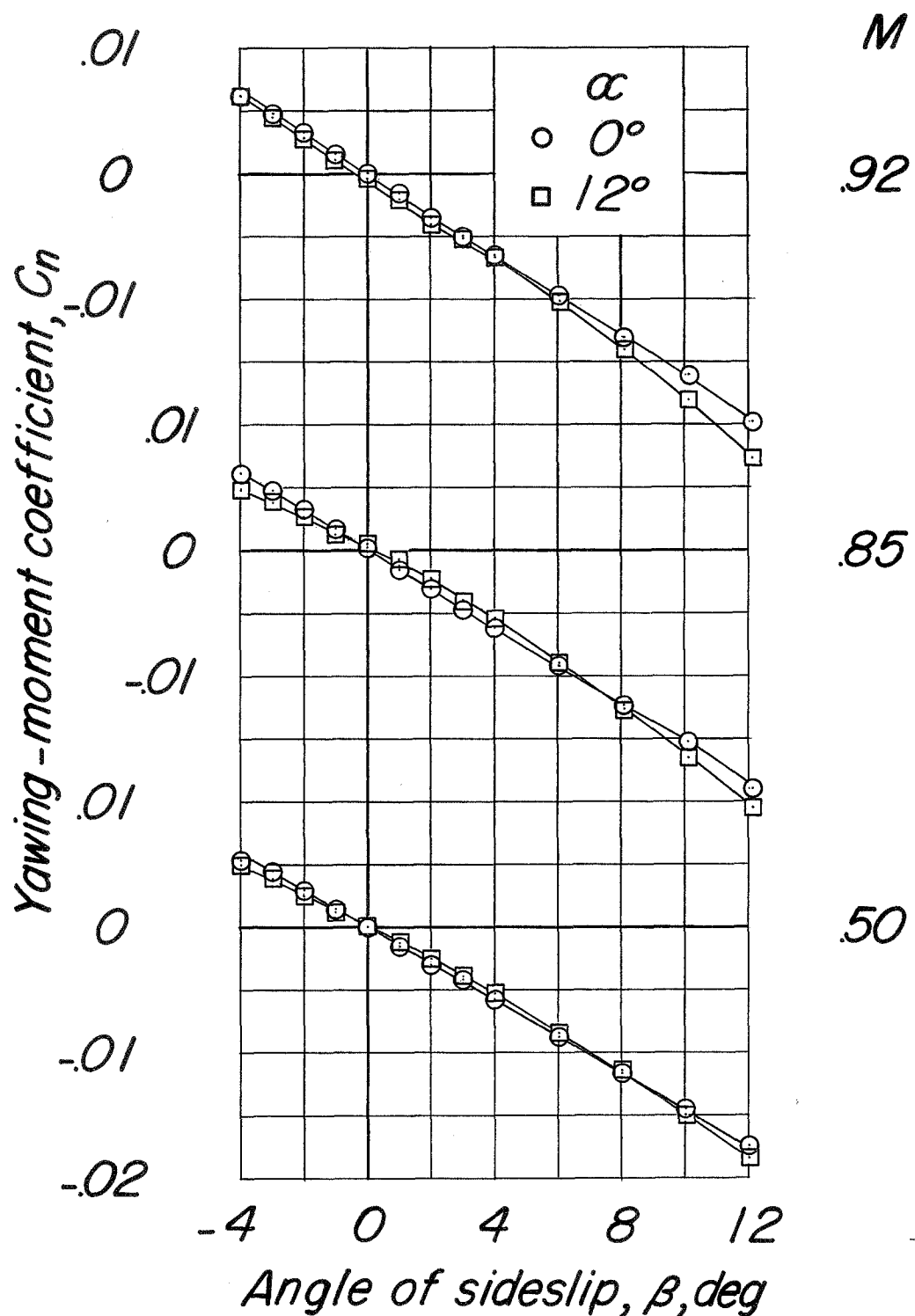
(b) C_n against β .

Figure 21.- Continued.

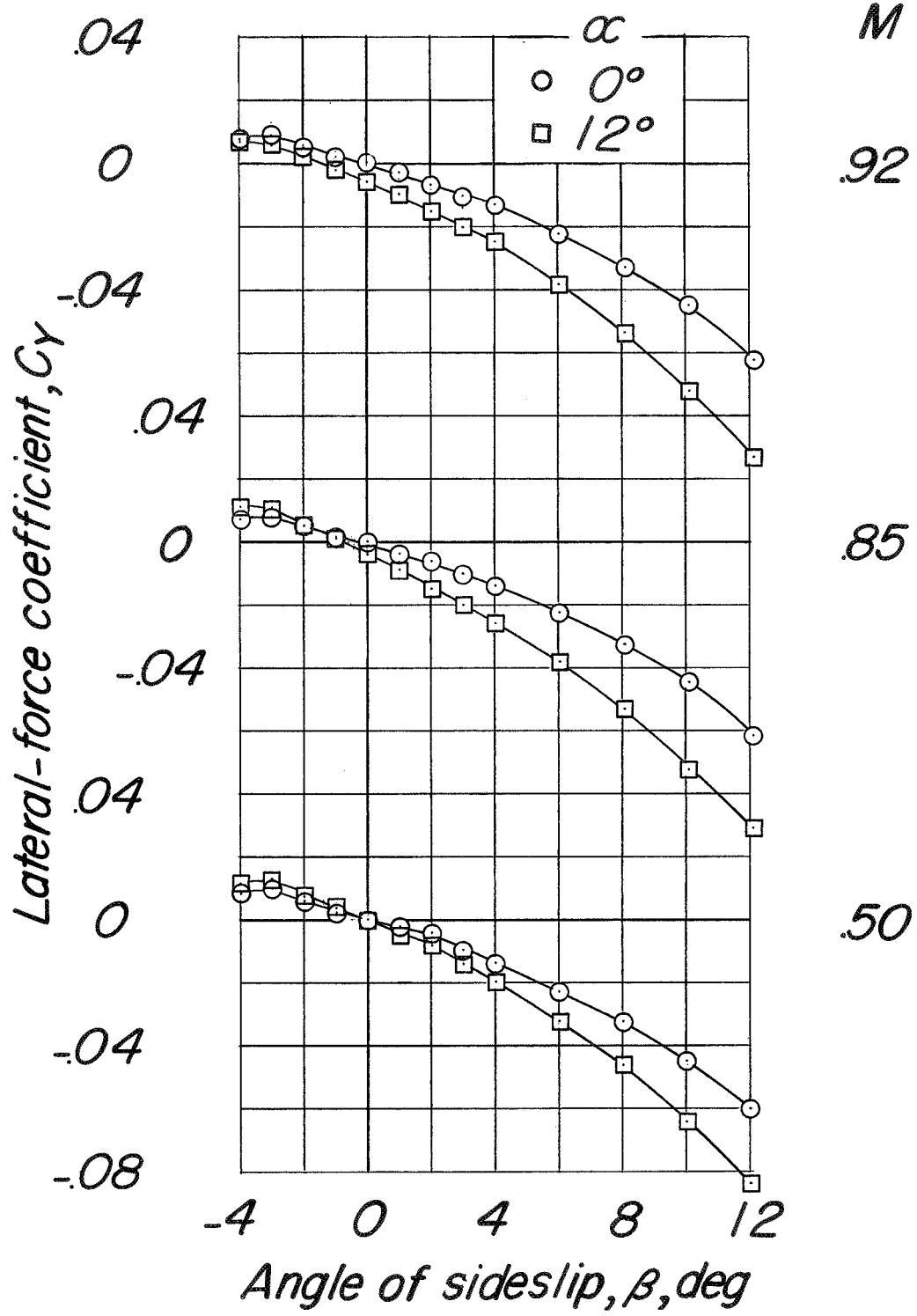
(c) C_y against β .

Figure 21.- Concluded.

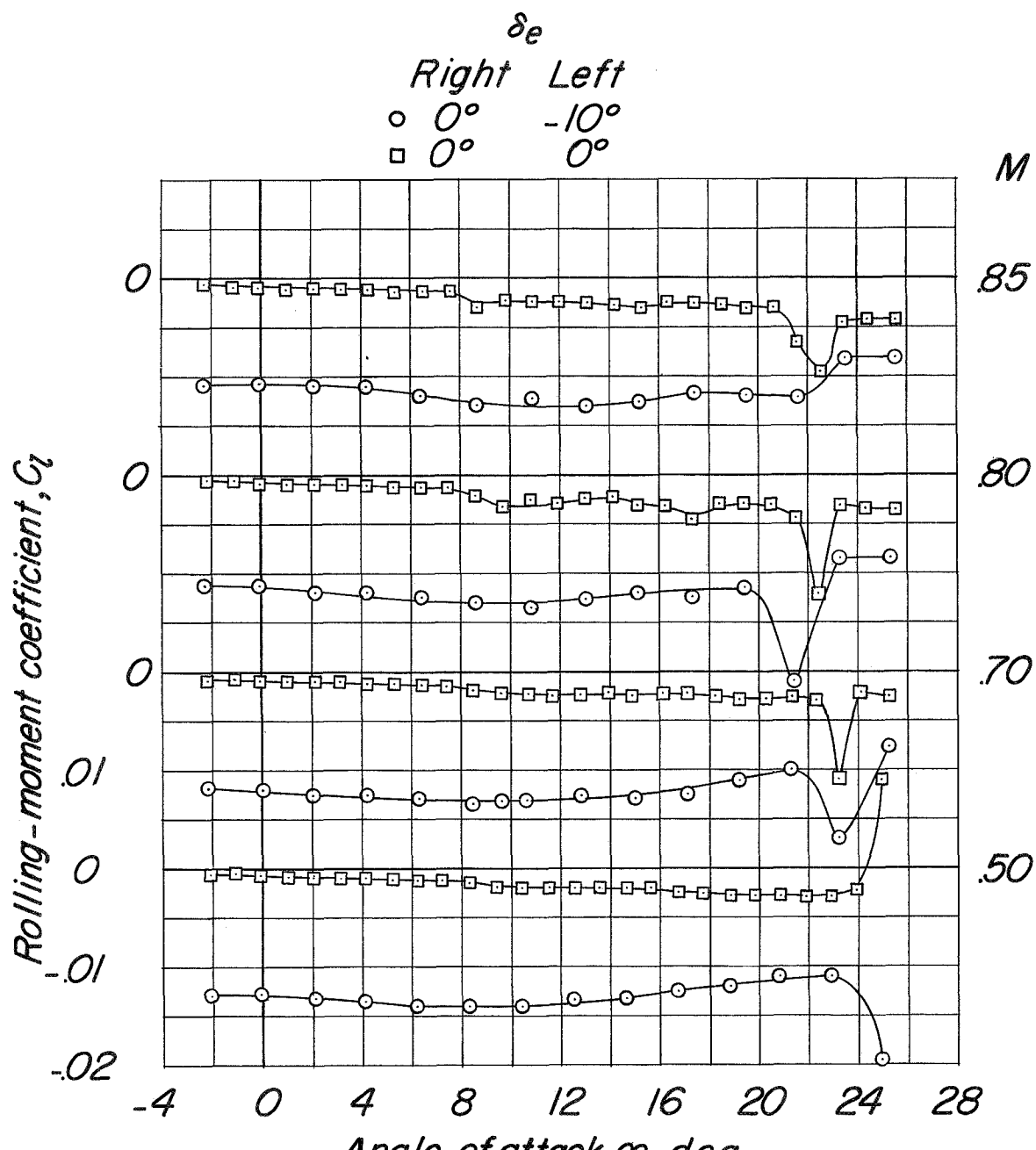
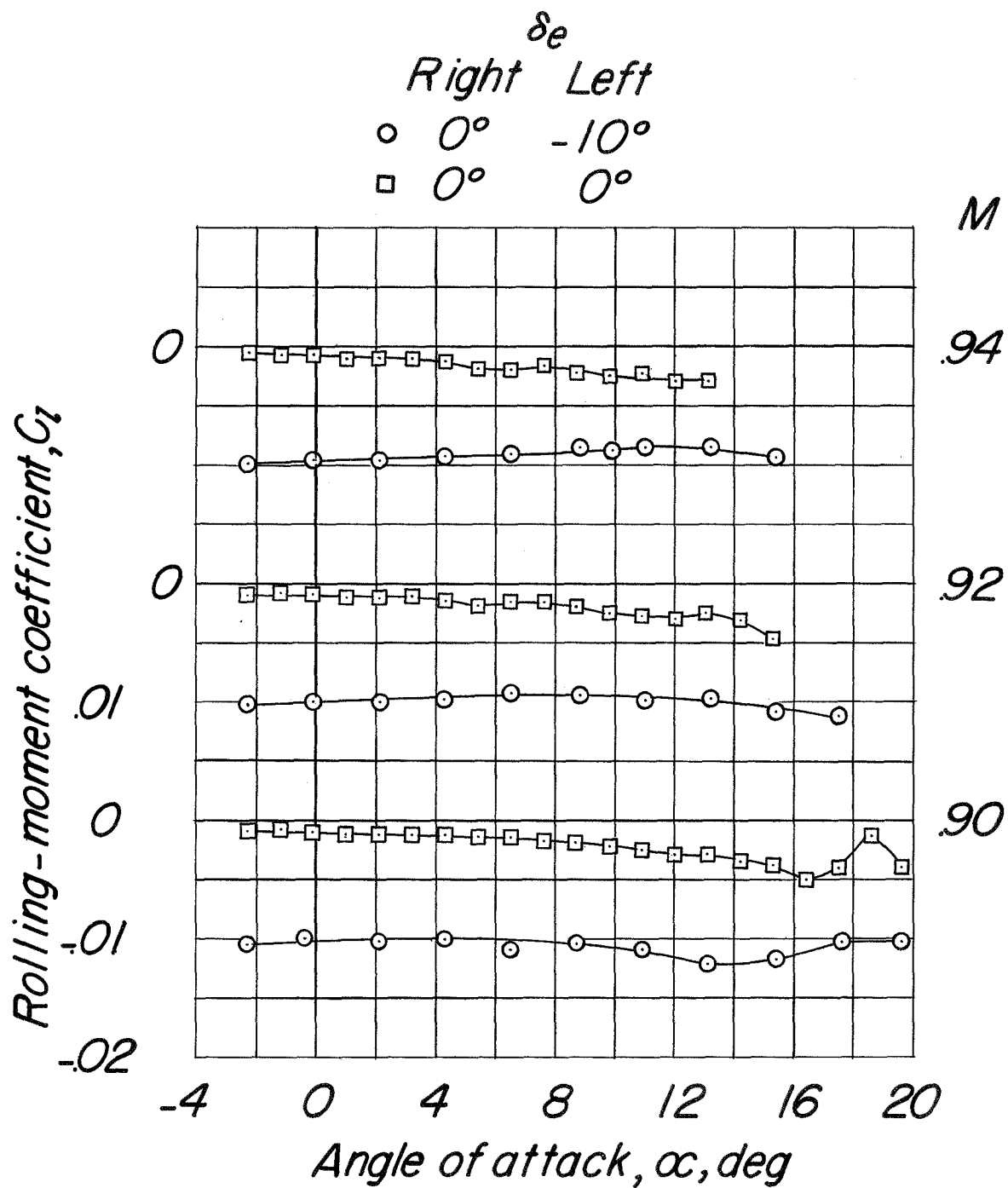
(a) C_l against α .

Figure 22.- Aerodynamic characteristics in pitch to determine lateral control effectiveness for configuration $BCWF_1V$, $\delta_r = 0^\circ$.



(a) Concluded.

Figure 22.- Continued.

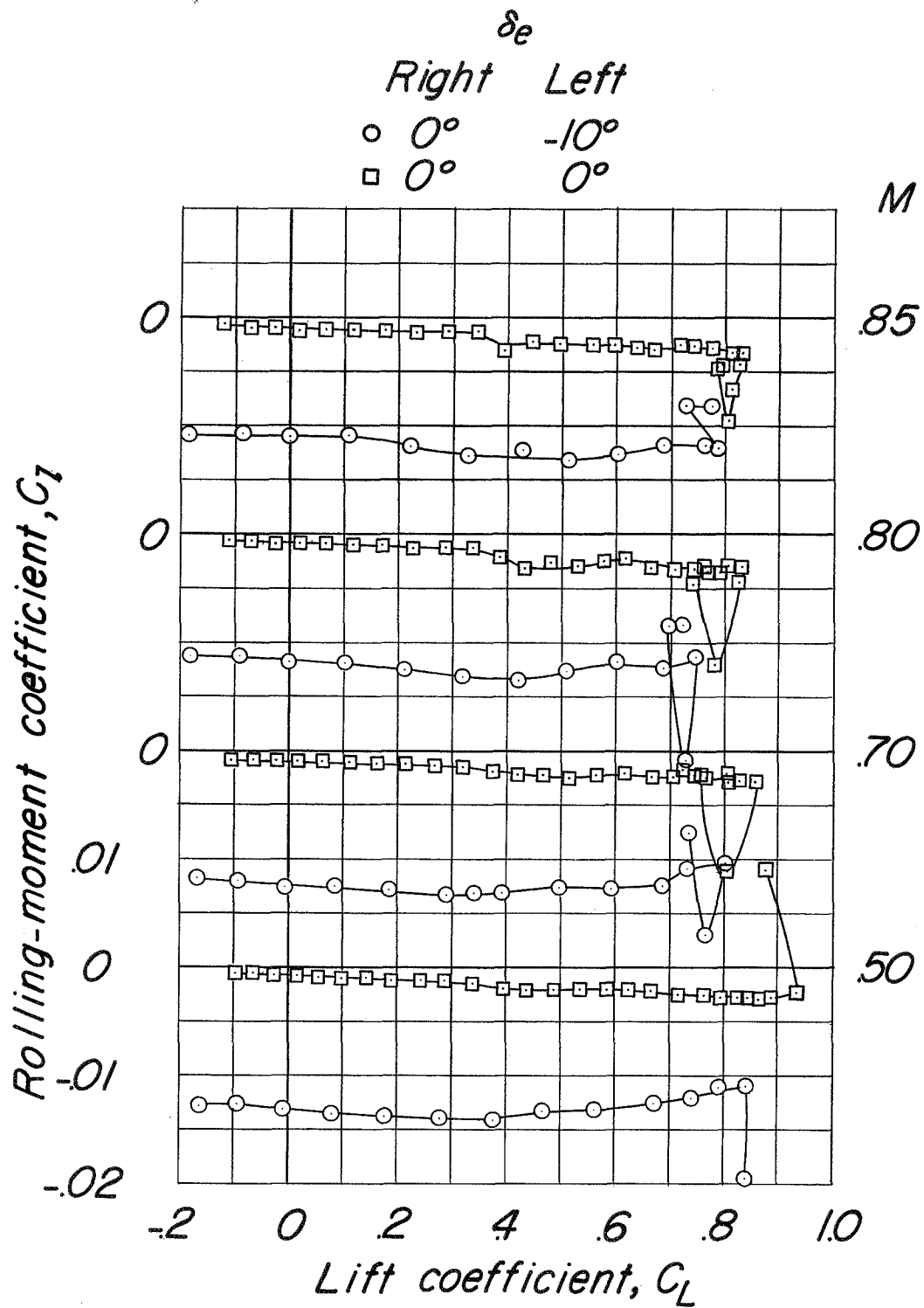
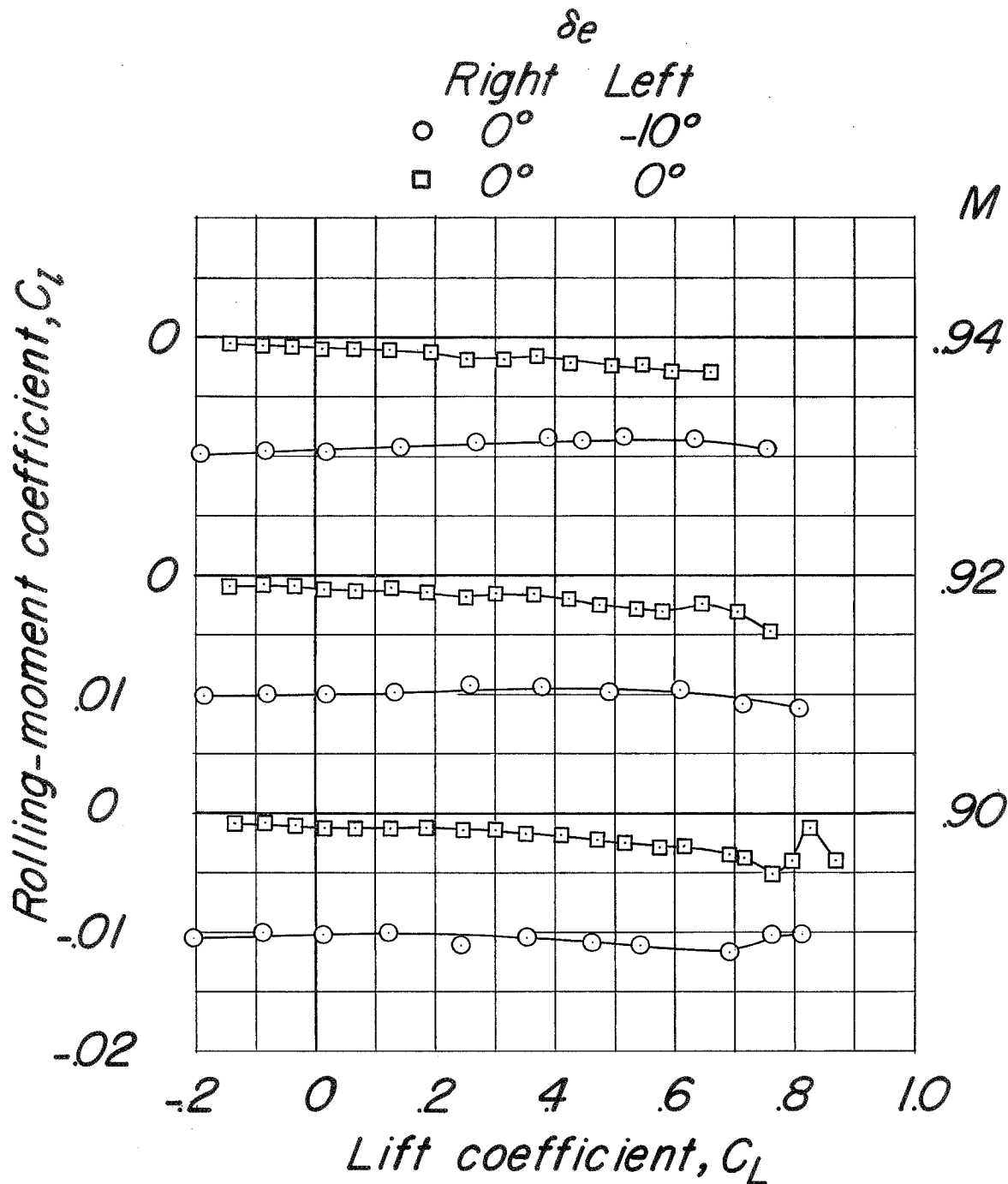
(b) C_l against C_L .

Figure 22.- Continued.



(b) Concluded.

Figure 22.- Continued.

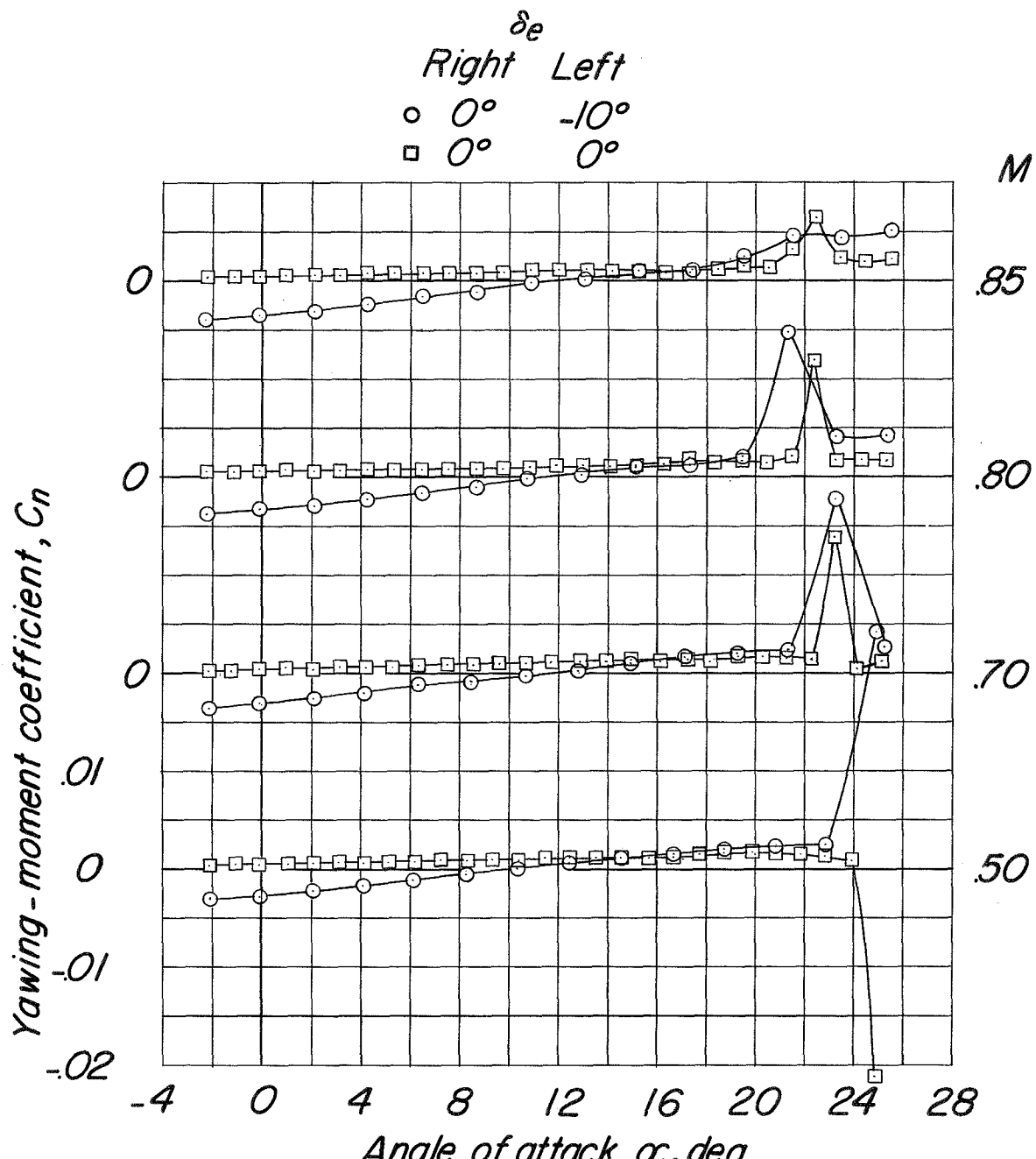
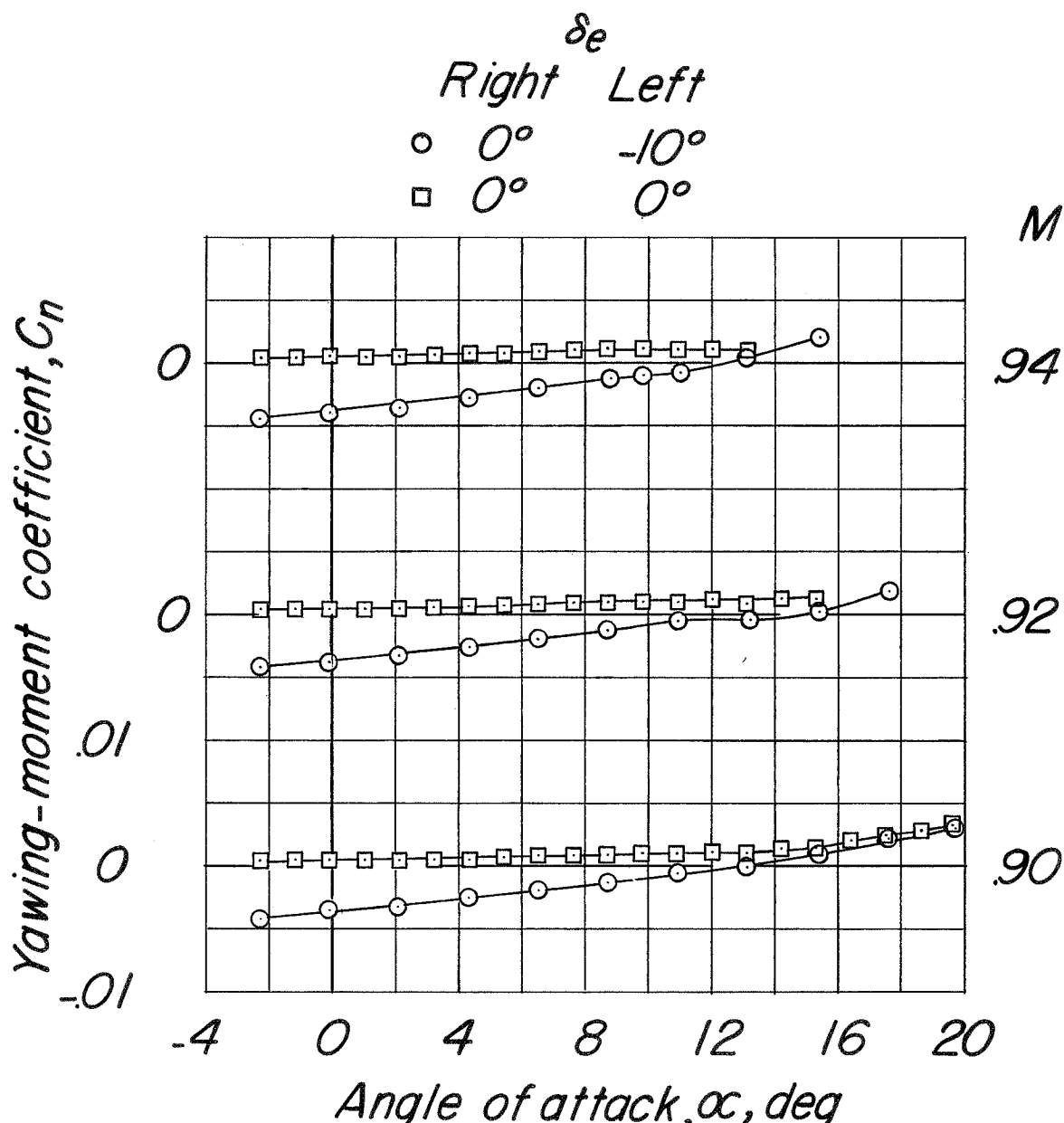
(c) C_n against α .

Figure 22.- Continued.



(c) Concluded.

Figure 22.- Continued.

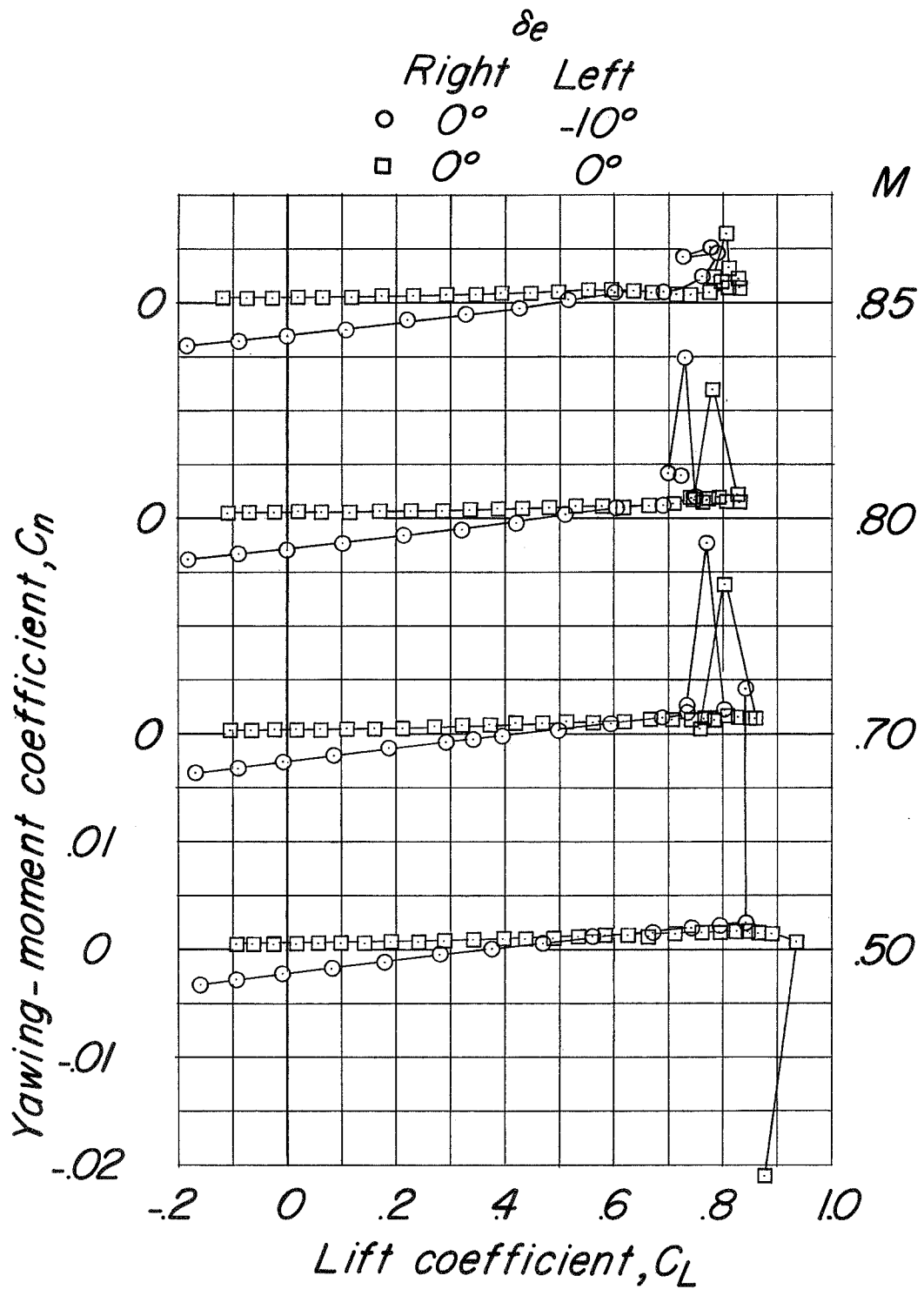
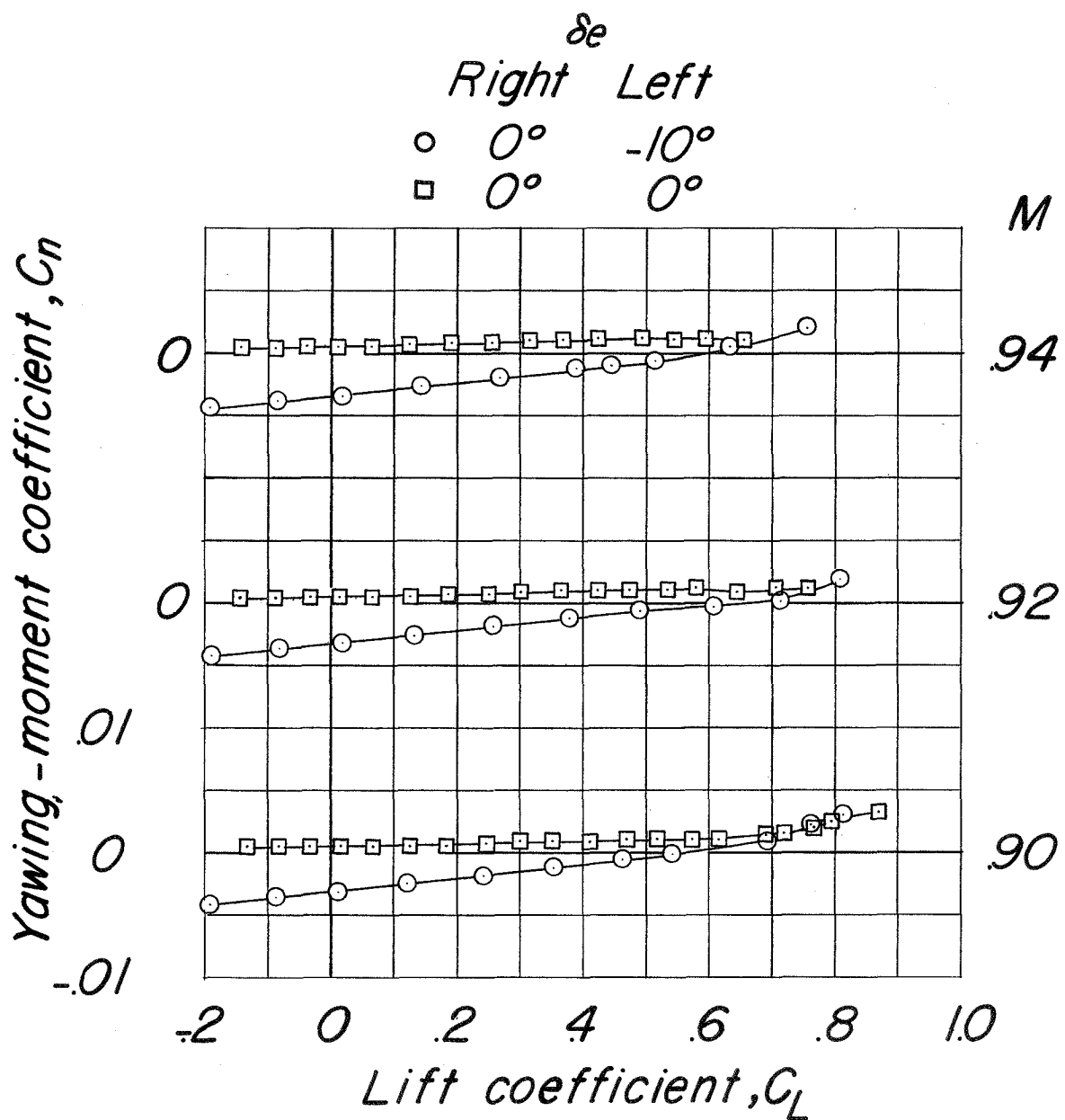
(d) C_n against C_L .

Figure 22.- Continued.



(d) Concluded.

Figure 22.- Continued.

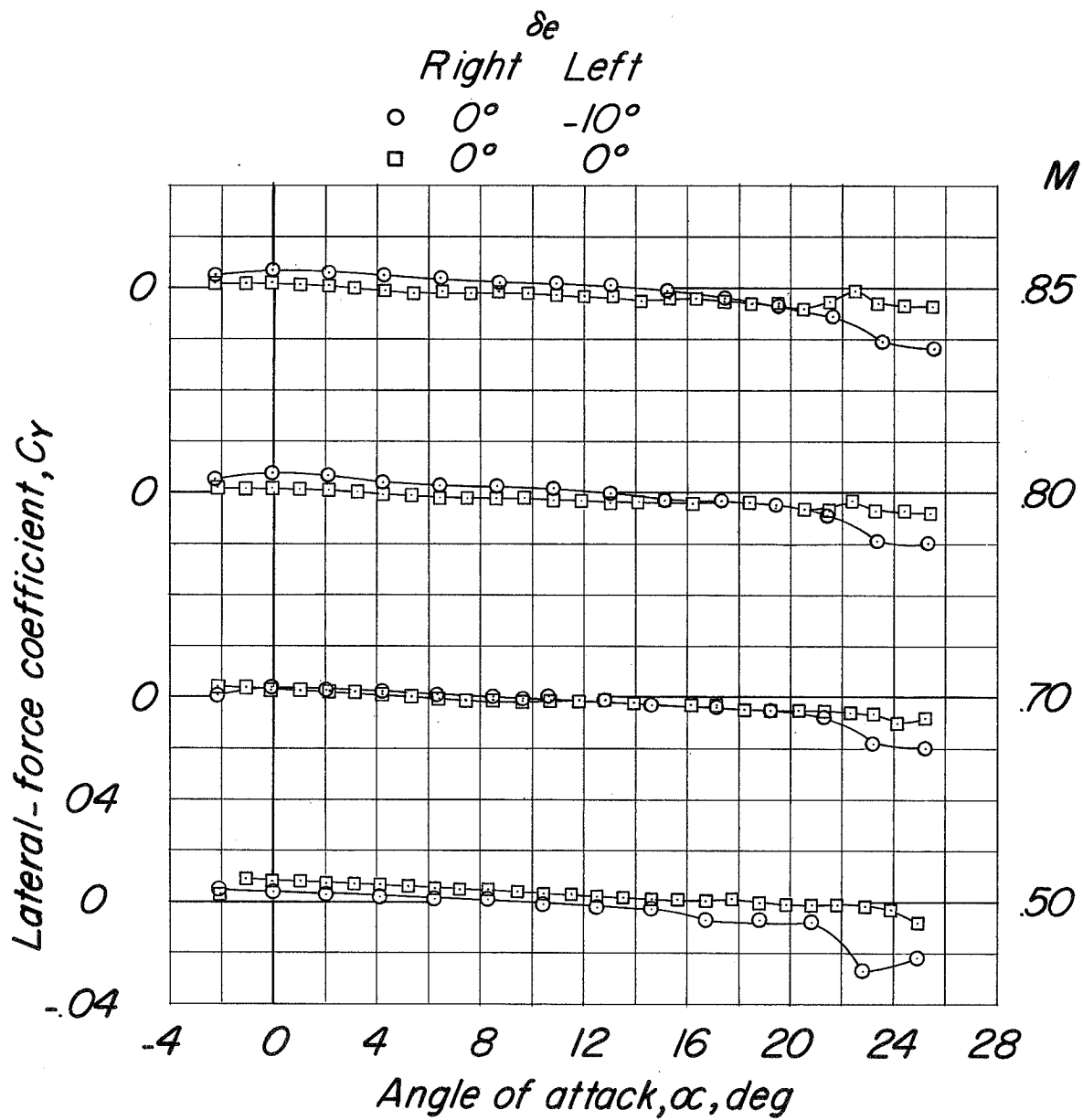
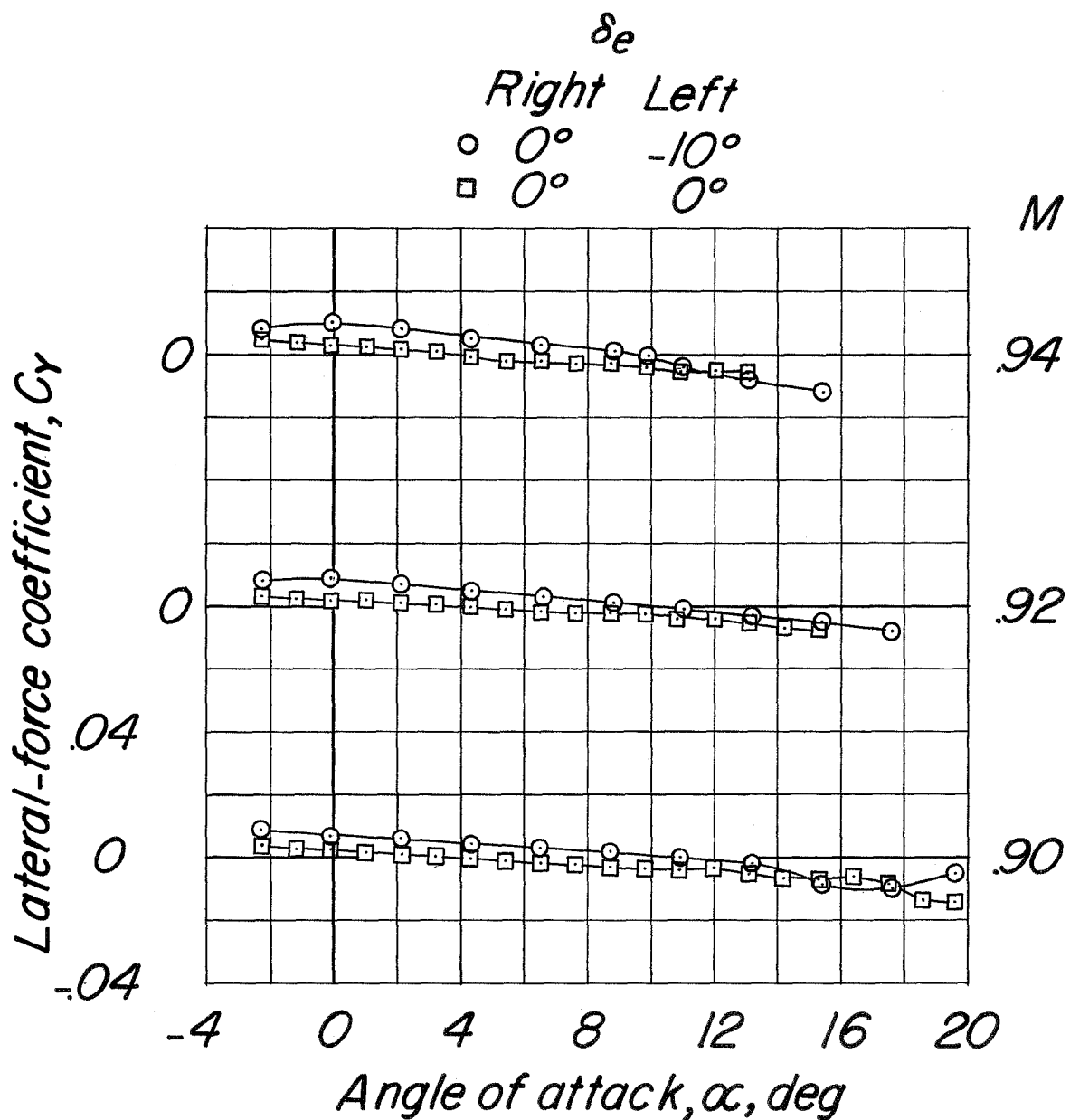
(e) C_Y against α .

Figure 22.-- Continued.



(e) Concluded.

Figure 22.- Continued.

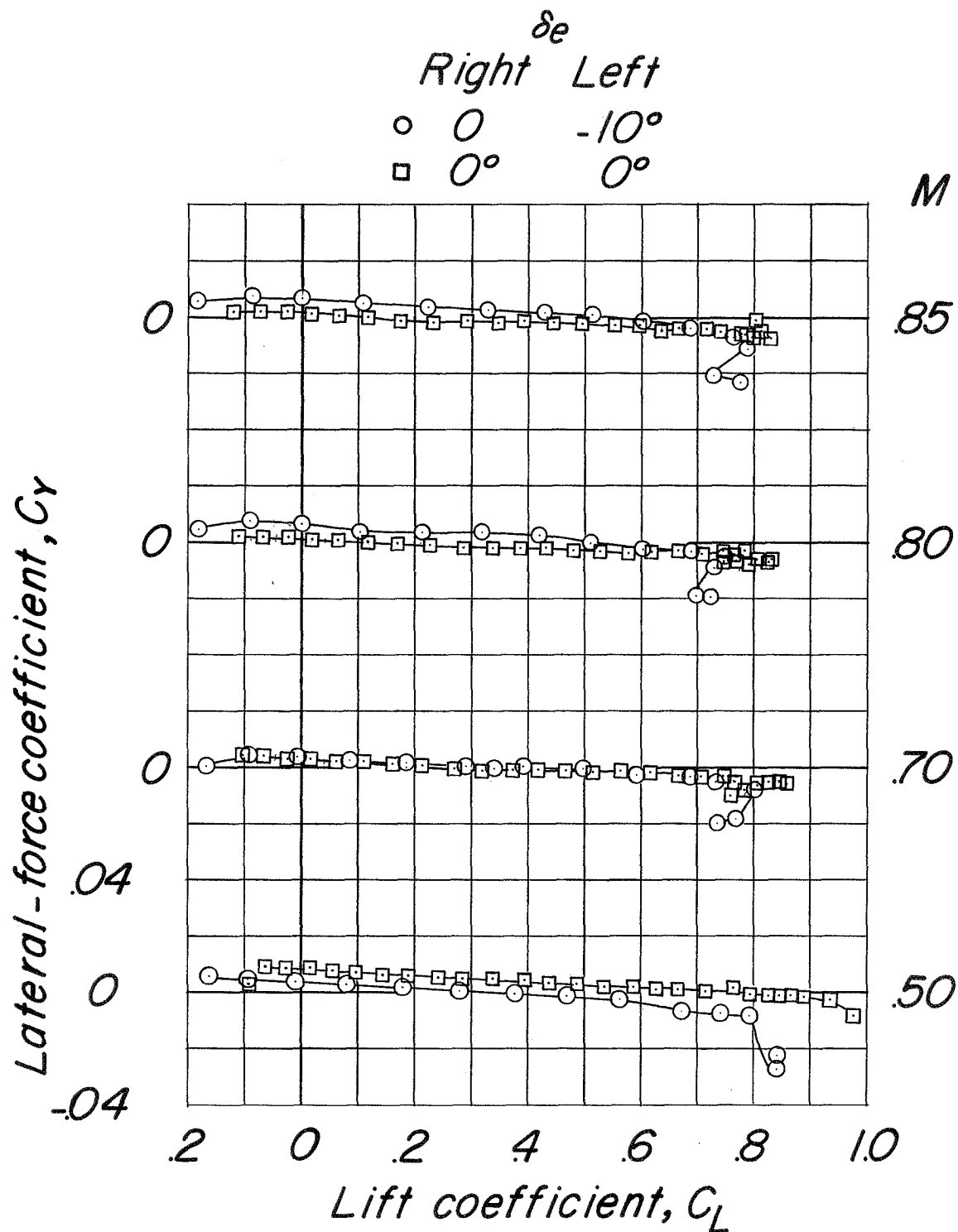
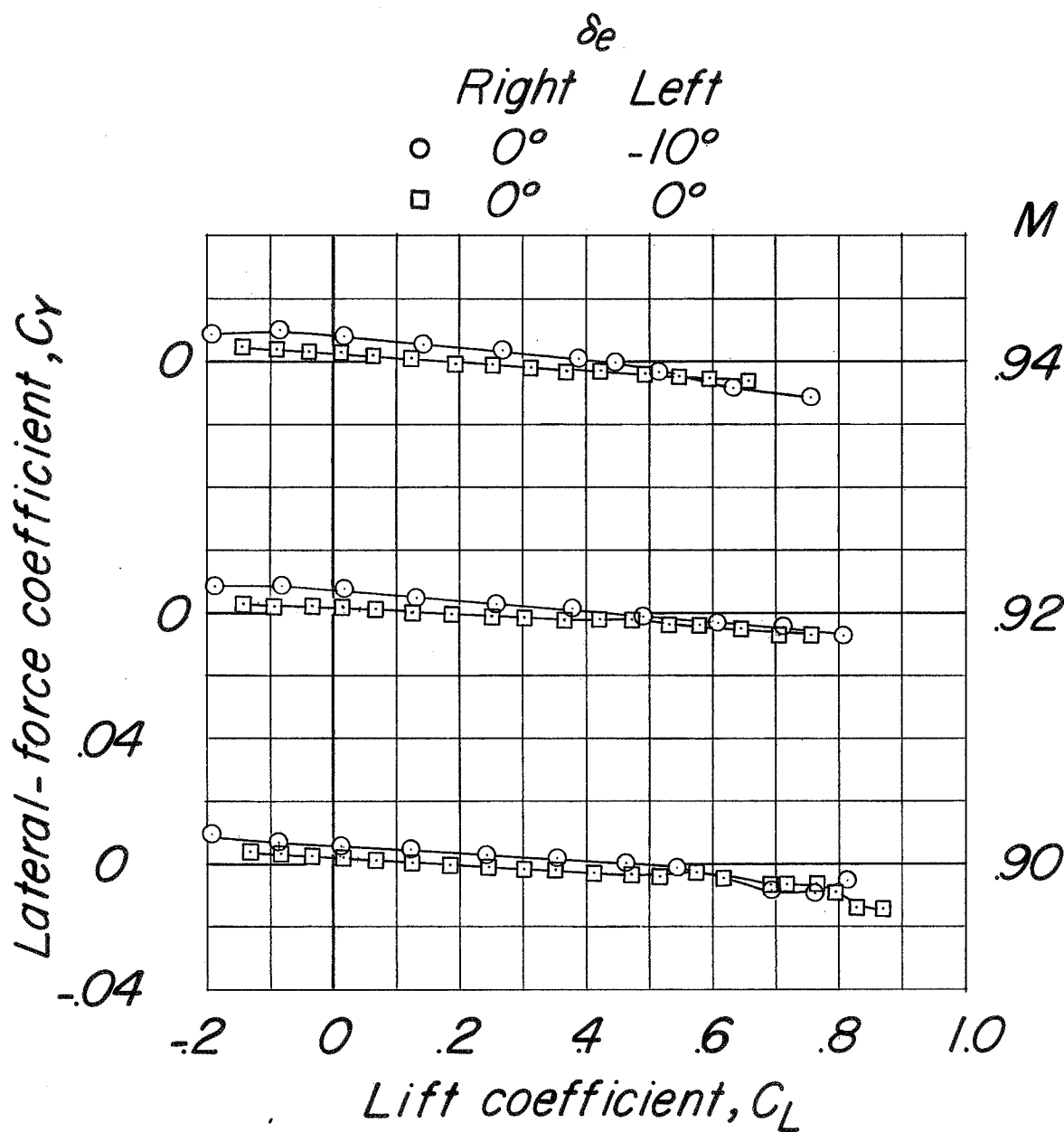
(f) C_Y against C_L .

Figure 22.- Continued.



(f) Concluded.

Figure 22.- Concluded.

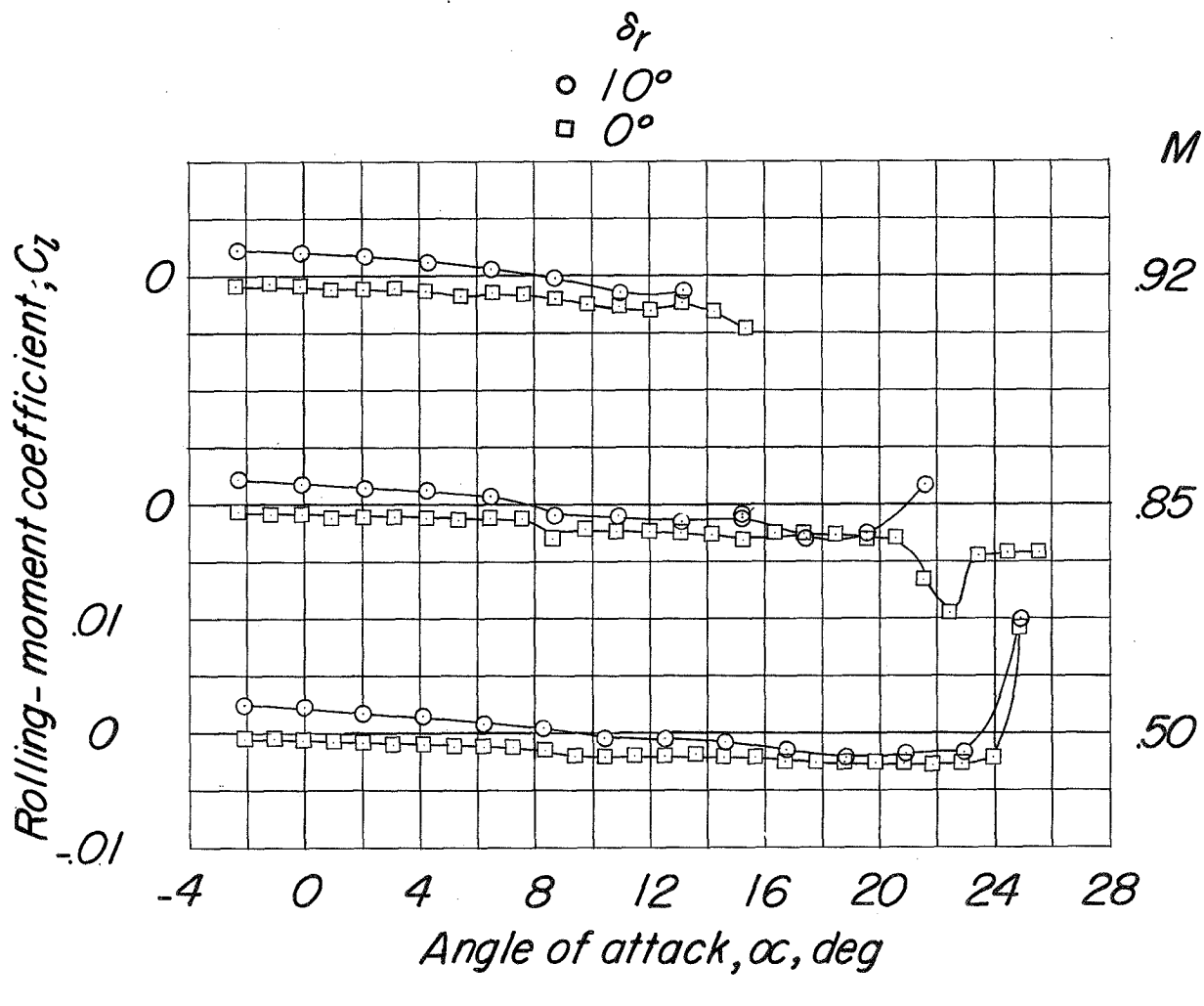
(a) C_l against α .

Figure 23.- Aerodynamic characteristics in pitch to determine directional control effectiveness for configuration BCW_{F₁}V, $\delta_e = 0^\circ$.

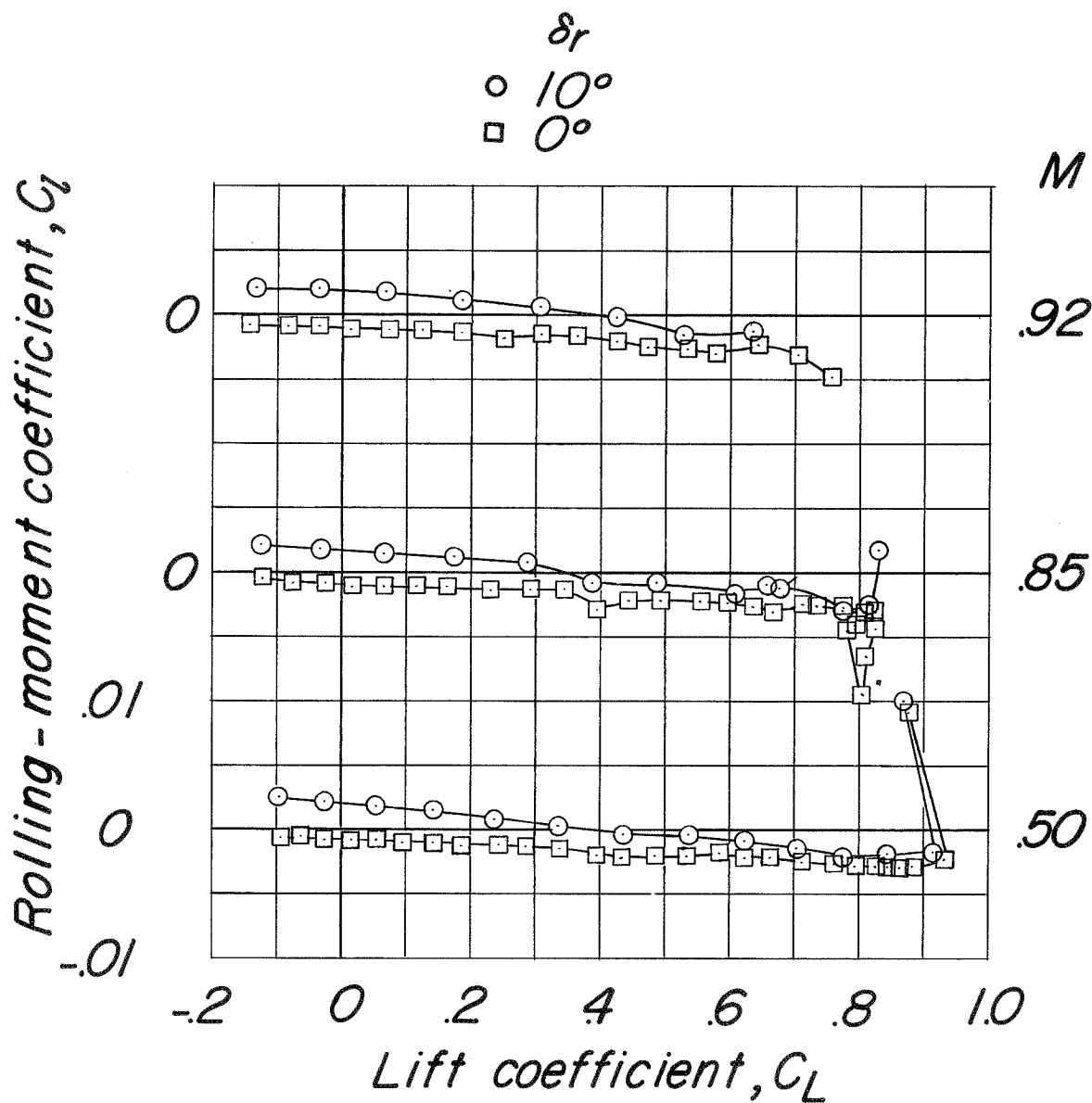
(b) C_l against C_L .

Figure 23.- Continued.

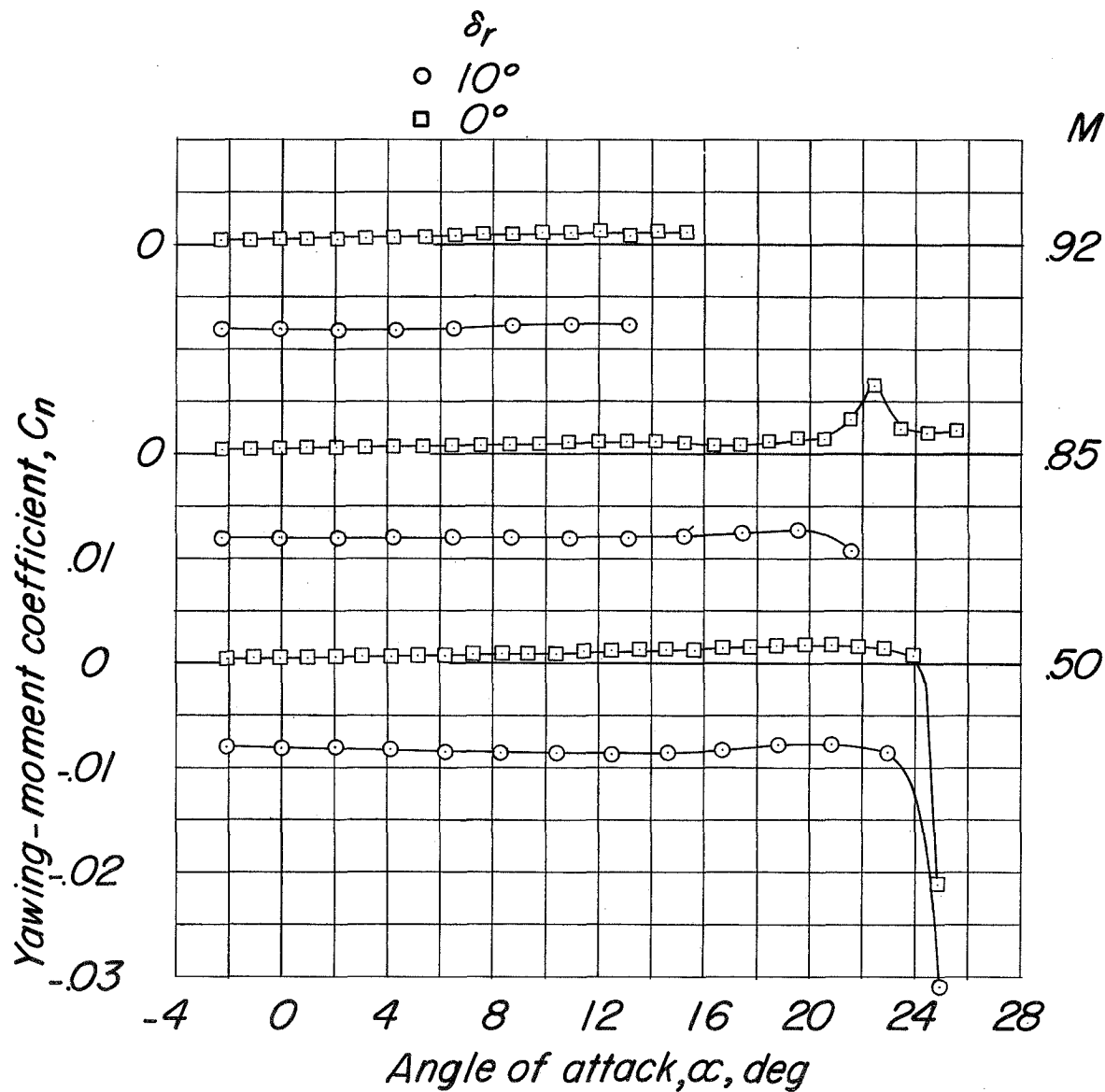
(c) C_n against α .

Figure 23.- Continued.

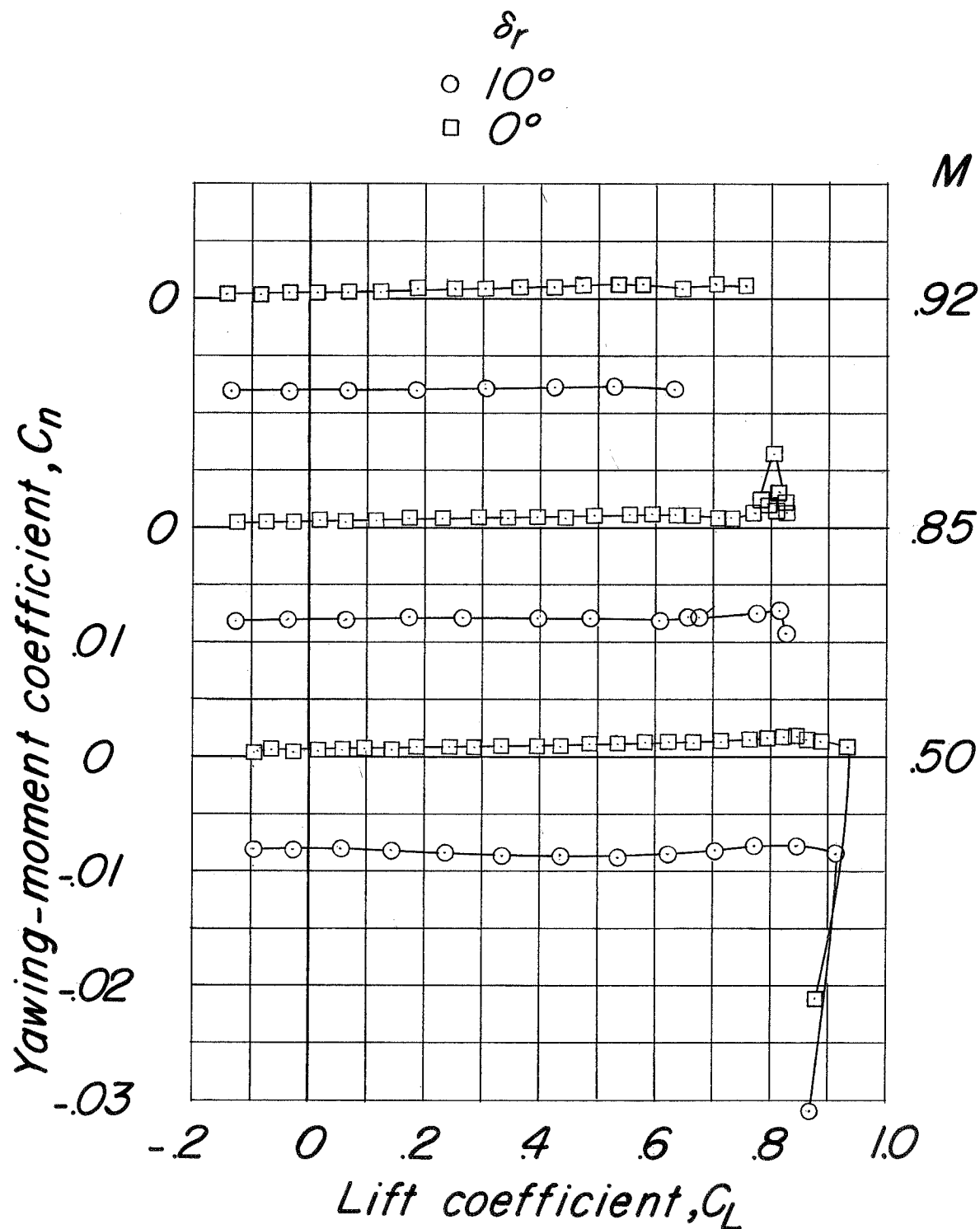
(d) C_n against C_L .

Figure 23.- Continued.

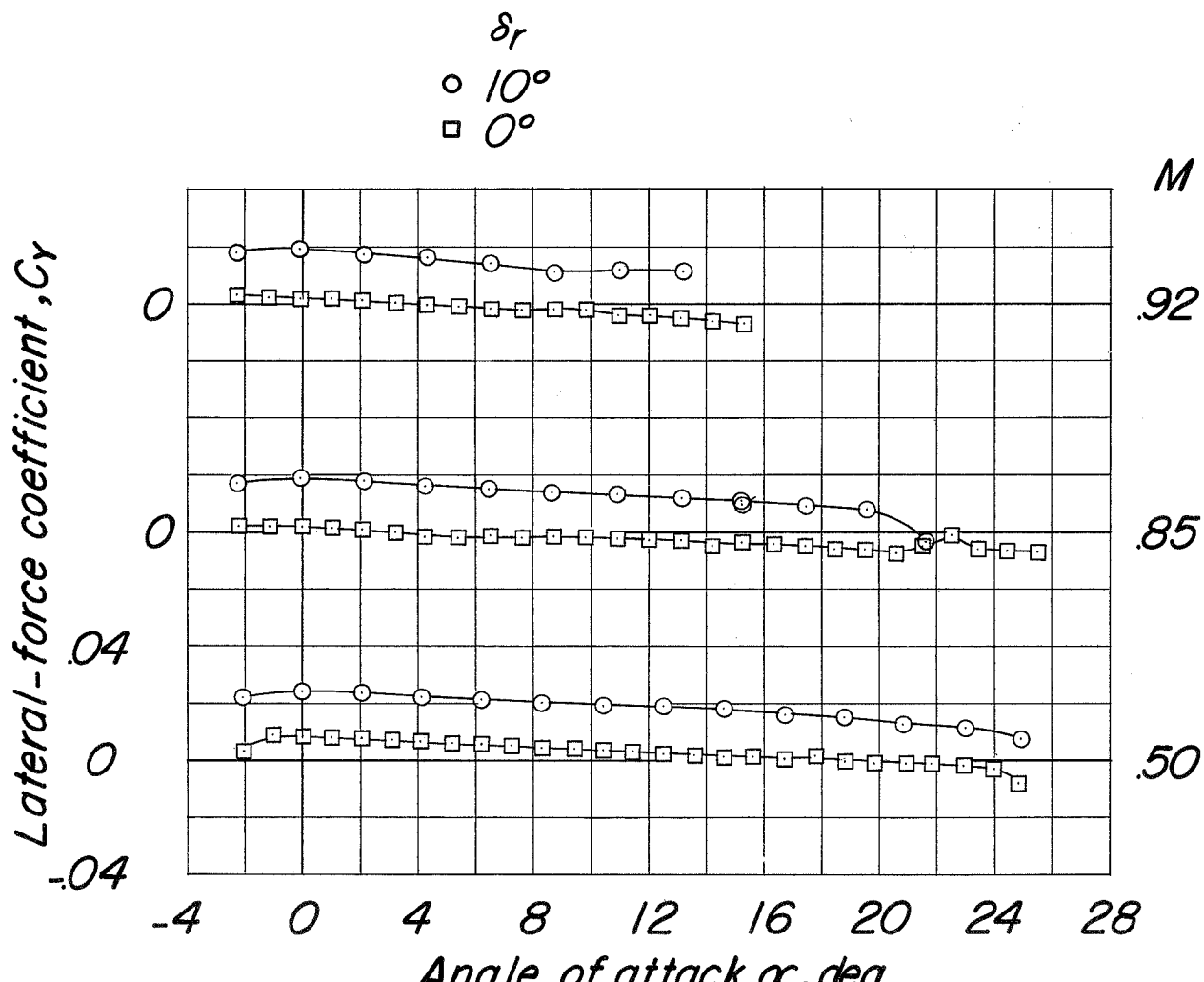
(e) C_Y against α .

Figure 23.- Continued.

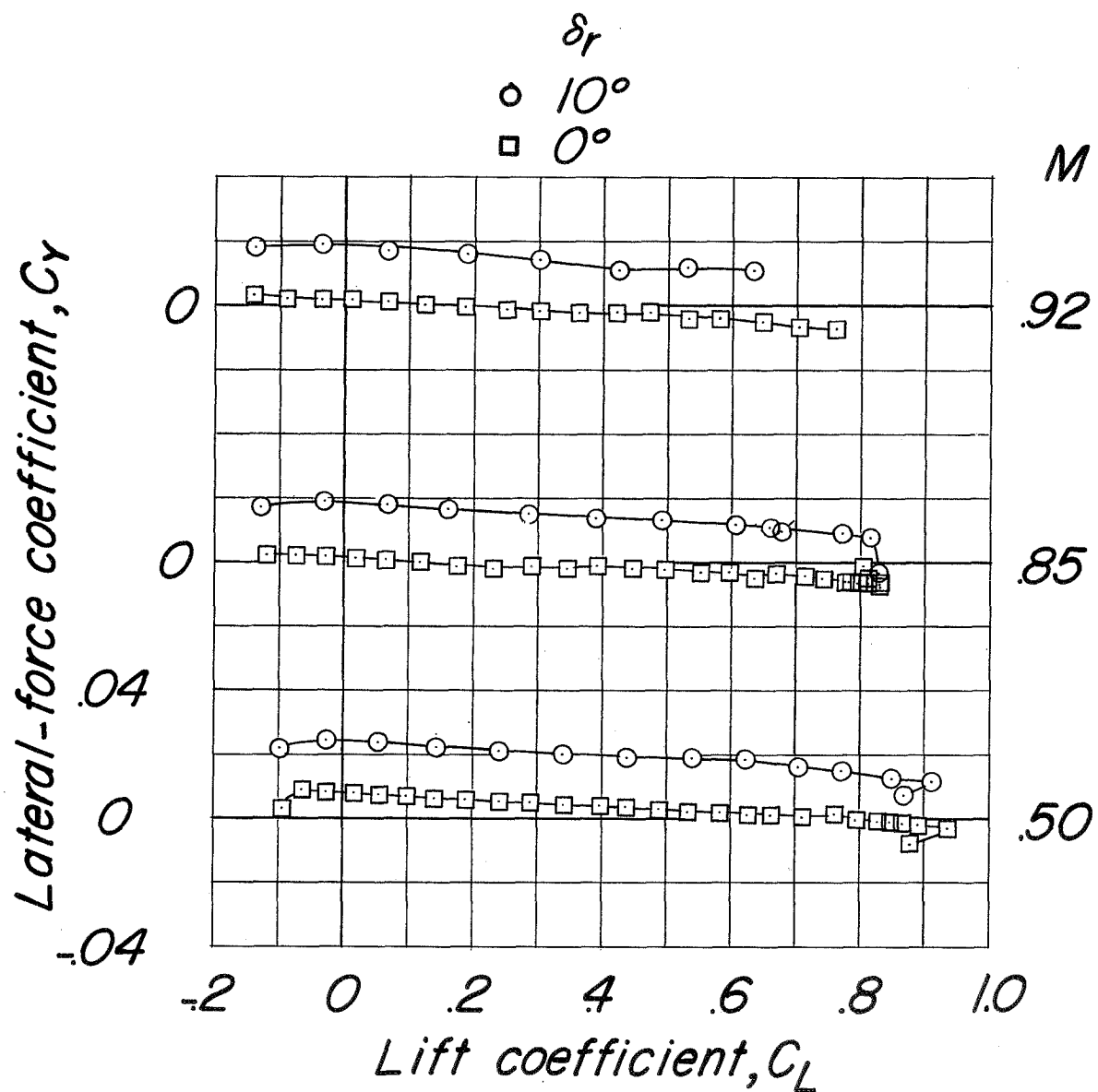
(f) C_Y against C_L .

Figure 23.- Concluded.

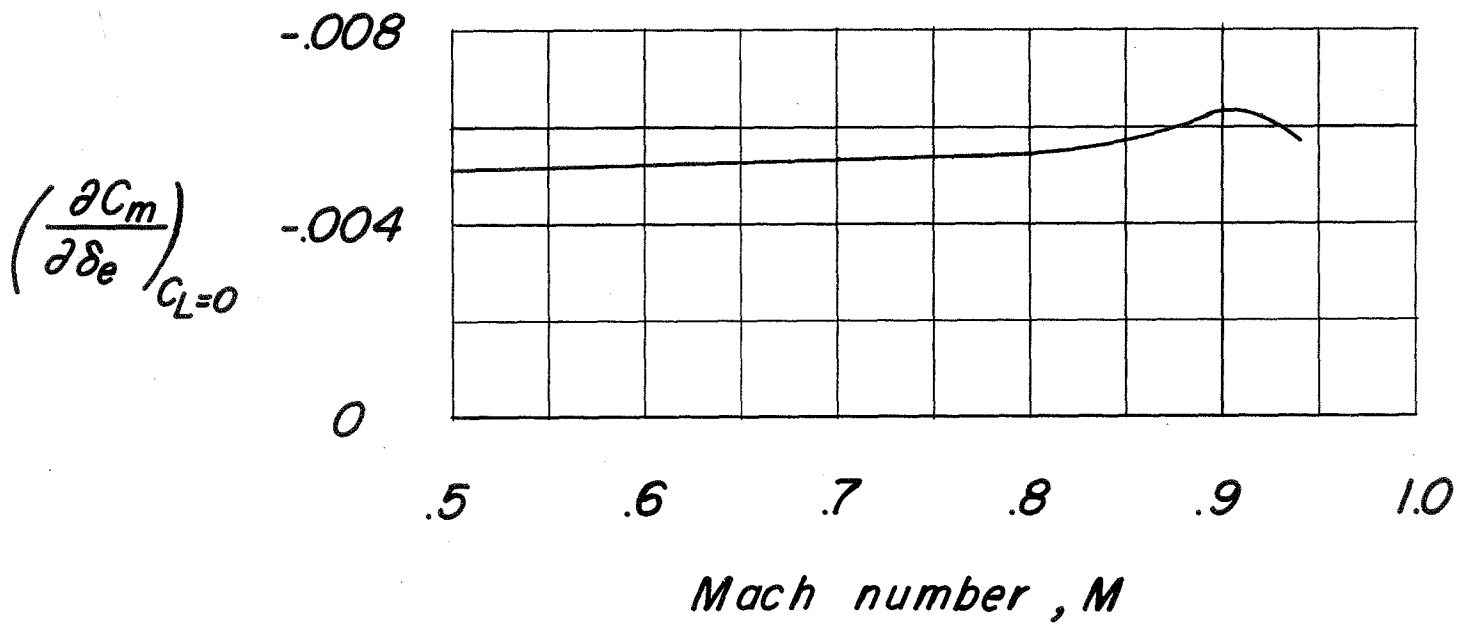


Figure 24.- Elevator effectiveness of configuration BCWF₁V, $\delta_r = 0^\circ$,
center of gravity at 0.30 \bar{c} .

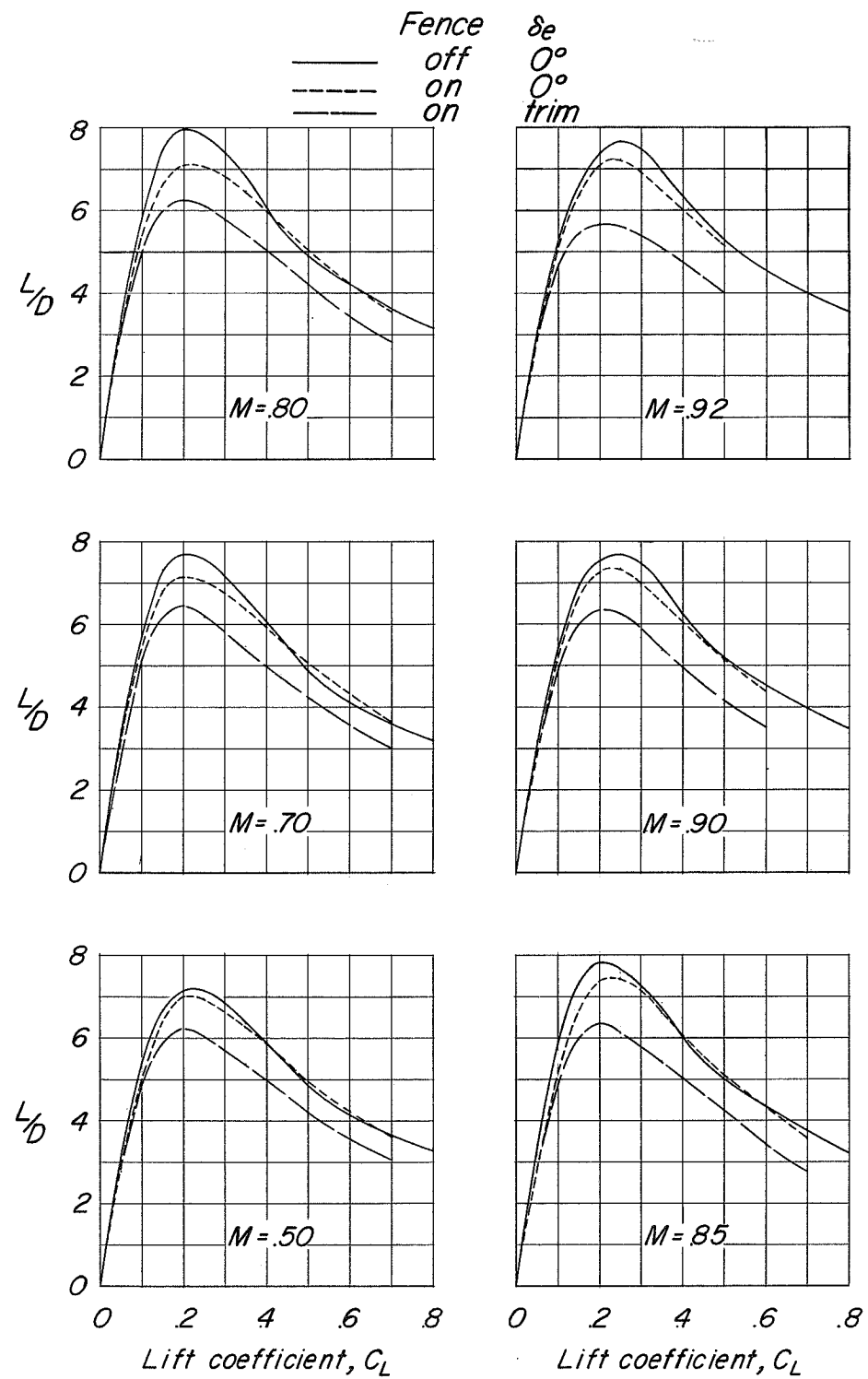


Figure 25.- Lift-drag ratios of configuration BCWV with and without fence 1 and in trim with fence 1, $\delta_r = 0^\circ$, center of gravity at $0.30\bar{c}$.

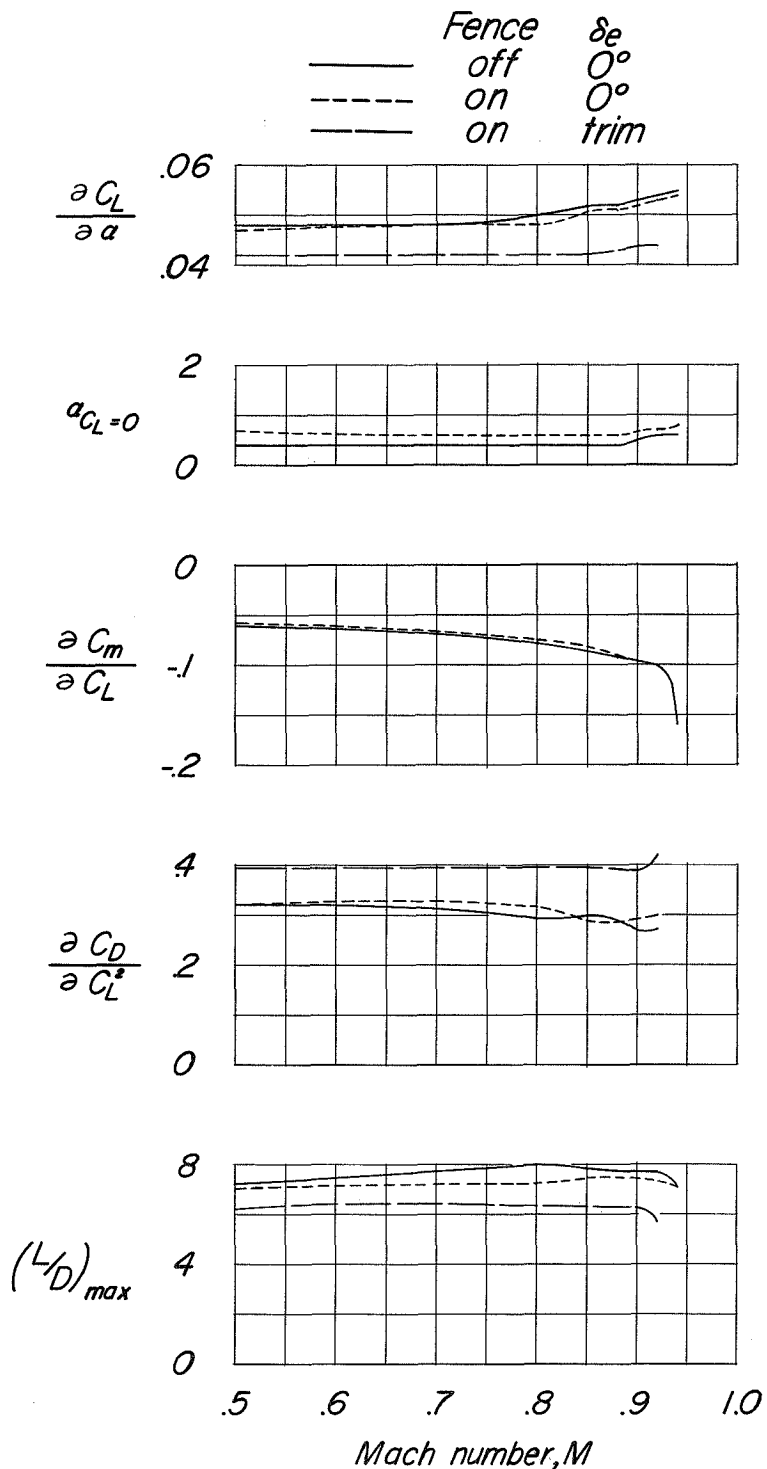


Figure 26.- Summary of aerodynamic characteristics in pitch of configuration BCWV with and without fence 1 and in trim with fence 1, $\delta_r = 0^\circ$, center of gravity at $0.30c$. (Slopes are averaged over lift-coefficient range of 0 to 0.4.)

~~CONFIDENTIAL~~
Restriction/Classification Cancelled

~~CONFIDENTIAL~~
Restriction/Classification Cancelled